DESIGN AND DEVELOPMENT OF A LINEAR TRAVELLING WAVE MOTOR

by

Ricardo J. Zemella
B.S., Massachusetts Institute of Technology
(1988)

SUBMITTED IN PARTIAL FULFILLMENT
OF THE REQUIREMENTS OF THE
DEGREE OF

MASTER OF SCIENCE IN
AERONAUTICS AND ASTRONAUTICS

at the

MASSACHUSETTS INSTITUTE OF TECHNOLOGY
May 1990

Signature of Author_____
Department of Aeronautics and Astronautics
May 11, 1990

Certified by_____
Prof. Andreas von Flotow
Thesis Supervisor

Accepted by_____
Prof. Harold Y. Wachman
Chairman, Departmental Committee on Graduate Students

Acknowledgements

I wish to thank the members of Piezo Systems, Inc., in particular Steve D. Lawrence, for their invaluable assistance in mounting the piezoelectric ceramics for the travelling wave motor. Their technical skills as well as their financial support helped making this project a success.

I also wish to thank Al Shaw, Paul Bauer, Don Weiner, Earl Wassmouth and Fred Cote for their patience and assistance in constructing and assembling the hardware required for this project.

Finally, I wish to thank my advisor Andreas von Flotow for giving me the opportunity to work in a project which was both interesting and fun.

Design and Development of a Linear
Travelling Wave Motor

by

Ricardo J. Zemella

Submitted to the Department of Aeronautics and Astronautics
on May 11, 1990 in partial fulfillment of the requirements
for the Degree of Master of Science in
Aeronautics and Astronautics

Abstract

A linear ultrasonic travelling wave motor was designed and built to operate at a resonant frequency of 27230 Hz. The performance of the motor was evaluated by placing small objects on its upper surface, and measuring the speed and force with which these objects were displaced. The measured overall efficiency of the motor was calculated at 0.1%. It was found that ultrasonic motors are capable of displacing objects that are smaller than the wavelength of the travelling waves. It was also discovered that aerodynamic effects affect the performance of a travelling wave motor by creating a cushion of air that separates the surface of the track from objects placed on top of it.

Thesis Supervisor : Professor Andreas von Flotow
Title : Assistant Professor of Aeronautics and Astronautics

Table of Contents

List of Figures

I-Introduction

The propagation of waves in elastic bodies is an area of structural dynamics that has been extensively researched by Love [1], Graff [2] and many others since as far back as the last century. Recently, some research has focused on the idea of harnessing the energy transported by a travelling wave and using it to move objects in a controlled fashion. Devices capable of doing this are commonly referred to as travelling wave motors, or also as ultrasonic motors because of the frequency range in which they operate.

The basic principles behind the operation of travelling motors (see Chapter II) have been understood for several decades. Consider the propagation of a transverse wave in a beam. As a crest passes, the upper surface of the beam is locally lifted and pushed forward, then lowered and pulled backwards to its initial position, as the wave leaves. A body set at a point of passage of the wave will be lifted and, by friction, will follow the backward motion of the surface of the beam. Motion is therefore created. Unlike conventional motors, a travelling wave motor does not use magnets, coils or brushes to produce movement and do work. Instead, it relies on friction.

The absence of magnets makes travelling wave motors comparatively light. Furthermore, travelling wave motors do not have gears and other moving parts. This suppresses phenomena such as stiction and backlash between gears. The overall simplicity of travelling wave motors suggests the possibility of scaling down these engines to miniscule proportions. This possibility, in fact, is being explored by the Artificial Intelligence Laboratory at MIT. Their goal is to etch a motor onto a silicon wafer thereby providing locomotion to the mini-robots also being developed at that laboratory. [3]

On the other side of the spectrum, the Technische Hochschule at Darmstadt in the Federal German Republic, is attempting to scale up these engines for their possible use in industrial applications. A rotary travelling wave motor, with a rotor measuring more than a meter in diameter has been built in prototype. [personal communication with Dr. Wallachek from the Technische Hochschule]

The largest body of work on travelling wave motors probably comes from The Central Research Laboratory of Matsushita General Industrial Co. in Osaka, Japan. The work of Kawasaki, Ise, Inaba, Takeda, Yoneno and others has led to the development of several prototypes of ultrasonic motors. Most of them, such as the prototype produced by National Panasonic [4], are rotary in type. These motors usually consist of a vibrating metallic disk or ring, referred to as the stator, and a second disk, or rotor, which rests on the stator and rotates once the motor is in operation. These prototypes have performed successfully and have spurred further investigation in the area. Some variations on these prototypes have actually found commercial applications in auto focus cameras [5] and experimental high resolution X-Y Plotters [4].

Fewer attempts have been made to develop a linear ultrasonic motor. In contrast to rotary motors, linear motors must replace circular stators for straight beams which serve as waveguides for the travelling waves, and the rotors become small sliders which rest on only part of the waveguide at any given moment in time. The stumbling block with linear motor designs is the finite dimensions of the waveguide. The physical terminations of a waveguide requires that energy be added at one end of it and removed at the other in order to avoid internal reflections of the travelling waves and possible destructive interference patterns.

A linear travelling wave motor was built by Kuribayashi, Ueha and Mori [6] using a straight beam and a pair of linear transducers. The overall efficiency (mechanical output to

electrical input) obtained was less than 1%. The author does not know of any other attempt at building a linear travelling wave motor.

Linear ultrasonic motors are potentially useful in a wide range of applications. The absence of moving parts renders the motor suitable for space applications such as serving as a transport mechanism between sections of a large space station. Smaller versions of the motor can be used as linear actuators for robots and tele-operators as well as optical alignment systems or even toys. Large scale versions of the motor, if proven economical, could replace forklifts for moving heavy containers in warehouses, and replace conveyor belts as people movers in large airports and malls.

This thesis proposes to design and construct a linear travelling wave motor consisting of two straight waveguides joined by two semicircular waveguides, and to quantify the behavior and performance of the motor. This configuration represents a compromise between traditional rotary travelling wave motors and a purely linear motor as described above. By retaining mechanical closure, the racetrack configuration proposed in this thesis takes advantage of resonant effects and avoids dealing with waveguide termination problems. This configuration however, allows us to explore the behavior of straight lengths of track and of localized sliders resting on only part of the travelling waves.

The remainder of this thesis is structured in the following way. The basic principles behind the operation of a travelling wave motor are presented in Chapter 2. The theoretical considerations behind the implementation of the motor and a description of the construction and assembly processes can be found in Chapter 3. Chapter 4 elaborates on the testing procedures used to assess the motor's performance, presents the results obtained and goes into further analysis of phenomena not predicted at the onset of this project. Chapter 5 states the conclusions derived from the experiments and points out areas of research which require further investigation.

II- Basic Principles

An ultrasonic travelling wave motor is a frictional motor driven by ultrasonic vibrations. It consists of essentially two parts, an elastic body, which serves as a medium for the travelling waves, and a moving body, which rests on the elastic body and gets displaced in the direction opposite to that in which the waves travel (Figure 1) . The force responsible for acting on the moving body originates from the physical interaction between the elastic and the moving bodies. The magnitude of such a force is limited by the friction between the bodies. If there is no friction, the travelling wave motor does not operate, i.e.- the energy in the travelling waves does not get transferred to the moving body.

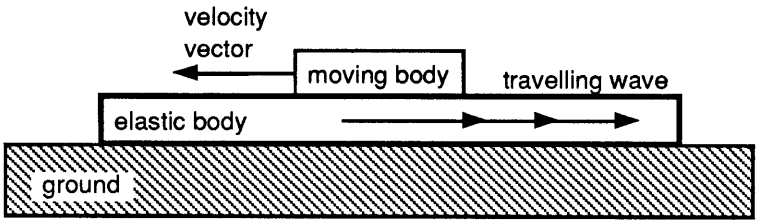

Figure 1- Essential Components of Travelling Wave Motor

The process by which the oscillatory motion of the elastic body is transformed into motion in the moving body is illustrated in Figure 2. A point located along the bending axis of the beam will experience simple harmonic motion along a path that approximately describes a straight line normal to the axis of the beam. A point, however, located on the surface of a beam will experience an added axial component to its motion. If the shear deformation is negligibly small, the axial motion will be proportional to the lateral deflection and inversely proportional to wavelength. This side to side motion, combined with the displacement in the vertical direction, results in an elliptical trajectory for the surface particle. The apogee of the elliptical trajectory for a given point on the beam corresponds to the time when the crest of the lateral deflection travelling wave coincides

with that point. At any given instant, a moving body of length greater than the wavelength of the travelling wave is in contact only with those points of the elastic body which are at their apogees. The velocity imparted to the moving body by these contact points is opposite in direction to the velocity of the travelling wave.

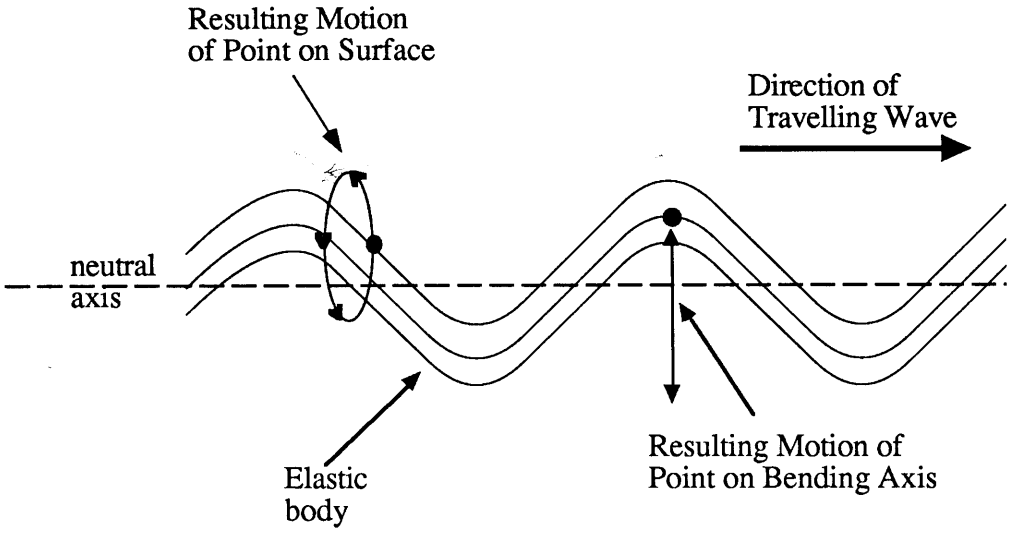

Figure 2- Trajectory of points on the surface and along bending axis of beam

As the motor is turned on, an object placed on top of the surface of the elastic body is subjected to a frictional force which accelerates the body to its final velocity. This final velocity is attained once the speed of the moving body matches the speed of those points on the elastic body which are at the apogee of their elliptical motion. Once these speeds are matched, the elastic body no longer exerts a force on the moving body except that needed to maintain its constant speed. The exact nature of this transient is not well understood. It is safe to assume, however, that the surface properties of the two bodies in contact will affect the performance of this type of motor. More elaborate models of this frictional force and surface interaction are beyond the scope of this thesis.

By assuming that in steady state operation the velocity of the moving body matches that of those points on the elastic body which are at the apogee of their trajectories, a mathematical expression for the velocity of the moving body as a function of the frequency and amplitude of the travelling waves can be derived using geometrical considerations. Figure 3 shows a beam of thickness T undergoing a deflection y_o. The distance ζ corresponds to the side motion of a point P_o which gets displaced to P as a function of θ as the wave travels through the beam.

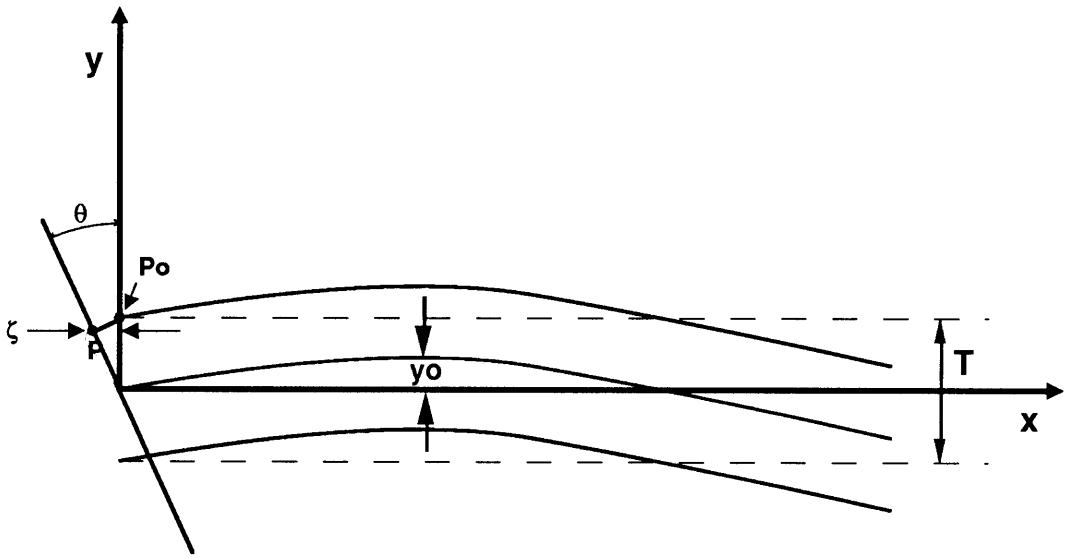

Figure 3- Geometrical description of beam undergoing bending due to Travelling Wave

The equation describing the vertical position, **y** of a point on the surface of the elastic body is given by :

$$y = y_o \sin(kx - \omega_o t) + \frac{T}{2}\cos(\theta) \qquad (1)$$

where: k = wave number of the travelling wave

T = thickness of the beam or elastic body

ω_o = frequency of excitation

Similarly the axial motion, ζ, can be described by :

$$\zeta = \frac{T}{2}\sin\theta \tag{2}$$

Now for $\theta << 1$ (1) can be written as (3) which then differentiated by x gives us (4).

$$y = y_o \sin(kx - \omega_o t) \tag{3}$$

$$\theta = \frac{dy}{dx} = y_o k \cos(kx - \omega_o t) \tag{4}$$

As shown by Cremer, Heckel and Ungar [7], shear deformation is negligible if the wavelength of a travelling wave is at least six times greater than the thickness of the beam. This implies that for such wavelengths, Bernouilli-Euler theory applies and

$$\theta = \frac{dy}{dx}$$

Thus the axial deflection of a surface particle becomes :

$$\zeta = \frac{T}{2} y_o k \cos(kx - \omega_o t) \tag{5}$$

The time derivative of (5) gives us an expression (6) which is equal to the lateral velocity of a point on the top surface of the elastic body. This equation sets an upper limit for the speed of the moving body as given by equation (7).

$$\dot{\zeta} = \text{velocity} = \frac{y_o \omega_o T \pi}{\lambda} \cos(kx - \omega_o t) \tag{6}$$

$$\text{velocity (max)} = \frac{y_o \omega_o T \pi}{\lambda} \tag{7}$$

III- Design and Construction

Design Goals

The primary goal of this project was to build an ultrasonic travelling wave motor capable of displacing an object along a straight line. The secondary goal was to maintain the motor's design as simple and practical as possible. This was essential if entertaining the possibility of finding commercial applications for the motor and for purposes of making a laboratory prototype work. The only constraints placed upon the design were the following:

- The motor had to be small and simple enough as to allow its construction with the machine tools available, and in a time frame of approximately 3 months.

- The motor had to operate in a stable fashion, without the assistance of any feedback control system.

Overall Configuration Selection

While designing the motor, three different overall configurations were evaluated, each one of them capable of producing linear motion. These configurations can be described best as: treadmill-like motors, straight beam motors, and racetrack-like motors.

Treadmill-like Motors : This motor configuration achieves linear motion by making use of existing rotary travelling wave motors and arranging them in a fashion similar to the one depicted in Figure 4. From the figure, however, it is apparent that this

arrangement is a very inefficient way of producing rectilinear motion. Because of its inherent inefficiency, this configuration was not pursued any further

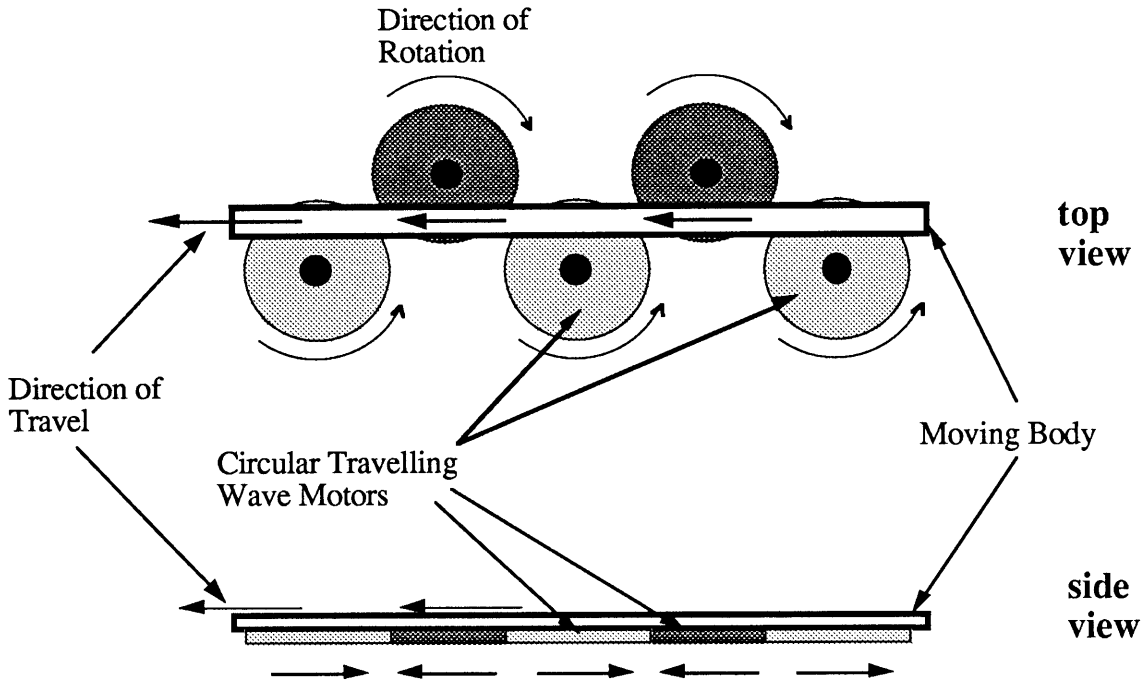

Figure 4- Treadmill Configuration. Linear motion of a body is achieved by making it interact with parts of rotary traveling wave motors.

Racetrack-like Motors: This configuration addresses the main problem of generating travelling waves in a straight beam of finite length : the energy propagated by a travelling wave must be generated at one end and dissipated at the other. This configuration solves this problem, by avoiding it. By wrapping the track around itself the energy in the travelling wave does not have to be dissipated or created, it simply has to be re-directed around the circular portions of the track so that it can be harnessed again in the opposite straight segment of the racetrack.

This configuration avoids the problem of creating or dissipating the energy at the ends of the straight segments, by introducing the problem of creating a discontinuity in the

wave impedance of the track. This discontinuity appears at the transition from a straight to a circular section of the track, and vice versa.

Several alternatives exist to designing a motor with a racetrack configuration. Figure 5 illustrates a motor in which the travelling waves move along the outer surface of what resembles the tread of an army tank. In fact, while in operation, the motor displaces itself in a fashion similar to that of an army tank. The curve section introduces coupling between bending and extensional wave types.

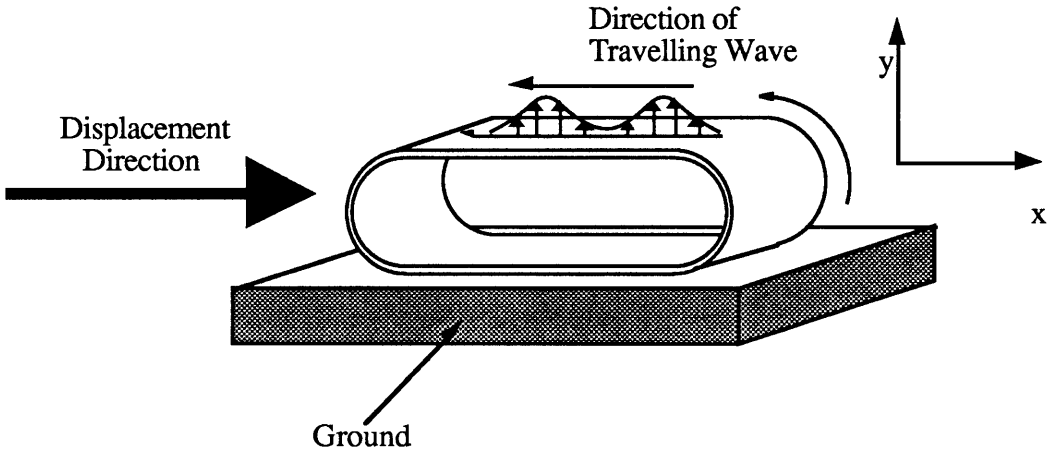

Figure 5- In plane racetrack configuration for travelling wave motor.

Another possible configuration is that of a flat racetrack similar to the one depicted in Figure 6. The travelling waves move along the track and allow objects placed on its surface to be displaced around the length of the track. The curved section introduces coupling between bending and torsional wave types, which might be reduced or removed by design of an asymmetric cross section.

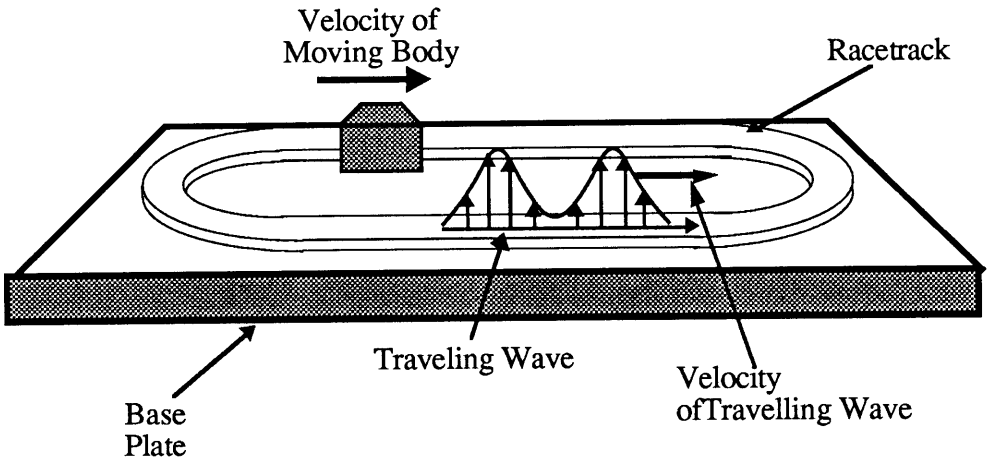

Figure 6- Flat track configuration. Piezo ceramics in the bottom of the track induce transverse travelling waves. Moving body travels in opposite direction of travelling wave.

Straight Beam Motors : This motor configuration fully addresses the problem of creating a travelling wave pattern in a straight beam of finite length: If the energy of a travelling wave is not totally dissipated at the end of a beam, part of it is reflected back thereby interfering with those waves that are still travelling towards the end of the beam. This will complicate the dynamics of such a motor and may affect the performance as a motor.

To solve this problem, one must attach to the ends of the beam systems that will behave as semi-infinite beams, thus artificially changing the dynamics of the finite length beam into that of an infinite medium. Kuribayashi, et al [6], implement this solution by connecting piezoceramic transducers at the ends of the beams using a specific geometric configuration and actuating the transducers so as to cancel reflections at one termination while launching waves at the other end. This is inelegant and very inefficient since most of the power injected into wave propagation is dissipated by wave absorption and does no useful mechanical work.

The configuration selected was that of a flat racetrack, since it does not require any sophisticated control system to implement it, as is the case with the straight beam configuration, nor is its construction too elaborate as is the case of the tank-tread track configuration. The flat racetrack consists of two straight beams interconnected by two semicircular beams. (See Figure 6) The track is made out of a single piece of aluminum and its total length, when measured along its centerline, is equal to an integer number of wavelengths in order to increase motor performance by taking advantage of resonant effects. The bottom side of the racetrack is covered with a thin layer of piezo electric ceramics. The piezo ceramics are driven electrically so as to generate and sustain transverse travelling waves along the length of the track. Small objects, referred to in this paper as "sliders", rest on the top surface of the track and get pushed around it by virtue of the frictional effects described in section II.

Theoretical Considerations

The dynamic characteristics of the motor are entirely defined by the material properties of the racetrack, its cross sectional dimensions, and the radius of curvature of its circular segments. Therefore, the task of designing a motor that meets certain specifications is limited to selecting the appropriate values for these dimensions. This selection, however, requires a deeper understanding of the equations of motion governing the transmission of waves along the racetrack.

The race track is modelled by straight and curved beams connected together. The equations of motion for both straight and curved beams will be analyzed, as well as the behavior of the waves at the junctions of these sections. The results of this analysis will provide some insight about the size requirements for the track, its operational frequency and the track's effectiveness in transmitting transverse waves around its length.

Equations of Motion

Straight beams: The straight portions of the motor were modelled as a one dimensional Bernouilli-Euler beam. Analysis of the equations of motion lead to dispersion relations which provide a functional relationship between the track's cross sectional properties and the frequency and wavelength of the travelling waves that can be transmitted by the track.

Figure 7 depicts a straight beam aligned along the x axis. Transverse deflections along the z axis are denoted by w, while β, denotes the twist angle of a cross section of the beam about its twisting axis. Both w and β are functions of x.

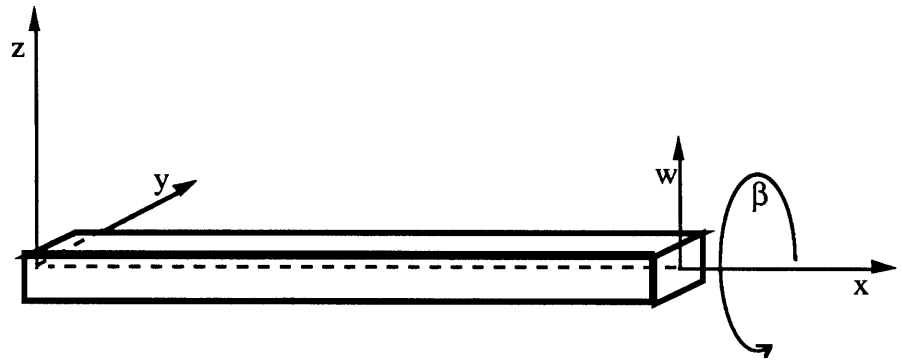

Figure 7- Axis and Variable designation for straight beam equations.

The governing differential equations for this beam are the following:

$$EIw'''' + \rho A\ddot{w} = 0 \quad (8)$$

$$GJ\beta'' - \rho J\ddot{\beta} = 0 \quad (9)$$

where: E = Modulus of elasticity of the beam

I = Bending moment of inertia about the y axis.

G = Torsional stiffness of the beam

ρ = Density of the beam

' = shorthand notation for d()/dx i.e.- spatial derivative

$\dot{}$ = shorthand notation for d()/dt i.e.- derivative with respect to time.

These constants usually appear in certain groupings which have a physical interpretation. The **EI** group defines the bending stiffness of the beam while the **GJ** group represents its torsional stiffness. The mass per unit length of the beam is represented by ρA while ρJ represents the torsional inertia of the beam.

Equation (8) describes the transverse motion of the straight portions of the track while equation (9) describes their torsional behavior. Its apparent from these equations that the transverse and torsional modes of vibration are decoupled along the straight segments of the motor.

Now by assuming a solution for the bending equation of the form:

$$w_{(x,t)} = w_o e^{\gamma x + i\omega t} \quad \text{where} \quad \gamma = \alpha + iK$$

the following dispersion relations are obtained :

$$\gamma = \pm \sqrt[4]{\frac{\rho A \omega^2}{EI}} \quad \text{and} \quad \gamma = \pm i\sqrt[4]{\frac{\rho A \omega^2}{EI}}$$

These dispersion relations show the existence of four wave patterns occurring simultaneously in the structure. These waves come in pairs which travel in opposing directions along the beam. One pair, determined by the real value of γ, is usually referred to as the evanescent pair since the waves decay exponentially in space. Their influence is only felt close to the point were the originating spatial disturbance occurs. The pair determined by the imaginary value of γ, is the travelling set of waves. Given that k is the wave number of the travelling pair of waves, and that :

$$k = \frac{2\pi}{\lambda} \quad \text{and}$$

$$\omega = 2\pi f$$

where: λ = wavelength of the travelling waves

f = frequency of travelling waves in Hz

the following relations can be arrived at:

$$\lambda = \sqrt{\frac{2\pi}{f}\sqrt{\frac{EI}{\rho A}}} \tag{10}$$

$$f = \frac{2\pi}{\lambda^2}\sqrt{\frac{EI}{\rho A}} \tag{11}$$

Given the material properties of the beam (ie.- E, ρ) as well as its dimensions (ie.- I, A), **f** becomes a simple function of λ. Equations (10,11) remain valid as long as the basic Bernouilli-Euler beam assumption applies, that is, the wavelength of the waves carried by the beam has to be much greater than the beam's thickness. If the wavelength becomes too short, shearing in the beam becomes a major factor and the Bernouilli Euler model ceases to be valid. As shown by Cremer, Heckel and Ungar [7], the wavelength of the travelling waves should be at least six times greater than the thickness of the track for the hypothesis to hold. This lower limit on the wavelength, translates into an upper limit for the frequency at which the beam can be driven.

Equation (11) shows that the operating frequency of the motor can be increased by using a stiffer material, while maintaining the wavelength and cross sectional dimensions constant. By substituting into equation (11) the expressions for the bending moment of inertia, **I**, and the cross sectional surface area, **A**, it becomes apparent that :

$$f = \frac{2\pi}{\lambda^2}\sqrt{\frac{Eh^2}{12\rho}} \tag{12}$$

where: h = thickness of the beam (ie. track)

Equation (12) shows that the operating frequency of the motor is proportional only to the thickness of the track and that it is independent of its width.

Curved Beams : The curved sections of the track were modelled as curved beams with a rectangular cross section. Their dynamic behavior is described by a coupled pair of differential equations which relate the transverse displacement of the beam to its rotation about its twisting axis. As the radius of curvature of the beam approaches infinity, the equations of motion describing its behavior decouple and simplify to the rectilinear model of equations (8) and (9).

Figure 8 depicts a beam with a constant radius **R**, a transverse displacement **v**, and a twisting angle of β. The system of coordinates **u**,**v**,**w** is aligned such that **u** points at the center of curvature of the beam while **w** remains tangent to the path length **s**. **v** remains perpendicular to the path length **s**. Love [1] derived the equations of motion for a circular rod of arbitrary curvature. These equations can be adapted specifically to the circular portions of the racetrack. This derivation is given in Appendix 2.

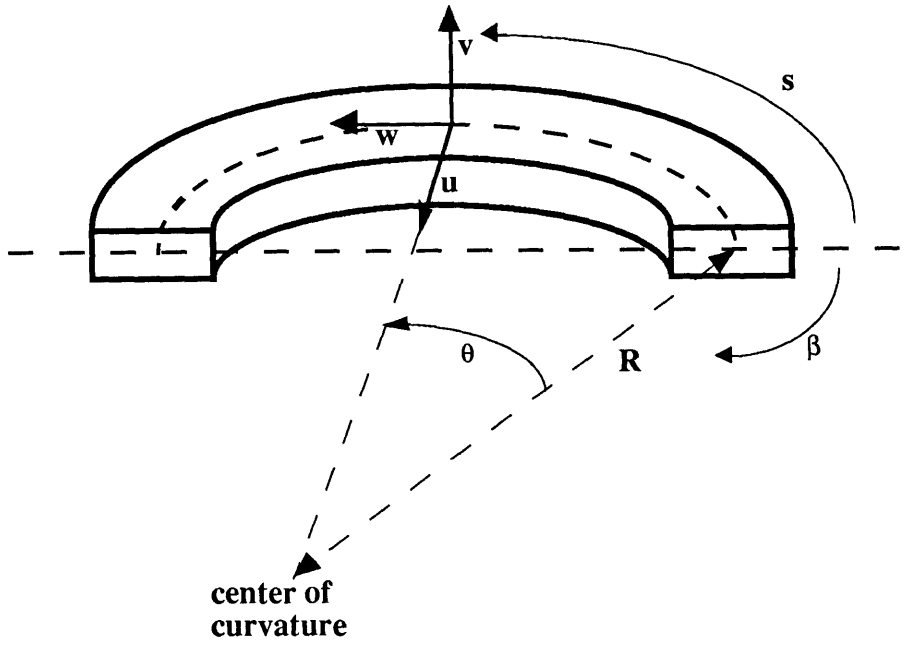

Figure 8- Axis and Variable designation for the derivation of the Equations of Motion for a Curved Beam.

The equations of motion for the curved beam are the following:

$$EIv'''' + \rho A\ddot{v} = \frac{1}{R}(EI + GJ)\beta'' + \frac{1}{R^2}GJv'' \tag{13}$$

$$GJ\beta'' - \rho J\ddot{\beta} = -\frac{1}{R}(EI + GJ)v'' + \frac{EI\beta}{R^2} \tag{14}$$

where: v = transverse displacement of a particle

β = the angle of twist about the twisting axis

' = shorthand notation for spatial derivative d()/ds

R = radius of the beam

These equations state that, if the radius of curvature of a beam is finite, the out of plane motion of a transverse wave will produce torsional waves. As the radius of curvature becomes smaller, the magnitude of the coupling terms becomes larger. This implies that a smaller radius of curvature hinders the performance of the racetrack because a greater amount of energy is taken away from the transverse travelling waves in order to generate the torsional waves.

Quantifying this effect is important for design purposes. A tradeoff between the radius of the circular sections of the track and the amount of coupling between transverse and torsional modes has to be evaluated. The dispersion curves for waves travelling in a circular section of the beam offer valuable insight to this behavior. These can be obtained by translating equations (13) and (14) into state-space form and forming a transition matrix. The eigenvalues of this matrix reveal which wavetrains are evanescent (ie- real eigenvalues) and which ones are travelling waveforms (ie.- purely imaginary eigenvalues). The dispersion curves, in this particular instance, were found to be most useful in their non-dimensional form. Hence, we proceed to non-dimensionalize equations (13) and (14), translate them into state-space form, and obtain the eigenvalues of the transition matrix.

The variable changes and groupings used were the following:

$$\Sigma = GJ + EI \qquad \text{and} \qquad \Phi = EIGJ$$

where Σ and Φ are defined purely for convenience to simplify the written expressions. Then there is:

$$\omega_{nd} = \frac{\omega h}{c} \qquad \text{where:} \qquad c^2 = \frac{E}{\rho}$$

where ω_{nd} corresponds to a non-dimensional frequency expression. In this case, ω has been non-dimensionalized by c, the velocity of longitudinal waves in the beam, and by h,

the thickness of the beam. The bending moment of inertia and hence the wavespeed is most sensitive to changes in h.

The last grouping used:

$$\Xi \equiv \frac{h}{R}$$

was defined as the ratio between the thickness of the beam, **h**, and the radius, **R**. The theoretical performance of a given track design can now be evaluated as a function of the non-dimensional curvature Ξ. In the limit, a small value of Ξ corresponds to a track that behaves like a straight beam, with little or no coupling between the transverse and torsional modes. A big value of Ξ will result in a large amount of coupling between the torsional and transverse modes of vibration.

Non-dimensionalization of equations (13) and (14) lead to equations (15) and (16) respectively:

$$\left(h^3 v''''\right) = \frac{\Xi h}{\Phi}\left\{(GJ)^2 - \Sigma^2\right\}(hv'') + \frac{\rho A \omega_{nd}{}^2 h^2 c^2}{EI}\left(\frac{v}{h}\right) + \frac{\Xi^3 \Sigma}{\Phi}\left(EI - \frac{\rho J \omega_{nd}{}^2 c^2}{\Xi^2}\right)(\beta) \tag{15}$$

$$\left(h^2 \beta''\right) = \left(\frac{EI\Xi^2}{GJ} - \frac{\rho J \omega_{nd}{}^2 c^2}{GJ}\right)(\beta) + \frac{\Xi\Sigma}{GJ}(hv'') \tag{16}$$

These equations correspond to the non-dimensional equations of motion for the curved sections of the motor. Rewriting them in state-space form, we obtain a matrix equation of the form :

$$h\frac{d}{ds}\bar{X} = A\bar{X}$$

where $\bar{X}$ is the state vector and A is the transition matrix. These matrices are the following:

$$\bar{X} = \begin{bmatrix} \frac{v}{h} \\ v' \\ hv'' \\ h^2 v''' \\ \beta \\ h\beta' \end{bmatrix}$$

$$A = \begin{bmatrix} 0 & 1 & 0 & 0 & 0 & 0 \\ 0 & 0 & 1 & 0 & 0 & 0 \\ 0 & 0 & 0 & 1 & 0 & 0 \\ \frac{\rho A \omega_{nd}^2 t^2 c^2}{EI} & 0 & \frac{h\Xi}{\phi}\left((GJ)^2 - \Sigma^2\right) & 0 & \frac{\Xi^3 \Sigma}{\phi}\left(EI - \frac{\rho J \omega_{nd}^2 c^2}{\Xi^2}\right) & 0 \\ 0 & 0 & 0 & 0 & 0 & 1 \\ 0 & 0 & \frac{\Xi\Sigma}{GJ} & 0 & \frac{EI\Xi^2}{GJ} - \frac{\rho J \omega_{nd}^2 c^2}{GJ} & 0 \end{bmatrix}$$

Given this A matrix, it is now possible to determine its eigenvalues and plot their imaginary component (ie- the wavenumber of the travelling waves) as a function of the non-dimensional frequency. Figure 9 illustrates both the torsional (normal line) and the transverse (dashed lines) travelling wave modes for different values of Ξ (ie.- h/R).

As the radius of curvature of the track increases relative to its thickness, the cutoff frequency of the transverse mode decreases. This cutoff frequency corresponds to the frequency value below which, the circular beam cannot serve as a waveguide for transverse waves. Furthermore, this cutoff frequency corresponds to a wavelength which is equal to the radius of curvature of the track.

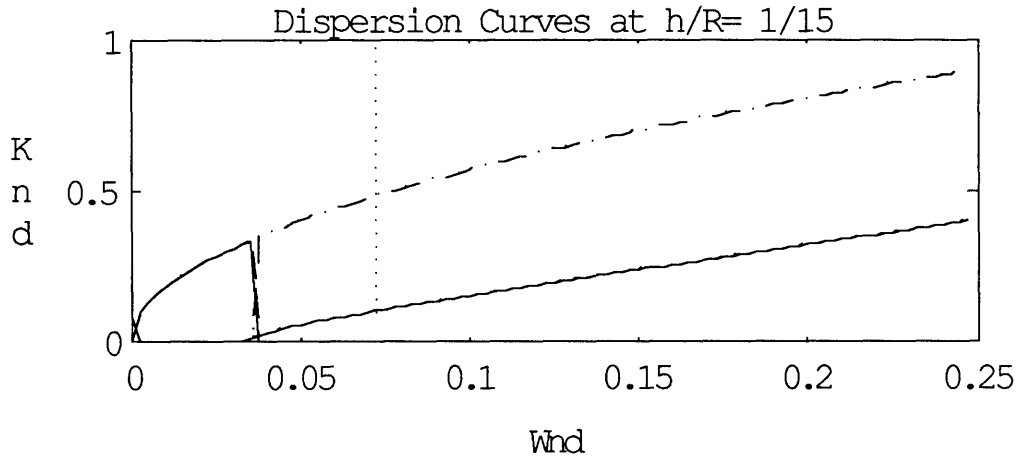

h/R).

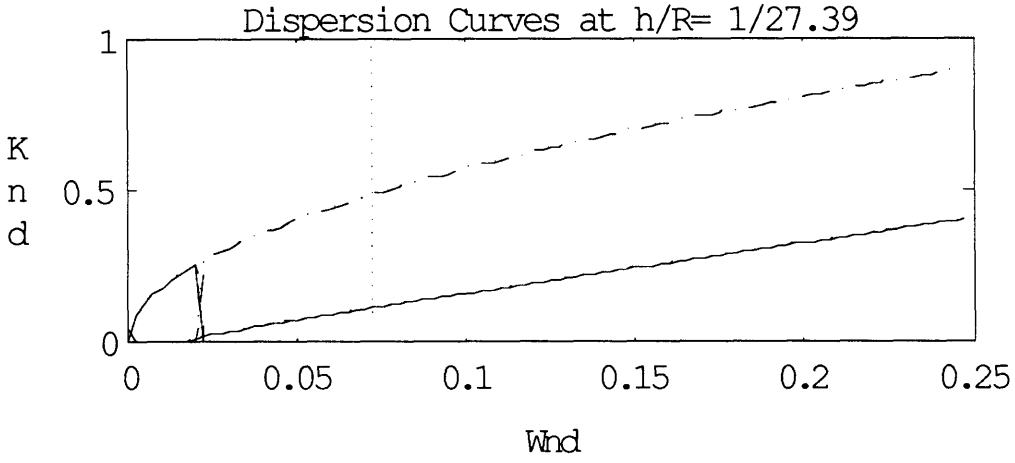

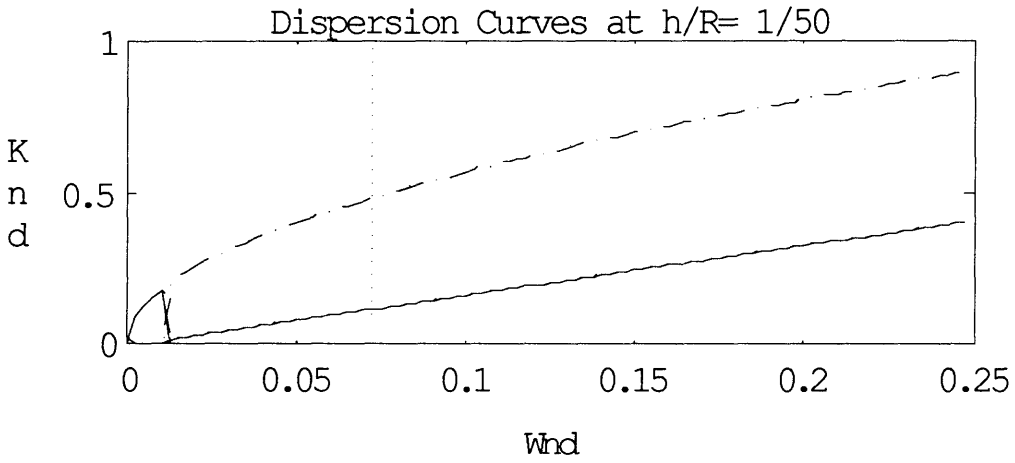

Figure 9- Non-Dimensional Dispersion Curves for Circular Beams.

From a design point of view, the operating frequency of the motor is bounded on the lower side by the consideration that the wavelength of the travelling waves in the track has to be smaller than the radius of curvature of the curved sections of the track. On the other hand, the upper limit for the operating frequency of the motor is dictated by shearing effects of the beam. Since the thickness of the track remains the same in both the curved sections of the track as well as the straight ones, the upper limit of the operating frequency of the motor was chosen to be the same as that for the straight sections: the frequency has to be lower than the value that corresponds to a wavelength six times greater than the thickness of the track.

Scattering Analysis

Dispersion curves provide an estimate on how a disturbance will travel through a given section of the racetrack. The race track, however consists of four distinct sections: two straight ones and two curved ones. The junction between a straight section and a curved one can create problems because of impedance mismatch. This may cause unwanted reflections.

If the impedance between two adjacent sections is perfectly matched, a wave travelling along the first section will move onto the second section without noticing any changes on the medium its traveling on. Two perfectly bonded straight beams of similar cross sectional dimensions, would be an example of perfect impedance matching.

The dispersion relations for a straight beam and a curved beam are different, hence, there is probably an impedance mismatch at their junction. As the radius of curvature of the curved section gets smaller, this mismatch increases. Scattering analysis of the junction provides a way to quantify the effect of this impedance mismatch.

Figure 10 shows the notation convention used to designate wavetrains going into and out of a junction. Notice that each section of the track has six different wavetrains corresponding to it. Four of these wavetrains correspond to the transverse vibrational modes and represent solutions to the fourth order beam equations of motion (equations 8 and 13). The other two, correspond to torsional modes of vibration and represent solutions to the second order torsional equations of motion (equations 9 and 14).

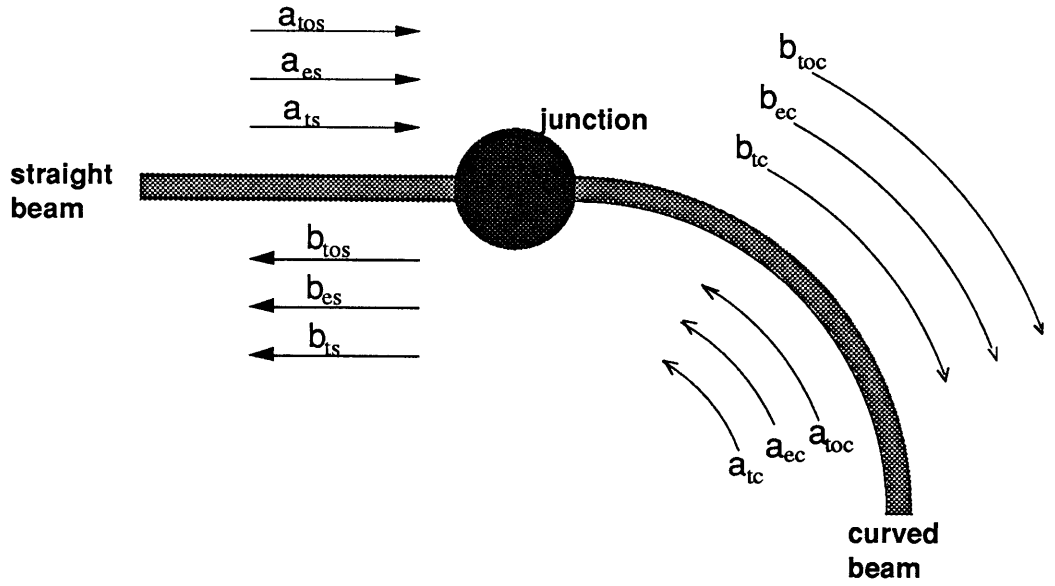

Name Code for Wave Trains
(1 letter from each group)

a = into node	**to** = torsional wave	**s** = straight section
b = out of node	**e** = evanescent wave	**c** = curved section
	t = travelling wave	

Figure 10- Convention Used for Designating the Various Wavetrains Common to a Junction

As a wavetrain enters a junction, part of it gets reflected, while part of it gets transmitted through the junction. All wavetrains entering a junction are designated by a letter **a**, while those wavetrains leaving a junction are designated by a **b**. A perfect

transmission at a junction implies that a given wave mode entering a junction will leave it with the same amount of energy it entered. If the transmission is not ideal, the energy of an incoming wavemode will be distributed between the reflected wave modes and the transmitted ones. If there is coupling between the various modes, a scattering effect will occur at the junction by which a given wavemode will excite other wavemodes other than its own. As a result, of this scattering, it is possible for example, that an incoming transverse wave may result in both an outgoing transverse and torsional waves.

The following scattering analysis will result in a scattering matrix which relates the outgoing wave modes at a junction as a function of the incoming wavemodes. This analysis will use the the boundary conditions at the junction in their dimensional form.

At the junction between the straight beam and the curved beam, there are six boundary conditions which must be satisfied. They are the following:

$$v_c = v_s \quad \text{----------} > \quad \text{equal displacements}$$

$$v_c' = v_s' \quad \text{----------} > \quad \text{equal slopes}$$

$$\beta_s = \beta_c \quad \text{----------} > \quad \text{equal twist angles}$$

$$EIv_s''' = EIv_c''' \quad \text{----------} > \quad \text{Shear balance}$$

$$EIv_s'' = EIv_c'' - \frac{EI\beta_c}{R} \quad \text{----------} > \quad \text{Moment Balance}$$

$$GJ\beta_s' = GJ\beta_c' + \frac{GJv_c'}{R} \quad \text{----------} > \quad \text{Torsional Balance}$$

where the subscript "c" refers to a variable related to the curved beam, while a subscript "s" refers to a variable related to the straight beam. (Note: w as defined in Figure 8, is equal to

v_S, and β as defined in Figure 9 is equal to β_S). By defining state vectors $\mathbf{Y_c}$ and $\mathbf{Y_S}$ as follows :

$$Y_s = \begin{pmatrix} v_s \\ v_s' \\ EIv_s'' \\ EIv_s''' \\ \beta_s \\ GJ\beta_s' \end{pmatrix} \qquad Y_c = \begin{pmatrix} v_c \\ v_c' \\ EIv_c'' \\ EIv_c''' \\ \beta_c \\ GJ\beta_c' \end{pmatrix}$$

the boundary conditions can be re-written in matrix form as follows :

$$\begin{pmatrix} 1 & 0 & 0 & 0 & 0 & 0 & -1 & 0 & 0 & 0 & 0 & 0 \\ 0 & 1 & 0 & 0 & 0 & 0 & 0 & -1 & 0 & 0 & 0 & 0 \\ 0 & 0 & 1 & 0 & 0 & 0 & 0 & 0 & -1 & 0 & \frac{EI}{R} & 0 \\ 0 & 0 & 0 & 1 & 0 & 0 & 0 & 0 & 0 & -1 & 0 & 0 \\ 0 & 0 & 0 & 0 & 1 & 0 & 0 & 0 & 0 & 0 & -1 & 0 \\ 0 & 0 & 0 & 0 & 0 & 1 & 0 & \frac{-GJ}{R} & 0 & 0 & 0 & -1 \end{pmatrix} \begin{pmatrix} Y_s \\ Y_c \end{pmatrix} = 0$$

which can be also expressed as :

$$[B_s \vdots B_c] \begin{bmatrix} Y_s \\ Y_c \end{bmatrix} = 0$$

where B_S corresponds to the first 6 x 6 block and B_c corresponds to the second 6 x 6 block matrix.

Now, using Y_c and Y_s as state vectors, Fourier Transformed equations (8),(9) and (13),(14) can be re-written in state space form. These corresponding matrices are the following :

$$A_s(\omega) = \begin{bmatrix} 0 & 1 & 0 & 0 & 0 & 0 \\ 0 & 0 & \frac{1}{EI} & 0 & 0 & 0 \\ 0 & 0 & 0 & 1 & 0 & 0 \\ \rho A\omega^2 & 0 & 0 & 0 & 0 & 0 \\ 0 & 0 & 0 & 0 & 0 & \frac{1}{GJ} \\ 0 & 0 & 0 & 0 & -\rho J\omega^2 & 0 \end{bmatrix}$$

and

$$A_c(\omega) = \begin{bmatrix} 0 & 1 & 0 & 0 & 0 & 0 \\ 0 & 0 & \frac{1}{EI} & 0 & 0 & 0 \\ 0 & 0 & 0 & 1 & 0 & 0 \\ \rho A\omega^2 & 0 & \frac{1}{EIR^2}\left(GJ - \frac{(EI+GJ)^2}{GJ}\right) & 0 & \frac{(EI+GJ)}{GJR}\left(\frac{EI}{R^2} - \rho J\omega^2\right) & 0 \\ 0 & 0 & 0 & 0 & 0 & \frac{1}{GJ} \\ 0 & 0 & \frac{-(EI+GJ)}{EIR^2} & 0 & \frac{EI}{R^2} - \rho J\omega^2 & 0 \end{bmatrix}$$

where $A_s(\omega)$ corresponds to the straight beam and $A_c(\omega)$ corresponds to the circular beam. Let $\mathbf{e_s}$ be the matrix of eigenvectors of $A_{s(\omega)}$ and $\mathbf{e_c}$ be the matrix of eigenvectors of $A_{c(\omega)}$. Then introduce the similarity transformations :

$$Y_s = e_s w_s \quad \text{and} \quad Y_c = e_c w_c$$

where w_s and w_c are columns of wave mode coordinates [8,9] travelling independently along the straight and curved segments respectively. The Boundary conditions can then be written as :

$$[B_s e_s \vdots B_c e_c] \begin{pmatrix} w_s \\ w_c \end{pmatrix} = 0$$

which can be rearranged into outgoing and incoming wave modes such that:

$$[B_a \vdots B_b]\begin{pmatrix} a \\ b \end{pmatrix} = 0 \qquad \text{or}$$

$$B_a\vec{a} + B_b\vec{b} = 0 \tag{17}$$

where $\vec{a}$ and $\vec{b}$ are the incoming and outgoing wavetrain vectors defined according to the conventions in Figure 10, as follows:

$$\vec{b} = \begin{pmatrix} b_{ec} \\ b_{ts} \\ b_{toc} \\ b_{es} \\ b_{ts} \\ b_{tos} \end{pmatrix} \qquad \vec{a} = \begin{pmatrix} a_{es} \\ a_{ts} \\ a_{tos} \\ a_{ec} \\ a_{tc} \\ a_{toc} \end{pmatrix}$$

By performing a partial inversion of equation (17), the outgoing wavetrains can be expressed in terms of the incoming ones (18). The matrix that relates them is the scattering matrix of the junction between the straight beams and the circular beams.

$$\vec{b} = -B_b^{-1}B_a\vec{a} \tag{18}$$

$$\text{Scatter} = -B_b^{-1}B_a$$

$$\vec{b} = (\text{Scatter})\vec{a}$$

Given the way in which the vectors $\vec{a}$ and $\vec{b}$ are defined, the scattering matrix provides information on how much of a given wave mode is reflected, and how much is

transmitted at a junction. The scattering matrix is a 6x6 matrix which can be understood as follows:

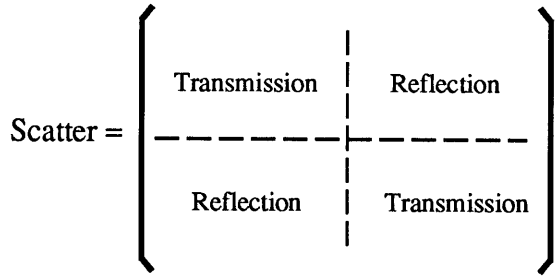

The elements along the main diagonal represent the extent to which a given wave mode transmits through the junction. Perfect transmission would imply that the scattering matrix is equal to identity. The presence of reflection at the junction and cross coupling between wave modes, produces non-zero entries in the off diagonal terms. Since the equations used for this analysis are in dimensional form, those elements along the main diagonal of the scattering matrix represent a fraction of unity in which 1 is equal to perfect transmission of that wave mode through the junction. Similarly, the elements along the diagonals of the reflection block matrices represent a fraction of unity in which 1 corresponds to total reflection of a given wavemode.

Because of their mixed units, the other elements of the scattering matrix don't provide much insight about the extent to which wavemodes are coupled, unless the columns of the matrix are non-dimensionalized so that they represent the energy delivered by each wavemode. This extra work becomes unnecessary however, if the values along the main diagonal indicate that there is good transmission at the junction.

As the radius of curvature of the curved sections of the track increases, the scattering matrix approaches the identity matrix. Conversely, as the radius of curvature of the track decreases, coupling terms appear in the off diagonal positions of the scattering

matrix while the elements along the main diagonal decrease in magnitude from their ideal value of one.

From a design point of view, transmission at the junction would be optimized if the radius of curvature of the circular portions of the motor was equal to infinity (ie.- there would be no discontinuity). In practical terms the radius of curvature of the track should be selected such that the diagonal terms of the scattering matrix approach unity within an error that may be deemed acceptable.

Cross Sectional Banking of the Track

The primary concern of both the dispersion and scattering analysis was to evaluate, the extent to which coupling between torsional and transverse modes occurred as a result of the geometrical configuration of the race track. This section, however, investigates the possibility of eliminating the coupling between bending and torsion in a curved beam by varying the cross sectional properties of the curved beam.

A simple approach to the problem consists in taking a plate viewpoint; modelling the curved segment of the track as a series of infinitesimally thin beams only capable of deflecting transversely. Furthermore, it is convenient to assume that the beams are not coupled to one another. Given this model, the problem of decoupling torsional and transverse modes in the racetrack boils down to turning the wavefront so that it follows the track. The wavefront is turned by forcing the waves travelling in the outside of the track to go faster than the waves travelling in the inside of the track.

The speed of a travelling wave is given by equation (19):

$$c = \lambda f \tag{19}$$

where : $c =$ speed of the travelling wave along the track

After substituting in the following expressions:

$$\lambda = \frac{2\pi}{k} \qquad k = \sqrt[4]{\frac{\rho A}{EI}}\,\omega^{\frac{1}{2}} \qquad \text{and} \qquad I = \frac{bh^3}{12}$$

we arrive at equation (20) which shows that the velocity of a travelling wave is proportional to the thickness of the track to the power of one half .

$$c = 2\pi\omega^{\frac{1}{2}}\sqrt[4]{\frac{Eh^2}{12\rho}} \tag{20}$$

Figure 11 illustrates a section of a curved beam. The centerline of the track is located at a distance **r**, and the wavespeed at that radial location is **c.** During a given length of time t, the wavefront displaces itself by a distance **ds** along the centerline. Waves travelling on the outside of the track, need to travel the same angular distance in the same amount of time, which means that $\mathbf{c_o}$ has to be greater than **c**. Conversely, $\mathbf{c_i}$, at the inside of the track, has to be smaller than **c**.

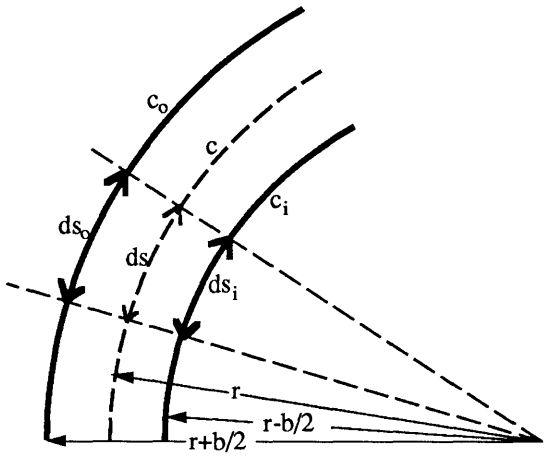

Figure 11- Curved Section of Track. Subscript "i" refers to inner radius and the subscript "o" refers to the outer radius.

The change in speed of the waves throughout the width of the track can be accomplished by varying the thickness of the track across a given cross section. Given that the length of time **t** can be expressed as :

$$t = \frac{ds_i}{c_i} = \frac{ds_o}{c_o} = \frac{ds}{c} \tag{21}$$

Clearly the thickness should vary quadratically with the radial distance from the center of curvature. This is difficult to machine, and we rather consider a thickness distribution linear with radial distance.:

$$h_i = \left(\frac{4r^2 - 4rb + b^2}{4r^2}\right) h_{ref} \tag{22}$$

$$h_o = \left(\frac{4r^2 + 4rb + b^2}{4r^2}\right) h_{ref} \tag{23}$$

where: h_i = thickness of the beam at a distance r-b from the center of curvature

h_o = thickness of the beam at a distance r+b from the center of curvature

r = radius measured along the centerline of the track.

h_{ref} = thickness of reference beam with plain rectangular cross section

Now, by substituting equations (22) and (23) into equation (24), which assumes that the thickness of the track varies in a linear fashion:

$$h_{avg} = \frac{h_i + h_o}{2} \tag{24}$$

we arrive at equation (25):

$$h_{avg} = \left(1 + \frac{b^2}{4r^2}\right) h_{ref} \tag{25}$$

where : h_{avg} = average thickness of the track with variable cross section

This relationship implies that if the thickness of the track is varied linearly, the wavefront will follow the shape of the track as long as the ratio of the width to the radius of curvature of the track is small. If this ratio is not small, the linear approximation cannot be used and the thickness of the track would have to vary quadratically. From a construction point of view, varying of the cross sectional thickness of the track in a linear fashion would be easier than varying it quadratically. For example, a curved beam with a rectangular cross section, with a radius of 2.5 inches, a width of half an inch and a thickness of 80 milli-inches along its centerline would have to be altered so that the thickness along the inside of the track was 51 milli-inches thick and the thickness along the outer radius became 97 milli-inches.

An alternative to varying the cross sectional thickness of the track is to vary its mass distribution. Rewriting equation (20) as a function of μ, the mass per unit length of the beam, we obtain :

$$c = 2\pi\omega^{\frac{1}{2}}\sqrt[4]{\frac{EI}{\mu}} \tag{26}$$

which implies that the velocity of the traveling wave is inversely proportional to the fourth root of μ. After performing an analysis similar to to the one performed for the cross sectional variation of thickness, we obtain the required values of μ, for the outer and inner sections of the track in terms of the μ along the centerline of the track.

$$\mu_o = \mu\left(\frac{r}{r+\frac{b}{2}}\right)^4 \tag{27}$$

$$\mu_i = \mu\left(\frac{r}{r-\frac{b}{2}}\right)^4 \tag{28}$$

where : μo = mass per unit length along the outside of the track.

μi = mass per unit length along the inside of the track.

μ = mass per unit length along the centerline of the track

Varying the density across the width of the track is in practice not feasible. Shifting the center of mass of the beam by placing a lumped portion of mass of higher density on the inside of the track, such that the resulting center of mass is similar to that achieved by a functional variation of density, is feasible. Figure 12 indicates the position of the center of mass of a rectangular beam with a constant density and the center of mass of a rectangular beam whose density varies linearly between the values defined by equations (27) and (28). Using a beam with similar dimensions as that of the previous example, we obtain through equations (27) and (28), that the inside of the track has to have a density 1.5 times greater than the density of the beam with a rectangular cross section. Similarly the outside of the track has to have its density value decreased by a factor of 1.46 relative to the density of the beam with a rectangular cross section.

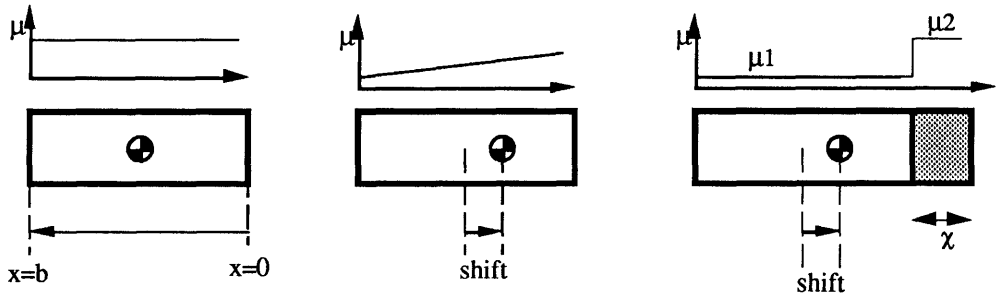

Figure 12- Side Shift of the Position of the Center of Mass across the Width of the Beam due to Variational Distribution of μ and due to Addition of Lumped Mass to One Side. (The center of Curvature is located to the Right hand Side of the Cross sections.)

The center of mass of a rectangular beam is located along the middle of the beam. If we assume that the the mass per unit length varies across the width of the track as shown in Figure 12, then μ can be written as a linear function :

$$\mu = cx + d \tag{29}$$

where, for the example given, c = .1596 and d= -.1734.

The shift of the position of the center of mass in a beam with a density distribution described in equation (29) is equal to:

$$\text{shift} = \left(\frac{\frac{cb^2}{3} + \frac{db}{2}}{\frac{cb}{2} + d} \right) - \frac{b}{2} \tag{30}$$

where: b = width of the track.

For the example at hand, a beam with a linearly varying μ, would have a center of mass located 25 milli-inches away from the center of mass of a beam whose μ remained constant. The direction of this shift is towards the center of curvature of the track.

A similar shift of the center of mass can be attained by adding a lumped mass, of greater density than the rest of the track, to the inner radius of the curved beam. See Figure 12. The relative shift of the center of mass for this configuration is given by equation (31):

$$\text{shift} = \left(\frac{\frac{\chi^2 \mu_2}{2} + \frac{\chi \mu_2 b}{2}}{b\mu_1 + \chi\mu_2} \right) \tag{31}$$

where : χ = width of the cross section of the lumped mass

$\mu 1$ = mass per unit length of track

$\mu 2$ = mass per unit length of lumped mass s.t. $\mu 2 > \mu 1$

By using this approach, the 25 milli-inch shift of the center of mass from the previous example can be duplicated by adding a 13 milli-inch thick strip of lead to the inside of the aluminum track.

Another approach of analyzing the torsion bending coupling along the curved sections of the track with offset between the elastic axis and section center of mass, is to add another term to the governing equations of motion, (13) and (14). It may be possible that they decouple at the desired operating frequency of the motor. As shown by Bisplinghoff [10], this additional term takes into account the separation between the center of mass of the beam and its elastic axis. By incorporating this term to equations (13) and (14), we obtain the following :

$$EIv'''' + \rho A\ddot{v} = \frac{1}{R}(EI + GJ)\beta'' + S_y\ddot{\beta} + \frac{1}{R^2}GJv'' \tag{32}$$

$$GJ\beta'' - \rho J\ddot{\beta} = -\frac{1}{R}(EI + GJ)v'' - S_y\ddot{v} + \frac{EI\beta}{R^2} \tag{33}$$

where $S_y = \rho Ae$ and **e** is defined as the separation between the center of mass and the elastic axis.

In order to decouple equations (32) and (33), the terms in β of equation (32) as well as the terms in **v** of equation (33) have to vanish. This can be accomplished by setting:

$$e = -\frac{(EI + GJ)}{\rho ARf^2\lambda^2} \tag{34}$$

By selecting an operating frequency of 27230 Hz and using the cross sectional properties corresponding to the beam of the previous example, we obtain a value of **e** equal to 31.7 mill-inches. This value is approximately 20 % larger than the value of the center of

mass shifts obtained using the simplified beam models. This suggests that these simplified beam models are relatively good and that the torsional extensional coupling along the curved sections of the beam can be greatly reduced by simply placing a strip of lead along the inside of these sections.

Piezo Ceramic Layout

In order to induce travelling waves along the racetrack, piezo electric ceramics are glued to the bottom side of the track and excited so that they produce a moving wavetrain. The disposition of the ceramics on the track is not unique. An approach commonly used in the travelling wave motors developed by the Matsushita Research group [11,12] is to generate a travelling wave by actually producing two standing waves and carefully phasing them so that their resultant is travelling. This approach requires a symmetric disposition of the piezo ceramics. Usually one side of the track is in charge of driving one of the standing waves, while another set of piezos mounted on the opposite side of the track, drive the second standing wave. The phasing between both sets of piezos is accomplished by allowing a physical separation between both sets of piezos equivalent to a quarter of the wavelength of the travelling wave. See Figure 13.

Another way of implementing two standing waves is to collocate the piezos responsible for driving the different standing waves by mounting them one on top of the other. The phasing between the standing waves is once again accomplished by physically displacing one set of piezos by a quarter wavelength relative to the other. This configuration, however, is impractical, since access to the lower layer of ceramics is restricted once the top layer is mounted. Collocation can also be achieved by setting the two banks of piezos side by side along the width of the track.

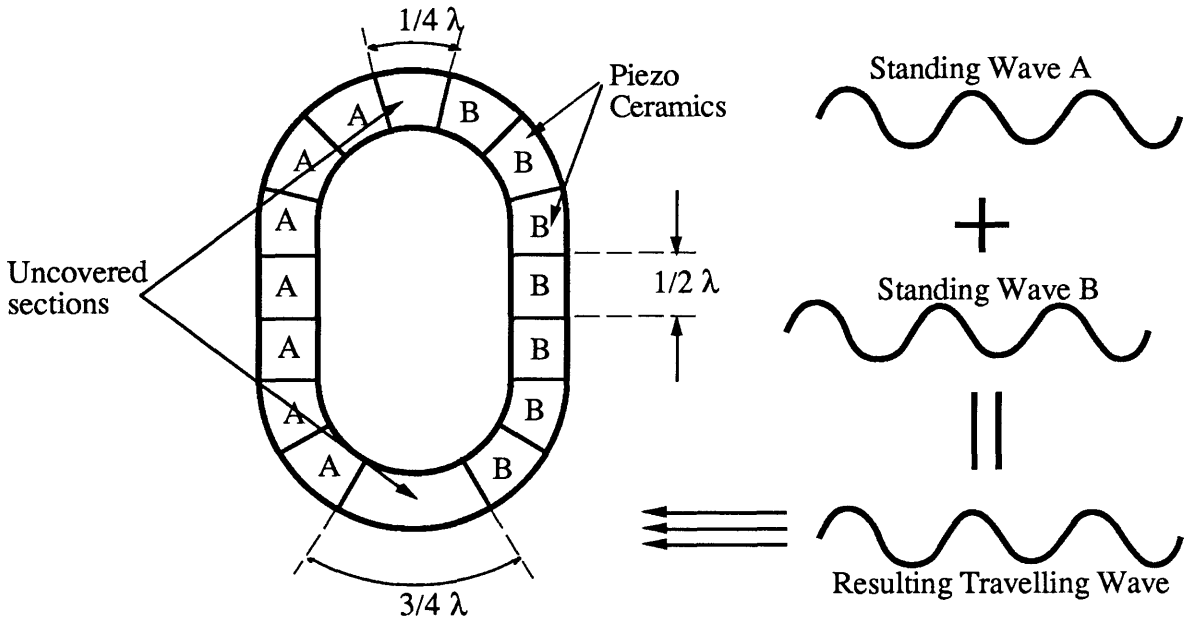

Figure 13- Piezo Layout Configuration which Drives Two Standing Waves Phased Which Results in a Travelling Wave. Piezo ceramics labeled with an A drive one of the Standing waves, while those ceramics labeled with a B drive the other standing wave.

A simpler way of driving the travelling waves along the motor is to cover the whole bottom side of the track with piezo ceramics and to drive them in a sequential manner to generate a rippling effect which thereby produces the travelling wave. The piezo ceramic segments are a quarter wavelength in length and have the same width of the track. Each segment is driven by a different electrical signal : a sine, a cosine, a negative sine, and a negative cosine wave respectively. The electric signals are exactly in phase relative to each other. This pattern is repeated throughout the length of the track an integer amount of times such that there is an integer amount of wavelengths being generated by the track. Figure 14 illustrates schematically a portion of the track being excited by piezo ceramics. The letter under the ceramics indicates which electrical signal is driving that portion of the track. An **s** corresponds to a sine wave, a **c** to a cosine wave, a **-s** to a negative sine wave and a **-c** to a

negative cosine wave. Figure 13 also illustrates how the superposition of these four signals leads to a rippling effect which corresponds to a travelling wave moving along the length of the track.

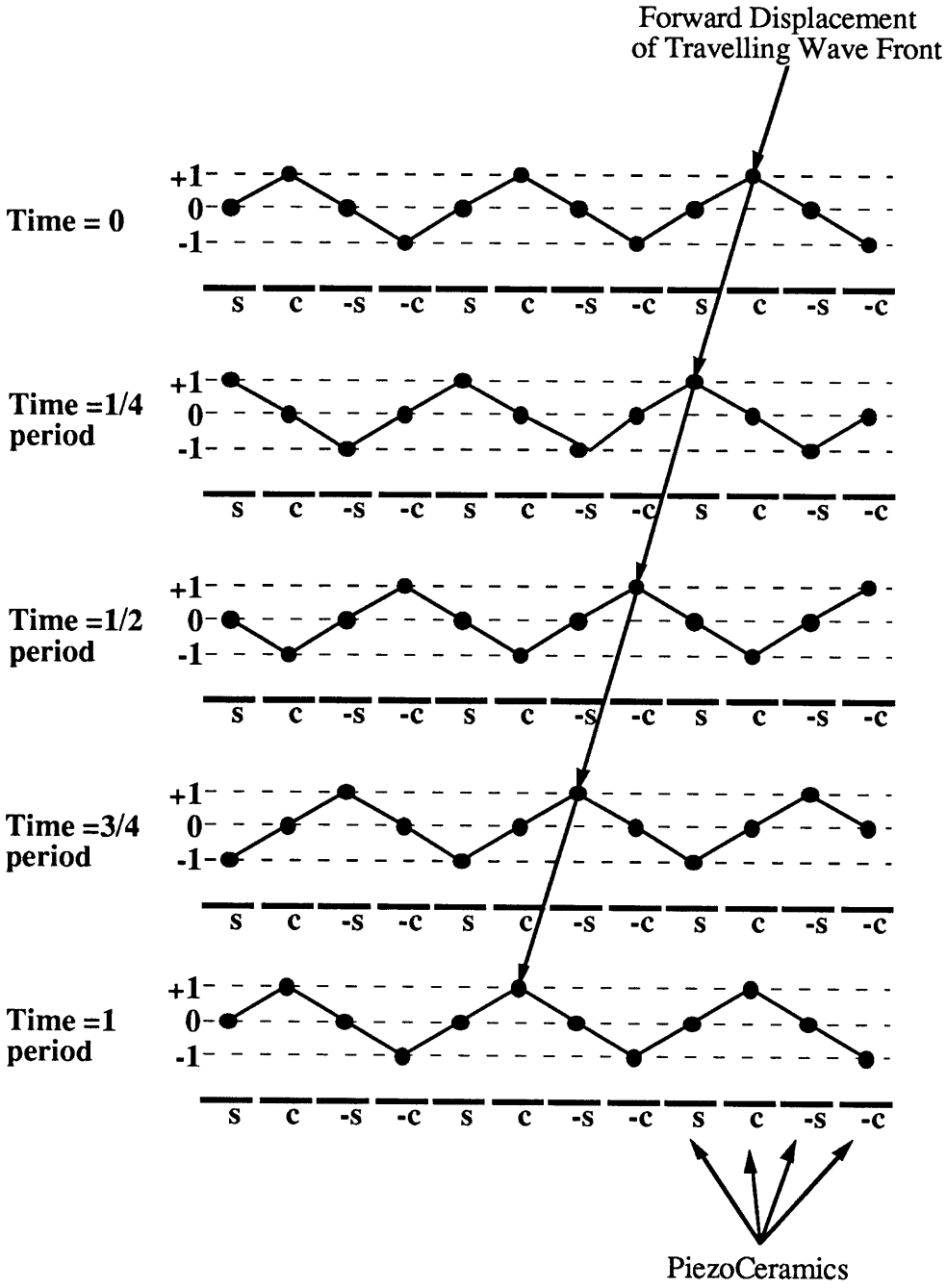

Figure 14- Schematic Representation of a Portion of the Track Undergoing Excitement by Piezo Ceramics. In One Full Cycle, the Wave Pattern Displaces Itself by One Wavelength.

This last piezo ceramic configuration was chosen since accurate alignment between the piezos and the track is not required. Furthermore, this configuration also permits the even distribution of piezos throughout the whole surface of the track. This eliminates the problem of having cross sectional discontinuities along the track such as portions of the track being made of aluminum and ceramics while other portions of the track are made entirely of aluminum. Discontinuities along the track are to be avoided since they represent junctions at which wavetrains can undergo scattering.

As the operating frequency of the motor is increased the length of the wavelength in the track decreases. Since this ceramic layout configuration requires four piezo etchings per wavelength and since there is a practical limit to the size of piezos that can be etched using available technology, there is therefore a practical limitation to the operating frequency of the motor. From a design perspective, the operating frequency of the motor has to be selected such that the wavelength of the waves is at least six times the thickness of the track as well as large enough to allow four piezo segments to be accurately etched.

Corrections due to Piezo Layer

The dynamic analysis of the various segments of the track has neglected to take into account the presence of the piezoelectric ceramics attached to the track as well as the glue layer bonding them together. In order to model more accurately the dynamic behavior of the racetrack, the track's overall stiffness, torsional rigidity and mass per unit length values were adjusted to take into account the presence of the piezo ceramics. The ceramics were thin, not more than 10% of the total thickness of the aluminum track. The effects of the glue layer between the aluminum track and the ceramics was neglected.

Given the material properties of the G1195 piezo ceramics used (see Appendix 5), the mass per unit length of the composite (ie- aluminum and piezo) race track was evaluated using an area weighted average of its mass densities as follows:

$$\rho A = \rho_a bh + \rho_p bh_p \tag{35}$$

where: ρA = mass per unit length of the composite track

ρ_a = density of aluminum

ρ_p = density of G1195 piezo ceramics

h = thickness of the aluminum track

h_p = thickness of the piezo ceramic layer

b = width of both the track and the piezo ceramic layer

Similarly, the overall moment of inertia, **I**, of the composite beam was reevaluated about the composite centroidal axis using a modulus weighted formula. The shift in the centroidal bending axis due to the presence of the piezo ceramic layer was estimated as follows:

$$z_{cl} = \frac{\left(rh_p^{\,2} + 2hh_p + h^2\right)}{2\left(h + h_p r\right)} \tag{36}$$

where : zcl = shift of the centroidal bending axis

r = ratio of the modulus of elasticity of aluminum and the piezo ceramic such as defined by :

$$r = \frac{E_{piezo}}{E_{aluminum}}$$

The bending moment of inertia of the composite beam about the N centroidal axis was then evaluated by:

$$I^* = \frac{bh^3}{12} + bh\left(z - \left(h_p + \frac{h}{2}\right)\right)^2 + \frac{brh_p^3}{12} + rbh_p\left(z - \frac{h_p}{2}\right)^2 \qquad (37)$$

where : I^* = bending moment of inertia of composite track

The racetrack's polar moment of inertia was estimated by assuming that the ratio of the modulus of elasticity between the composite beam and the aluminum beam was the same as the ratio of their torsional stiffness. Hence the value for the polar moment of inertia of the composite track was approximated by using the following expression:

$$J^* = \frac{I^* J}{I} \qquad (38)$$

where : J^* = polar moment of inertia of composite beam

J = polar moment of inertia of aluminum beam

The modified values of E, I, and J as derived in this section were used in all calculations including the ones from preceding sections.

Design Iteration Procedure

Given the overall configuration of the motor and having selected Aluminum as the material for its construction, the remainder of the design process consisted in selecting the dimensions of the track and evaluating its performance according to the models developed in the previous section. These last steps were performed in an iterative fashion until a motor design feasible to be constructed at our labs was arrived at. Figure 15 shows a block diagram of the steps involved in the design iteration process.

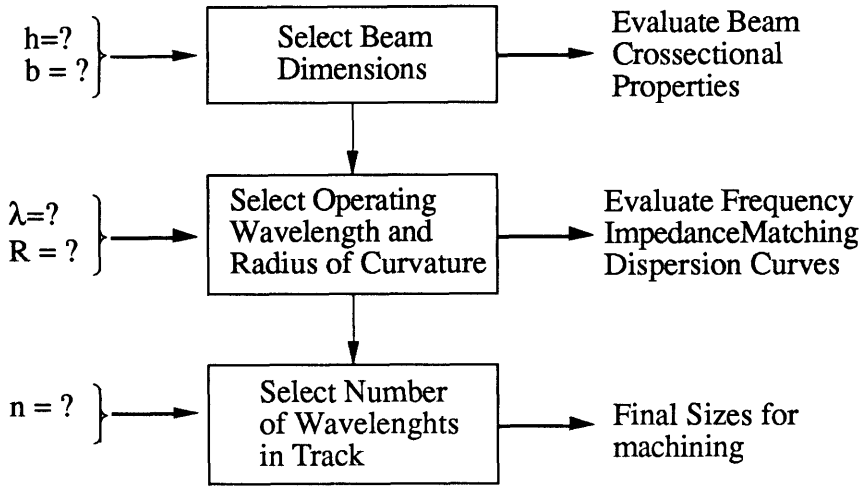

Figure 15- Block Diagram of Design Iteration Process

The first step involves choosing the cross sectional dimensions of the track. Once **h** and **b** are selected, all other relevant cross sectional properties of the track can be evaluated. Further analysis then demands that the cross sectional properties of the track be adjusted to take into account the influence of the piezo ceramics glued on the bottom side of the track. Having obtained estimates on the bending and torsional stiffness of the composite track it is necessary to predict the maximum static deflection that can be achieved by a beam of the prescribed dimensions. If the thickness of the piezo ceramics relative to the aluminum track is too small, the piezos may not have the authority to command the necessary deflection needed to attain a given operational speed. Since the dynamic amplification obtained by operating the track at resonance is unknown, the static deflection alone should be capable of attaining the selected operational speed of the motor. Hence, once in operation, the true speed attained by the motor will be greater than the design speed. Appendix 7 contains a description of the model used to describe the forces on the track due to the piezo actuators and shows the procedure used to estimate its static deflection.

The next step in the design process involves selecting a value for the operating wavelength, λ, the radius of curvature, **R**, and the number of wavelengths, **n**, contained in the track as measured along the centerline.

The lower limit on the value of λ was defined by our ability to accurately etch the four piezo segments per wavelength necessary to drive the travelling wave in the motor, and the thickness of the track. The higher limit on λ was imposed by the results of the dispersion curves, which suggested that λ should be much smaller than the radius of curvature, **R**, of the circular segments of the track. Selecting a value for the wavelength given the cross sectional dimensions of the track implies, according to equation (11), selecting the operating frequency of the motor.

The value of **R**, as stated above, is constrained to be larger than the value of λ. Once a value is selected, the dispersion curves for the circular sections can be plotted and the operating frequency can be identified on the plots. Furthermore, a scattering matrix for the junction, between the straight and curved sections of the track, can now be calculated and the transmission properties of the junction can be quantified. As stated in the previous sections, a larger value of R will reduce the impedance matching problems at the junction between the straight and curved sections of the track, as well as diminish the amount of scattering of the wave forms.

The value of **n** describes the number of complete wavelengths that fit along the centerline of the racetrack. Therefore, **n**, has to be an integer so that the racetrack can operate at resonance. Having selected **h**, **b**, $\mathbf{h_p}$, **R** and λ, the lengths of the circular portions of the track are known. By selecting **n**, the length of the straight beams connecting the circular portions of the track becomes fixed. At this point, all dimensions needed to construct the motor have been determined. If the predicted performance of the track is not satisfactory, the previous steps can be repeated until a suitable configuration is attained.

Final Dimensions and Sizing

Through the design iteration process described above, a final, linear travelling wave motor configuration was arrived at:

The proposed travelling wave motor is designed in the shape of a racetrack: it consists of two straight beams interconnected by two semicircular beams. The track is made out of a single piece of Aluminum (2024) and has a total length of 29 inches when measured along its centerline. The motor is designed to operate at a resonant frequency of 27300 Hz, and a wavelength of 1.00 inch. The cross sectional dimensions of the track are the following:

Thickness of track (**h**)	= 0.002 m	= 0.08 inches
Thickness of Piezos ($\mathbf{h_p}$)	= 0.000191 m	= 0.0075 inches
Width of track (**b**)	= 0.0127 m	= 0.5 inches
Effective Stiffness (**EI**)	= 1.3006 N-m^2	
Effective Mass/Length (ρ**A**)	= 0.10643 Kg/m	

Given these cross sectional dimensions, the (static) amplitude of the travelling waves for an applied voltage of 31 volts, can be estimated at:

Static Deflection ($\mathbf{w_{mid}}$)	= 8.349 x 10^{-8} m

This amplitude corresponds, at the operating frequency, to a design speed of 0.16 inches per second.

The selected values for **R** and **n** were the following:

Radius of Curvature (**R**)	= .0570 m	= 2.246 inches
Number of Wavelengths (λ)	= 29	

Figure 16 shows the dispersion curves for the circular segments of the track, using the selected design values. The vertical dotted lines correspond to the operating frequency of 27300 Hz. It is apparent from the figure that the operating frequency is sufficiently far away from the cutoff frequency of the transverse mode of the curved track.

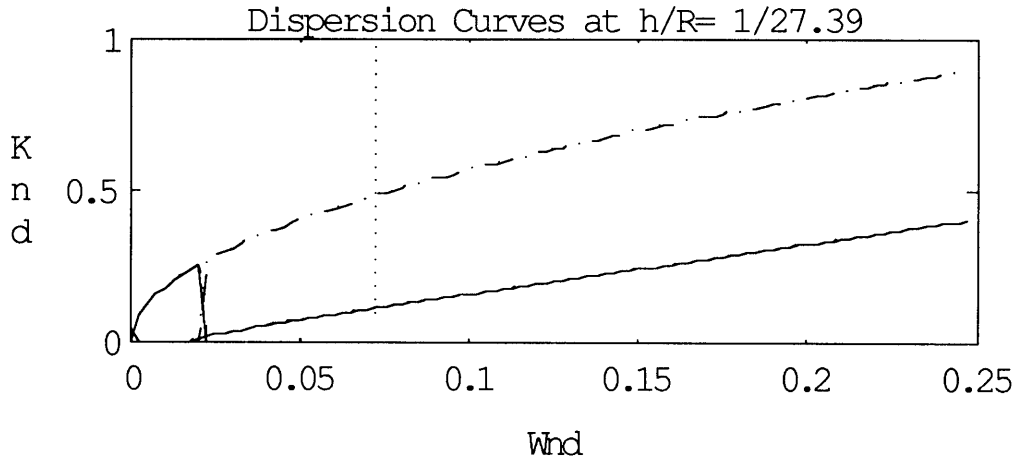

Figure 16 - Dispersion Curves for the Circular Sections of the Motor. The Dotted Vertical Line Corresponds to the Motor's Operating Frequency.

A scattering analysis of the junction between the straight and curved sections of the motor, resulted in the following scattering matrix (magnitudes only):

0.9951	0.0025	10.7458	**0.0025**	0.0018	10.7521
0.0030	**1.0032**	14.3514	0.0030	**0.0044**	13.5971
0.0001	0.0002	**0.9832**	0.0001	0.0000	**0.0160**
0.0025	0.0025	10.7741	**1.0049**	0.0019	10.7820
0.0006	**0.0004**	13.5600	0.0006	**0.9926**	14.3283
0.0001	0.0000	**0.0120**	0.0001	0.0002	**1.0126**

The highlighted values along the main diagonal indicate that the junction's transmission efficiency is very high, while the highlighted values along the secondary diagonals confirm this finding by indicating that reflection rates among similar wave modes are very low. The

fully populated matrix indicates that there is coupling between the transverse and torsional modes, but given the values along the main diagonal, we expect this coupling to be small.

Both the dispersion curves and the scattering matrix analysis suggest that the designed travelling wave motor will perform satisfactorily.

Note: There are some values along the main diagonal which are greater than one. This is due to numerical round-up error. The values along the diagonal cannot be greater than one since they represent transmission efficiencies.

Electric Circuit Design

The motor's driving circuitry is responsible for exciting the piezoelectric ceramics attached to the aluminum track, thereby generating the travelling waves in it. Figure 17 illustrates a functional block diagram of the driving circuitry. The output of a variable frequency signal generator is used as a timer for the quadrature circuit which produces four sine waves shifted by 90 degrees in phase, relative to each other. These signals are amplified and sent to the corresponding piezo ceramics on the track.

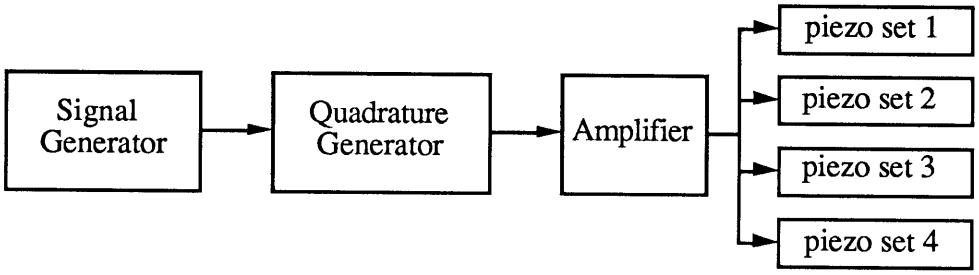

Figure 17- Functional Block Diagram of Driving Circuit

The circuit is designed to operate in an open loop configuration. The frequency of the electrical signals driving the piezo ceramics is controlled by the signal generator. The signal generator has to be adjusted manually until the racetrack achieves mechanical resonance. Further details of the driving circuitry can be found in Appendix 1.

Construction and Assembly

The construction and assembly of the various parts of the motor can be divided into three stages: the machining of the track and of the sliders, the integration of the piezos onto the track and finally, the wiring of the various electronic components together with the track and their integration into a working ultrasonic motor.

Metallic Parts: The track was machined out of an aluminum 2024 plate to the specified thickness of 80 milli-inches. In order to do this, a 1/8" aluminum plate was glued onto the machine polished surface of a 1/2" aluminum plate using contact cement. The assembly was then mounted onto a milling machine which machined the 1/8" aluminum plate to the desired thickness. The size of the cut in each pass was kept small, so that the cutting force on the tool bit as well as the machining stresses on the plate were minimized. A small cut size also prevents the 1/8" plate from coming prematurely unglued from the 1/2' base plate.

The whole assembly was then removed and taken to a programmable milling machine which carved out the racetrack to the dimensions specified in the construction diagrams of Appendix 4. Once the track had been cut out, the whole assembly was submerged in acetone so as to dissolve the contact cement and allow the track to come off freely. Having completed this, the oval track was deburred and its surfaces were polished with a 500 grade sandpaper.

The next parts to be machined were the sliders. These were made out of either Aluminum 2024 or out of of Plexiglass, and they did not require of any special machining procedures. The sliders were designed to offer a variety of surfaces to be tested on the track. Figure 18 shows some of the different slider configurations used. "Flat Sliders" and "Slotted Sliders" were built of varying length relative to the wavelength of the travelling

waves The slotted sliders were identical to the flat ones except that they concentrated all their weight on two rails.The construction diagrams for the sliders can be found in Appendices 3-b and 3-c.

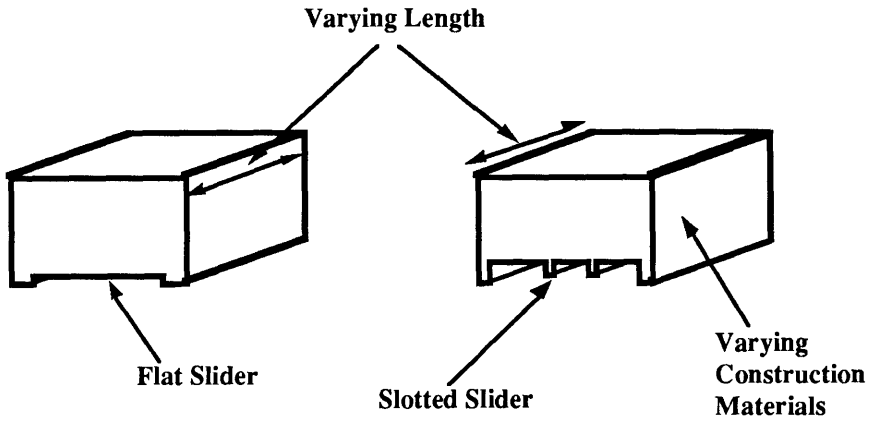

Figure 18- Various Slider Configurations Showing Their Lower Surface Geometries and Their Varying Lengths

Piezo Ceramic Assembly: Once the track was completed, it was sent to Piezo Systems Inc. to be covered with G1195 piezo electric ceramics. The G1195 ceramic has a 7.5 milli-inches thickness and is manufactured in 1.5" by 2.5" rectangular tiles. See Appendix 5 for further piezo ceramic specifications.

The piezoceramics were cut out into smaller sections and placed on the track so as to cover its whole surface. Ideally, the whole surface should be covered by a single piezo crystal in order to avoid discontinuities along the track. However, since this is not possible with available technology, we proceeded to minimize the effect of the discontinuities on the travelling waves by ensuring that the joint between any two piezo ceramics was never perpendicular to the centerline of the track.

The piezo ceramics were bonded individually to the the track using a 24 hour 60° C curing process. Once the track was covered, the ceramics were sanded down flush with the

aluminum track. Connectivity between the various piezos and the aluminum track was verified.

The ceramics were then etched at quarter inch intervals. This amounts to 4 etchings per wavelength or 116 etchings along the whole track. After completing the etching, the plating of the piezos was polished and the ceramics were individually checked for cross connectivity. The piezos were assumed to be electrically isolated from each other if the resistance between neighboring etchings was in the order of 1000 MΩ.

Once the etching was completed, each piezo segment was to be wired to the fourth piezo segment next to it. The wiring was done using 26 gauge magnet wire and solid core solder. All 116 ceramics were thus electrically addressed by 4 concentric wire rings, each one soldered to 29 piezo ceramics. Each wire ring was then connected to the lead wires which provided the driving signals from the amplifiers. Figure 19 shows the track with the position of the piezo etchings as well as the position of the solder points and the wire rings.

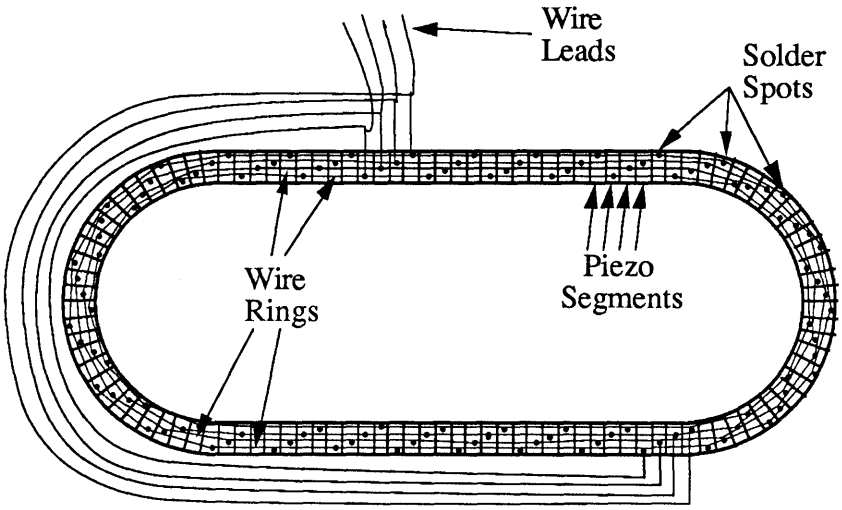

Figure 19 - Lower View of Racetrack. Etchings on the ceramic layer, are marked as well as the solder spots and the wires that interconnect the piezos electrically.

Having completed the soldering, the whole track was washed with water to remove any excess flux from the plating of the piezos, and then dried out with alcohol. Connectivity between the four lead wires and the surfaces of all the piezo ceramics was verified.

Final Assembly and Integration: Having completed the wiring of the piezos, the track was mounted onto an Aluminum base plate. In order to mechanically and electrically isolate the track from its base, the base was covered with a 1/16" black rubber sheet, and the track was then glued onto the rubber surface via a double sided foam tape.

The four leads of the track were connected to the four output stages of the Crown amplifiers. In order to protect the amplifiers, 3Ω power resistors were connected in series to the output of each amplifier. The inputs of the amplifiers were connected to the buffered outputs of the protoboard circuit. A signal generator serves as a variable frequency clock pulse for the quadrature circuit. The frequency of the signal generator is monitored by a frequency meter and the output of the amplifiers is monitored by an oscilloscope. Figure 20 shows an schematic representation of the experimental setup as described above.

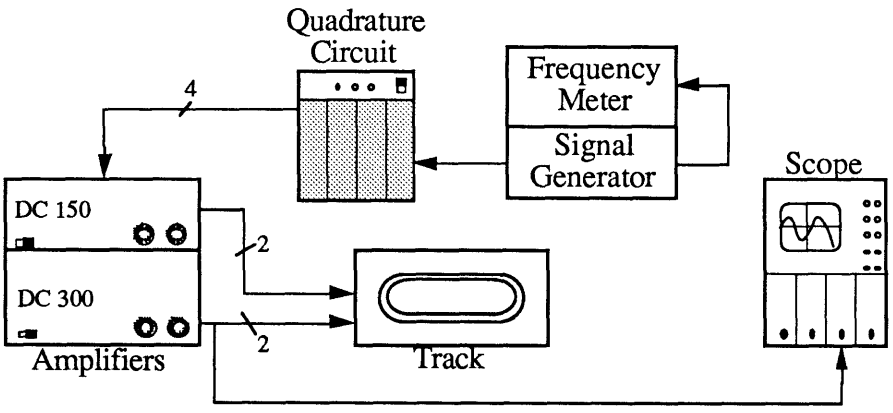

Figure 20- Schematic Representation of Experimental Set-up

IV- Experimentation and Results

The motor was subjected to a series of tests in order to quantify its performance, and compare its behavior to that predicted by theory. The tests consisted in operating the motor under a wide range of conditions and monitoring the changes in its performance in response to these particular conditions. This section will present the results of such tests as well as our findings on other phenomena encountered while performing the motor's evaluation.

Experimental Procedure

At the start of each test run, five experimental parameters were selected: the operating frequency of the motor, the peak to peak voltage of the driving signals leading to the piezo ceramics, the length of the sliders placed on the track, the mass of the sliders and the angle of inclination of the track. All parameters were varied throughout the testing period except the peak to peak voltage level which was set to a constant value of 20 Volts for all tests. The operating frequency of the motor could be varied by adjusting the frequency of the signal generator. The mass of the sliders could be modified by simply adding weights to the top surface of the sliders. Several sliders of different lengths were machined out of both aluminum and Plexiglass. This enabled us verify the effects of slider length and texture on the performance of the motor.

The tests were aimed specifically at characterizing the resonant effects of the system, determining the force, power and efficiency curves of the motor, and establishing whether or not the designed motor had successfully decoupled the transverse and torsional vibrational modes of the track.

Data acquisition was limited to obtaining the following measurements:

- Velocity measurements of the various sliders.
- Force measurements on the various sliders.
- Electrical readings, and
- Strain and temperature measurements of the top surface the track.

Velocity Measurements of Sliders :

The velocity of the various sliders and other objects placed on the track was measured differently depending on the length and weight of the slider, and of the operating frequency of the motor. The average velocity of the sliders at a given frequency, was estimated by measuring the time needed to complete a lap around the track. The sliders were allowed to travel several laps and their corresponding lap times were compared to each other. If these times were consistent with each other, the measurements were deemed satisfactory. Certain combinations of weight, length and operating frequency, however, did not allow for this type of measurement. The sliders were occasionally unable to complete a lap in a repeatable fashion. In these situations, the velocity of a slider was estimated by measuring the time taken by the slider to travel between two markers of known separation, along the straight portions of the motor.

Sliders that were longer than one inch encountered occasional difficulty in travelling around the circular portions of the track. As a result of this, the slider would jam at an arbitrary position for a given length of time and then resume its forward motion. Sliders heavier than 0.3 Kg also showed the same erratic behavior along the circular sections of the motor. The "excessive" weight seemed to hinder the slider's ability to move about the width of the track and avoid getting stuck along the curves. Velocity measurements taken under either of these circumstances were voided.

In theory, the velocity of an object on a linear travelling wave motor depends only on the operating frequency of the motor and the amplitude of the waves. The amplitude of the waves is in part controlled by the voltage used to drive the piezo electric actuators on the track. During the testing period, all signals actuating the piezo ceramics were kept at a 20 Volts (peak to peak) level. The amplitude of the waves is also in part determined by the operating frequency of the motor. Because of resonance, the amplitude of the waves depends upon the driving frequency of the motor. At or near resonance, the amplitude of the waves increases dramatically because of dynamic amplification. The velocity of a slider, thereby, increases in the vicinity of resonance. The most consistent velocity measurements were taken at frequencies close to resonance. As the operating frequency drifted away from resonance, measurements became noisier and the sliders would once again jam along the curved portions of the track and the measurements had to be annulled.

Force Measurements of Sliders:

The maximum (stalled) side force exerted by the motor on the sliders was estimated by measuring the extension, due to this force, of a calibrated spring. The spring was attached to the inertial frame of the base on which the racetrack rests, and to a slider resting on top of the track. By varying the mass of the slider, the magnitude of the side force also varied proportionally. These fluctuations were recorded as changes in length of the spring.

The side force exerted by the motor was also measured indirectly by tilting the base plate, on which the racetrack is mounted, to various specified angles. A slider placed on the track would be allowed to move along the straight segments of the track. The slope of the track would then be increased until the slider was no longer capable of moving up and would remain fixed in whatever position it was placed. Both the angle of inclination of the track and the mass of the slider were recorded. This exercise was repeated with sliders of different mass and length.

Electrical Readings:

Voltage readings were obtained directly from the output stage of the amplifier. Current readings were obtained indirectly by measuring the voltage differential across a 1Ω precision resistor connected in series with the signals driving the motor.

Surface Measurements:

Both a strain gauge and a thermometer were placed on the upper surface of the racetrack to provide information concerning the amplitude of the travelling waves and the amount of energy being dissipated as heat into the racetrack.

A strain gauge was glued onto the upper surface of the racetrack as shown in Figure 21. The gauge aligned along the straight segment of the track measured the strain caused by the passage of transverse travelling waves. The gauge aligned across the width of the track allowed the detection of standing wave patterns occurring across the width of the track. The third gauge aligned at a 45 degree angle from either of the previous gauges, allowed the estimation of torsion deformation of the straight segments of the track.

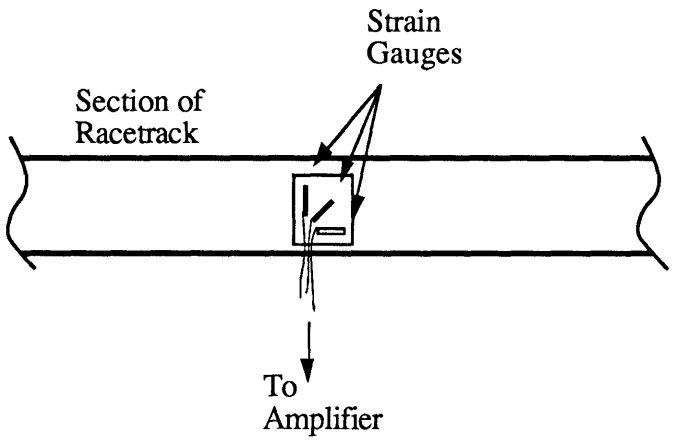

Figure 21- Strain Gauge placement along straight segment of track.

Results and Discussion

Resonant Behavior of the Motor

Figure 22 shows the frequency response of the motor over a bandwidth centered about its resonant frequency. As shown in the figure, the motor resonates at a frequency of 27230 Hz. This figure is a quarter of a percent lower than that predicted by theory : 27300 Hz.

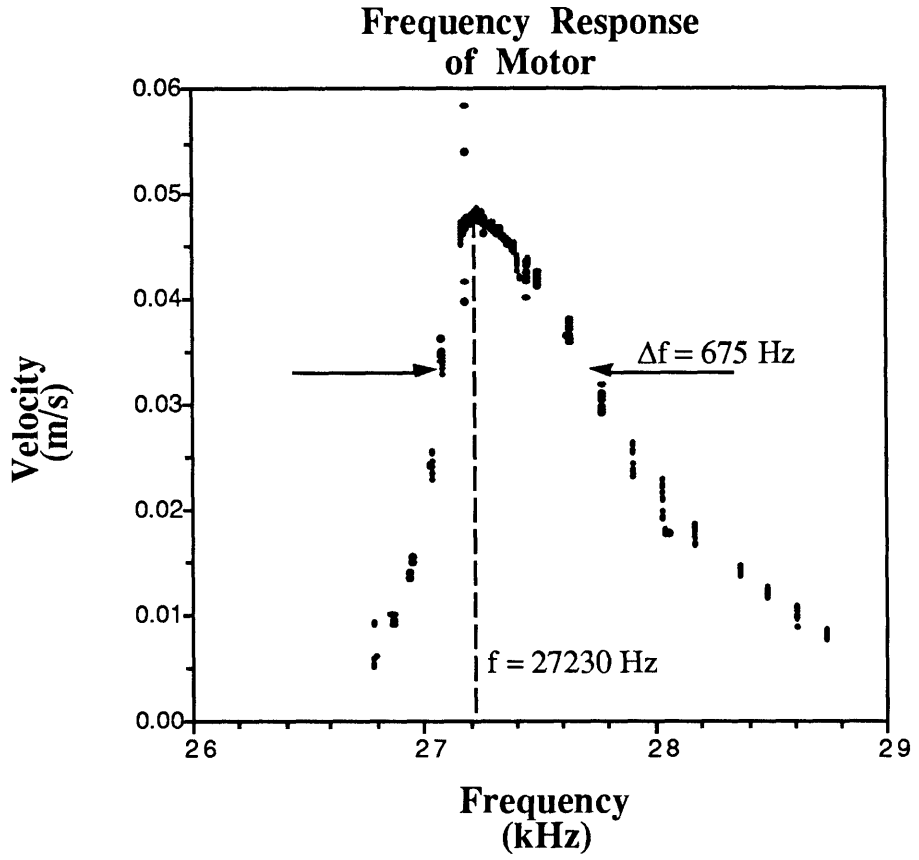

Figure 22- Frequency Response Plot of Motor. The data points correspond to test runs performed on a quarter inch long, Plexiglass slider of constant ,mass.

As a comparison, the resonant frequency of the motor was also determined by measuring the frequency at which the current drawn by the motor reached a maximum. This

phenomenon occurred at 27130 Hz, which is 0.62% lower than the predicted value of 27300 Hz.

The experimental decrease in the track's resonant frequency is probably due to the unmodelled increase in mass attributable to the 116 solder points and wires attached to the lower side of the track. Their presence increases the track's effective overall density which according to equation (11) will force the resonant frequency down. On the other hand, a 1% error on the estimate of a resonant mode is small enough to be attributed to discrepancies between the reported values of the modulus of elasticity, and density of the construction materials, and their actual values or simple measurement errors.

From Figure 22, it is apparent that dynamic amplification due to resonance greatly enhances the performance of the motor. At frequencies below 26750 Hz and above 28750 Hz, the amplitude of the travelling waves had decreased to the point where the motor was not capable of displacing any objects on its surface. Hence, no data was gathered at these operating frequencies.

It is common to characterize the dynamic amplification achieved by a system operating at resonance by the parameter **Q**, which is defined as follows:

$$Q = \frac{\omega_n}{\Delta\omega} = \frac{1}{2\xi} \tag{39}$$

where: ω_n = Natural frequency of the system

$\Delta\omega$ = Width of the frequency response curve measured at an rms value of the peak value.

ξ = damping ratio as defined for a second order system

The parameter **Q**, meaning Quality, can also be described as the amplification factor relating the output of a system when driven statically to its output when driven at resonance. From the data available, three separate estimates of the **Q** of the motor can be

obtained. The first estimate can be obtained using equation (39) and Figure 22. By reading off the values for ω_n and $\Delta\omega$ from the figure, we obtain an estimate of $\mathbf{Q} = 40.34$.

The other estimates of Q can be obtained by taking the ratio of the measured amplitude of the travelling waves when the motor is operating at resonance, to the amplitude of the waves when driven statically. Waves, however, cannot measured when driven statically, but an estimate of the track's static deflection due to the piezo actuators can be obtained using simple beam theory. Applying the method described in Appendix 5, the static amplitude of the traveling waves was estimated at $y_0 = 8.99 \times 10^{-8}$ m.

The amplitude of the travelling waves at resonance can be inferred by measuring the top velocity achieved by a slider on the track, or by by measuring the strain of the top surface of the track while the motor is in operation. The top velocity of a slider was measured from Figure 20 to be 0.048 m/s. Given this figure, equation (7) estimates the amplitude of the travelling waves to be $y_0 = 1.05 \times 10^{-6}$ m, which implies a Q value of 11.65.

The maximum strain measured in the direction along the length of the track was 180 microstrain. Using similar assumptions to those used for the estimate of the static deflection of the track (see Appendix 5) we can show that :

$$\varepsilon = -w'' z \tag{40}$$

where:

$$w''_{(x)} = -k^2 w_{mid} \sin(kx) \tag{41}$$

Hence by solving for w_{mid}, we obtain an expression which converts strain information to amplitude information :

$$w_{mid} = \frac{\varepsilon\lambda^2}{2\pi^2 h} \qquad (42)$$

Applying equation (42) to the strain data, we can estimate the amplitude of the travelling waves: $y_o = 1.3625 \times 10^{-6}$ m. This amplitude implies a value for Q equal to 15.1.

It was later discovered, after suspending the track in mid air and removing the foam tape attached to it, that a large amount of power was being drained into the rubber base of the track as well as the foam tape. It is possible that the foam and the rubber were adding damping to the track, which would suggest that without them, the track would have a much higher Q.

Force Capabilities of Motor

The side force exerted by the track on the sliders, causing them to move along the length of the track, is proportional to the normal force of the sliders on the track. It was discovered, however, that there were some practical limits to the normal forces and slider geometries that could be tested on the track under regular laboratory conditions. If the mass of the sliders exceeded 0.35 Kg, the surface of the track became marred with scratches and irregularities. When using aluminum sliders on the aluminum track, cold welding between them would cause further damage to the surface of the track. In order to preserve the integrity of the track's surface, high normal forces on the track were avoided. All force measurements were conducted while operating the motor at resonance.

As shown in Figure 23, the velocity of the sliders tends to decrease slightly as the normal force on the track is increased. In the limit, as the mass of the sliders is increased,

the waves supporting the sliders appear to get distorted to the point where the track is not able to deflect against the weight of the sliders. At this point the sliders effectively "squash" the waves underneath them. A decrease in the local amplitude of the waves due to this "squashing" effect, could therefore explain the observed decrease in speed. On the other hand, this decrease in speed could also be explained by the fact that as the mass of the sliders was increased, their sideways motion was constrained, making it difficult for them to go around the curved sections of the track. The maximum weight capable of being displaced by the motor is yet unknown, since it would require damaging the surface of the track as well as the driving piezoceramics attached to it.

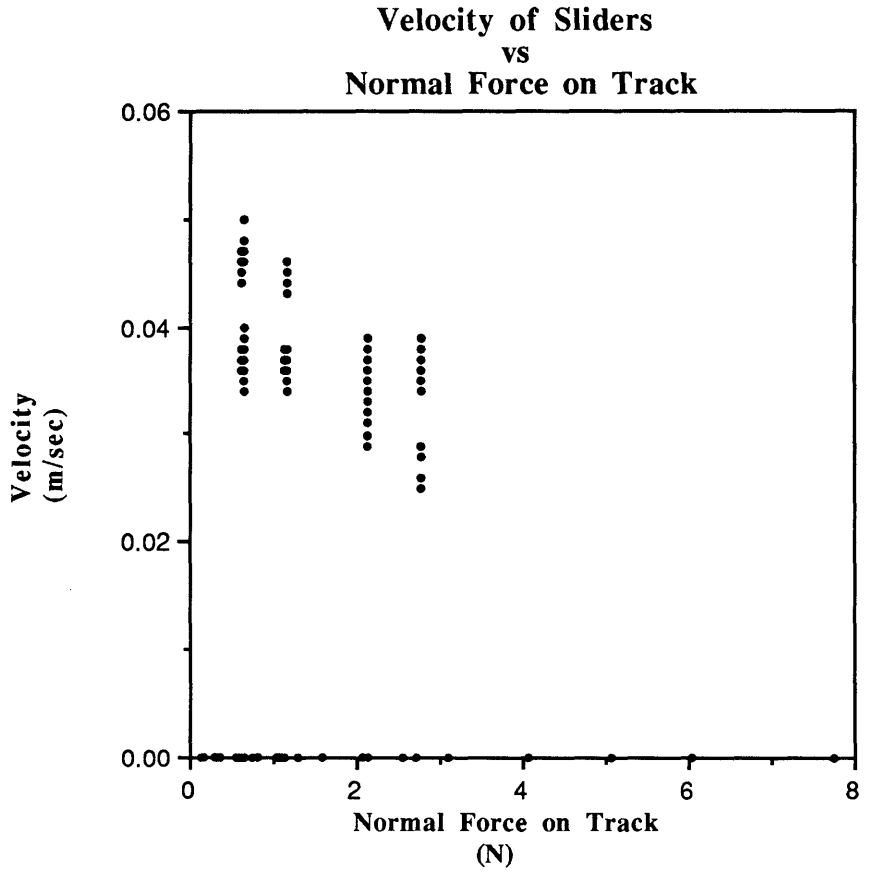

Figure 23- Measured Velocity of Sliders versus Normal Force On the Track. Operating Frequency : 27.23 kHz

The other practical limitation encountered while testing the track under regular laboratory conditions was using sliders that were very light and that had a large contact surface area. These "flat sliders", (see Appendix 3-b for drawing) would tend to hover at a given position unless their mass was increased with extra weights, or the motor was placed inside a vacuum chamber. Once their mass was increased they would move along the track as the rest of the objects placed on it, but never quite efficiently as their slotted counterparts. The "slotted sliders" (see Appendix 3-c for drawing), had similar dimensions as the flat sliders, but their weight on the track was concentrated on two rails. These sliders would move along the along the track with no need of additional mass. The motor's observed behavior in a vacuum chamber will be addressed later in the discussion.

Figure 24 shows the maximum side force exerted by the track on the sliders as a function of the surface area of the sliders that is in possible contact with the track. There were three different sliders, which justifies the clustering of data along vertical lines. The various values of side forces for a given slider correspond to variations in mass of the slider and hence variations of the normal force exerted by the sliders on the track. As the mass of the sliders is increased the magnitude of the side force increases proportionally.

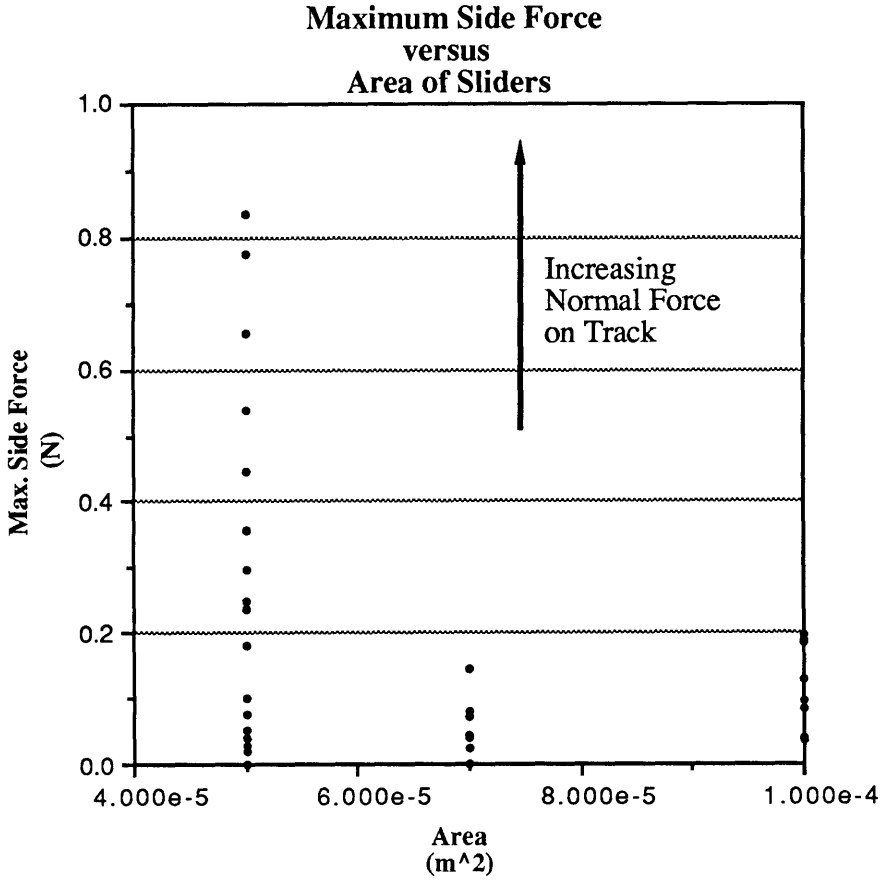

Figure 24- Maximum Side Force Exerted by Track on Sliders of Increasing Mass but Constant Surface Area. Operating Frequency : 27.23 kHz.

Figure 25 shows the dependency between the measured side and normal forces exerted on the sliders by the track. A least square, straight line curve fit of the data, approximates the slope of this curve to 0.0946 with a correlation factor of 0.589. The force coefficient for the motor, defined as the ratio between the maximum side and normal forces acting on the slider, is similar to a friction coefficient since it relates the normal component of the weight of a slider on the track, to the maximum side force exerted by the track on the slider.

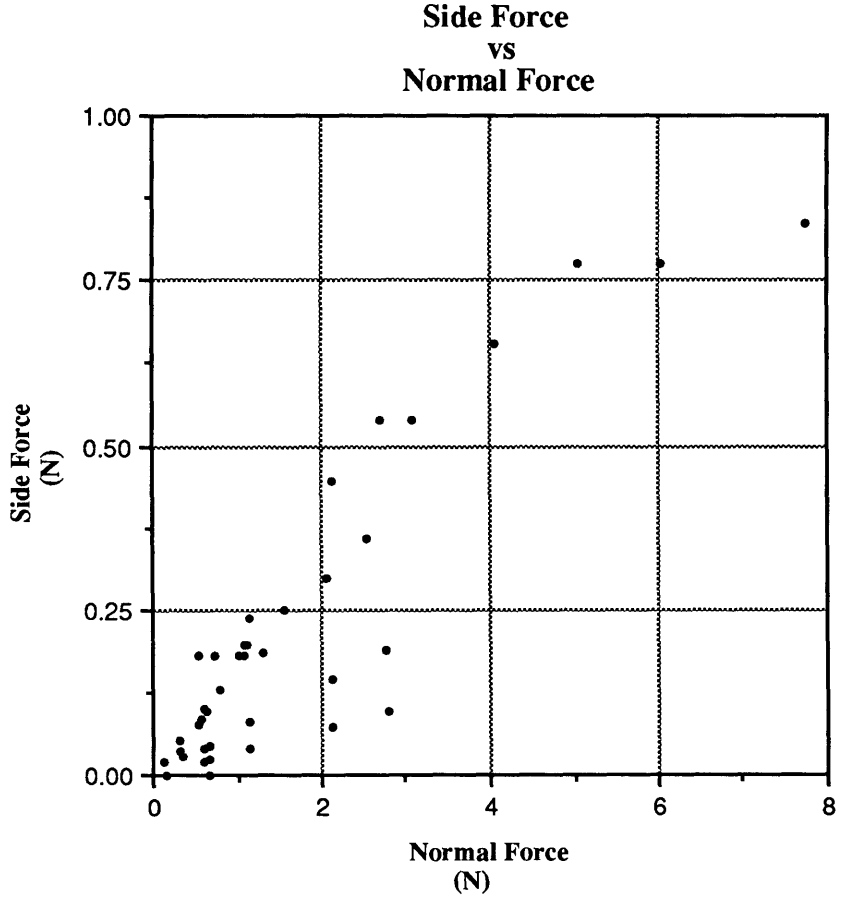

Figure 25- Maximum Side Force on Sliders versus Normal Force on Track. Operating Frequency : 27.23 kHz.

Figure 26 shows the dependency between side and normal forces on the sliders. In contrast to Figure 25, Figure 26 uses only those force measurements taken with the calibrated spring. The slope of this curve was estimated at 0.124 and has a correlation factor of 0.917. This suggests that the spring generates better data.

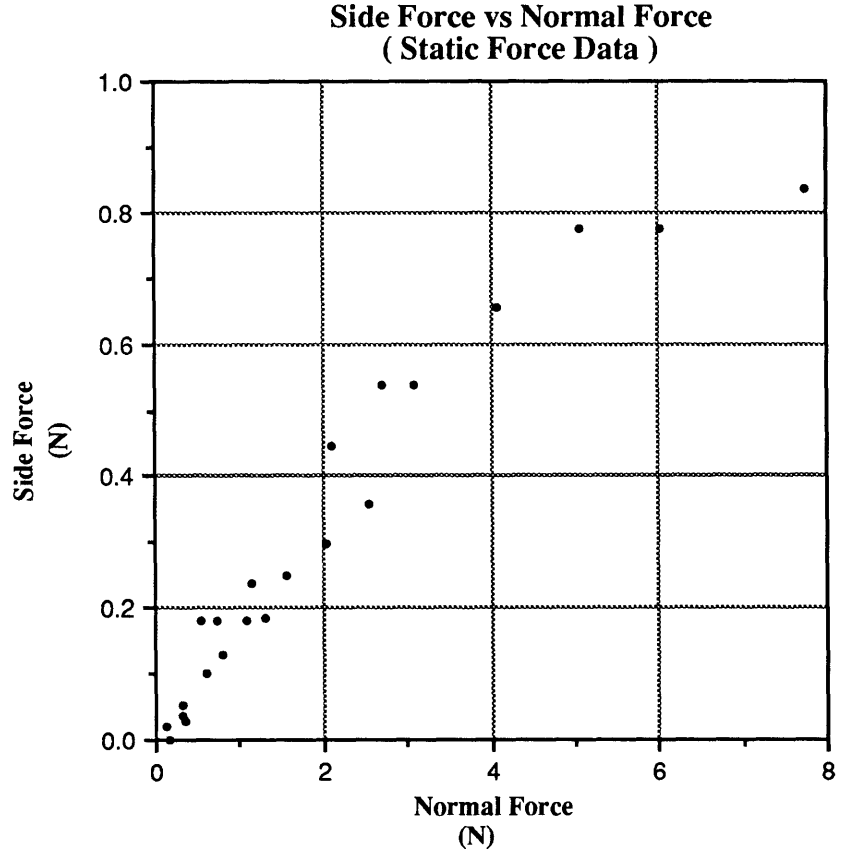

Figure 26- Maximum Side Force on Sliders versus Normal Force on Track. (force measurements only).

Figure 27 shows the relationship between the maximum side force acting on the sliders and the pressure exerted by the sliders on the track. Figure 27 contains the same data as Figure 25, except that the normal forces have been normalized by the surface areas of the corresponding sliders. By plotting the maximum side force as a function of pressure, Figure 27 appears less scattered than Figure 25. The correlation factor for the data in Figure 27 is 0.798.

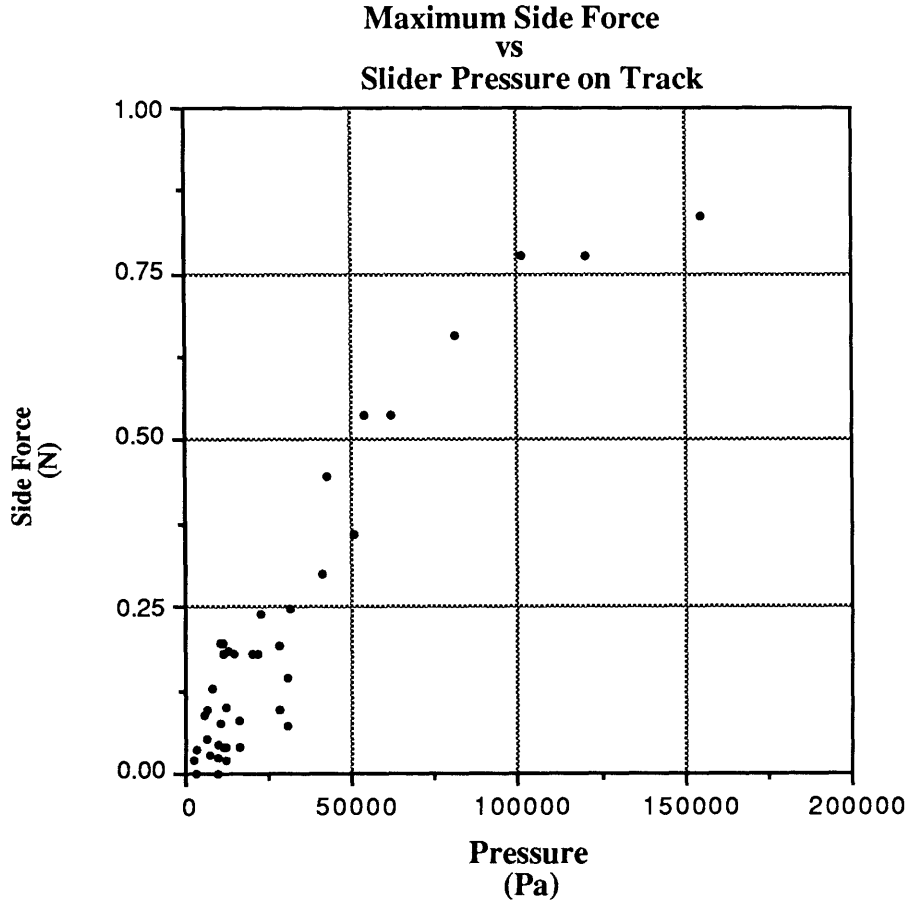

Figure 27- Maximum Side Force Exerted by Motor Versus Pressure Exerted by Slider

Figure 27 suggests that there is some correlation between the surface area of a given slider and the maximum side force exerted upon it. The side force exerted upon the sliders is frictional in nature, and hence according to simple (Coulomb) friction models, should be independent of surface area. In more elaborate models, surface area has a second order effect on friction. According to Rabinowicz, a doubling in surface area will lead to an approximate 10% increase in frictional force. The observations however, indicate that objects which exert a greater pressure (ie- have a smaller surface area per unit mass) on the track perform better and behave in a more predictable fashion. A possible explanation may be found in the effect of the air present in the interface between the track and the sliders.

Figures 25 through 27 suggest that the maximum side force exerted by the motor is linearly proportional to the normal force applied on the track by the slider. This may be a reasonable description of the operating range of normal forces to which the track was subjected to during the test period. However, as the normal force on the track is increased beyond the levels to which we tested it, the "squashing" effect on the waves would probably cause the curve to flatten out as illustrated in Figure 28. If the normal force is then increased further, the curve will intercept the x axis for a second time. At this limiting value, the normal force exerted on the track would not allow the piezo actuators to command a deflection in the track.

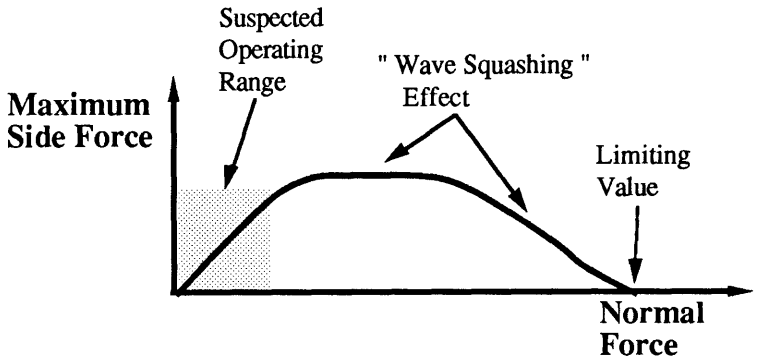

Figure 28- Conceptual Extension of the Operating Envelope of the Travelling Wave Motor. The shaded are represents the suspected range of Normal Forces Applied to the track during our testing procedures.

Figure 29 shows the force coefficient as a function of the normal force on the track. The average value for the measured force coefficient is approximately 0.1, with high values extending up to 0.33. Figure 30 shows the angle of inclination of the track at which the slider achieves static equilibrium versus the normal force of the slider on the track. The average value of this angle is approximately 0.1, with high values extending up to 1.8.

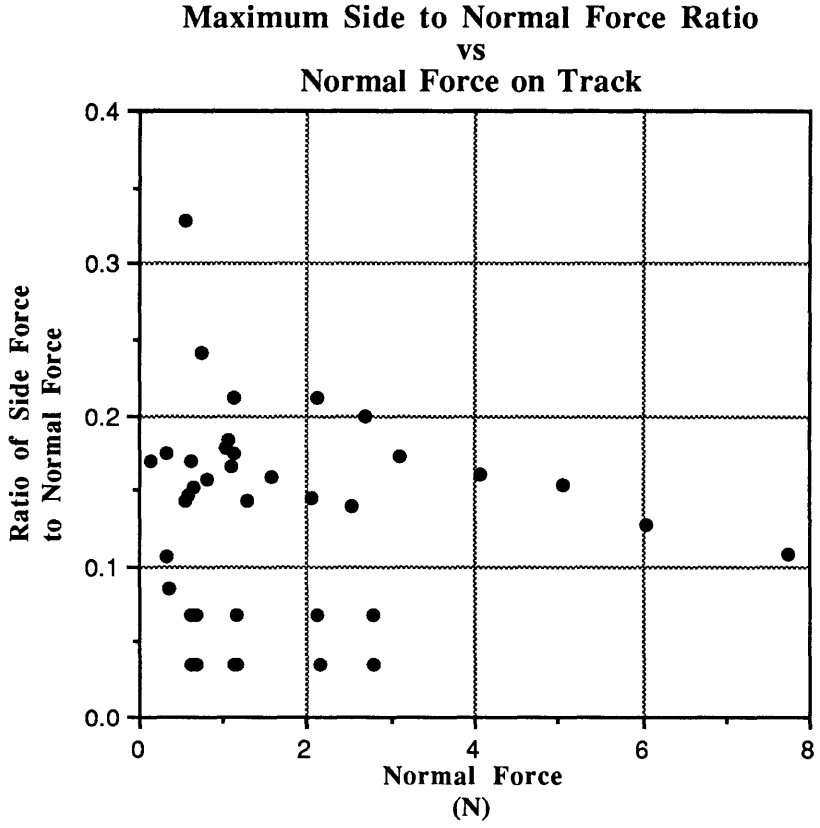

Figure 29- Force Coefficient of Motor (i.e- Ratio of Maximum Side Force to Normal Force) versus Normal Force on Track. Operating Frequency : 27.23 kHz.

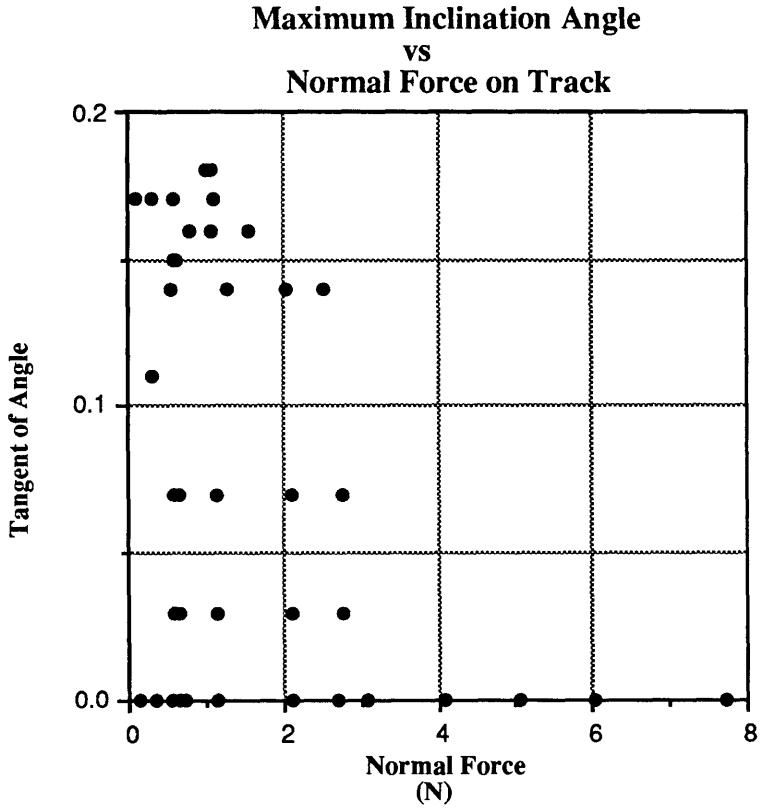

Figure 30- Maximum Angle of Track Inclination versus Normal Force on Track.

As shown in Appendix 7, the force coefficient of the motor should be identical to the tangent of the maximum angle of inclination of the track, yet by comparing Figures 29 and 30, we observe that some of the highest force coefficients values were achieved at angles of inclination equal to zero degrees. These data points correspond to force measurements obtained using the calibrated spring.

Similarly, it can be noted from Figure 30 that the maximum angle at which a slider will remain at rest on the track, is approximately 0.18 radians. If the travelling wave motor were turned off however, the track could be tilted to an angle in excess of 17 degrees (0.3 rads) and a slider would still remain at rest because of the high static friction coefficient between the aluminum surfaces of the track and the sliders.

It appears, based on this behavior, that the operation of the travelling wave motor somehow decreases the effective value of the friction coefficient between the track and the slider. As presented by Rabinowicz [13], the frictional force between two bodies is the result of the junctions formed between the two surfaces while they remain in contact with each other. When two surfaces slide over each other, these junctions have to be sheared. The frictional force is the force required to overcome the resistance of these junctions to shear. The junctions between surfaces appear regardless of the relative sliding velocity between them. The size of the junctions, however, increases proportionally to the amount of time the surfaces remain fixed to each other. Hence, the static friction coefficient between materials is larger than the dynamic friction coefficient.

According to Rabinowicz [13], the short contact time between the sliders and the track can decrease the number of junctions formed between the surfaces and therefore reduce the coefficient of friction between them. This effect, however can only be responsible for decreasing the friction coefficient between the sliders and the track from its static value of approximately 1.4 to its dynamic value of 1 or 0.9. The further reduction in the effective value of the coefficient of friction encountered while operating the motor, suggests that there is an effective drop in the normal force between the sliders and the track. The normal force between the sliders and the track could decrease as a result of the vibrations along the vertical direction that the slider is subjected to. If a slider finds itself in free flight during certain intervals of the operation of the motor the average normal force between the slider and the track will decrease. The normal force between the sliders and the track will also decrease if there is a layer of air that is supporting part of the weight of the slider and not allowing it to make contact with the track. This possibility is addressed at greater length later in the discussion.

Power and Efficiency

Electric Power : The electrical power delivered to the motor was calculated by measuring simultaneously the voltage and current levels of one of the driving electrical signals leaving the amplifiers. Figure 31 shows the voltage and current levels as measured during one cycle of operation, while Figure 32 shows the relationship between the current and the power delivered by the amplifier during that same interval of time.

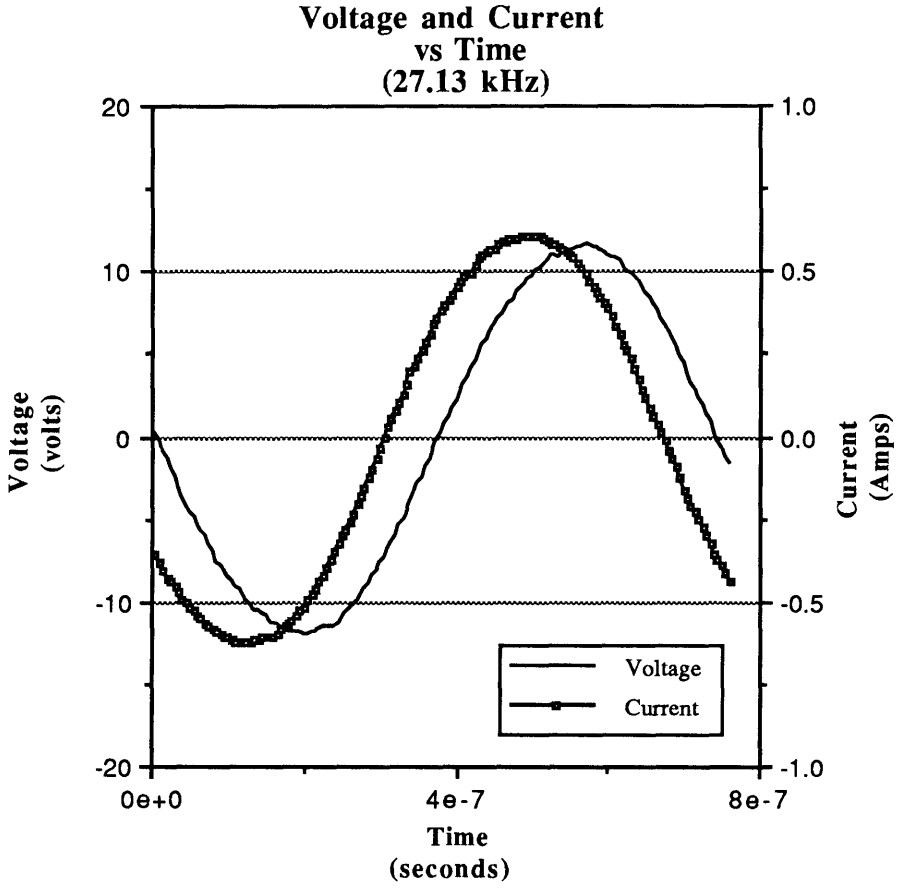

Figure 31- Voltage and Current Levels of Driving Amplifier Signal

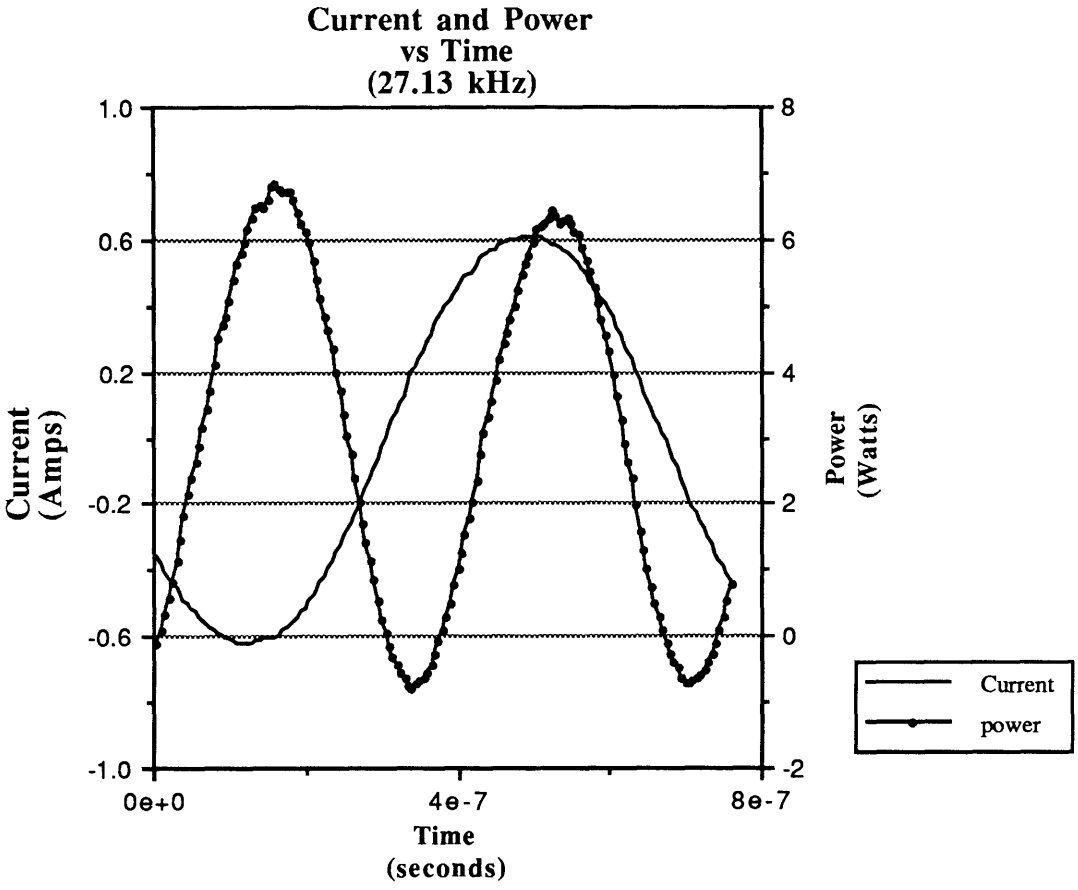

Figure 32- Current and Power Levels for Driving Amplifier Signal

The power curve in Figure 32 is shown to go negative during certain intervals of the operating cycle. This demonstrates that at resonance, the piezo ceramics in the track are converting some of the energy stored in the deflection of the track back to electrical power and doing work on the amplifier.

By numerically integrating the power data of Figure 32 as follows:

$$\text{Power} = \frac{\sum_{i=0}^{i=T} P_i \Delta t_i}{\sum_{i=0}^{i=T} \Delta t_i} \qquad (43)$$

the electric power delivered by the amplifier was estimated at 2.97 watts per signal or a total of 11.89 watts.

The electric power delivered to the track appeared to remain constant at a given frequency, regardless of the amount of mechanical work extracted from it. Any fluctuations in electrical power due to changes in mechanical loading were beyond the precision of the measuring devices used.

The electric power delivered to the track, did vary however, depending on whether the track was fixed to the aluminum base plate (via the layers of foam and rubber) or whether the track was suspended in mid air (with the foam tape attached to it). Figures 33 and 34 show the voltage, current and power curves of the signals going into the motor while the track is suspended.

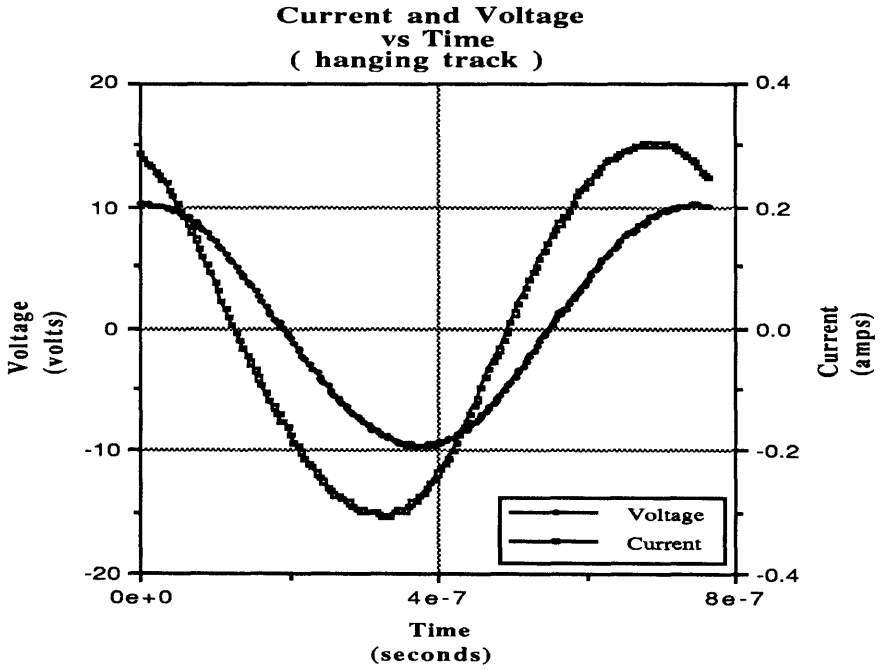

Figure 33- Voltage and Current of Driving Signal From Amplifier vs Time. The Track is Being Suspended Above the Base Plate.

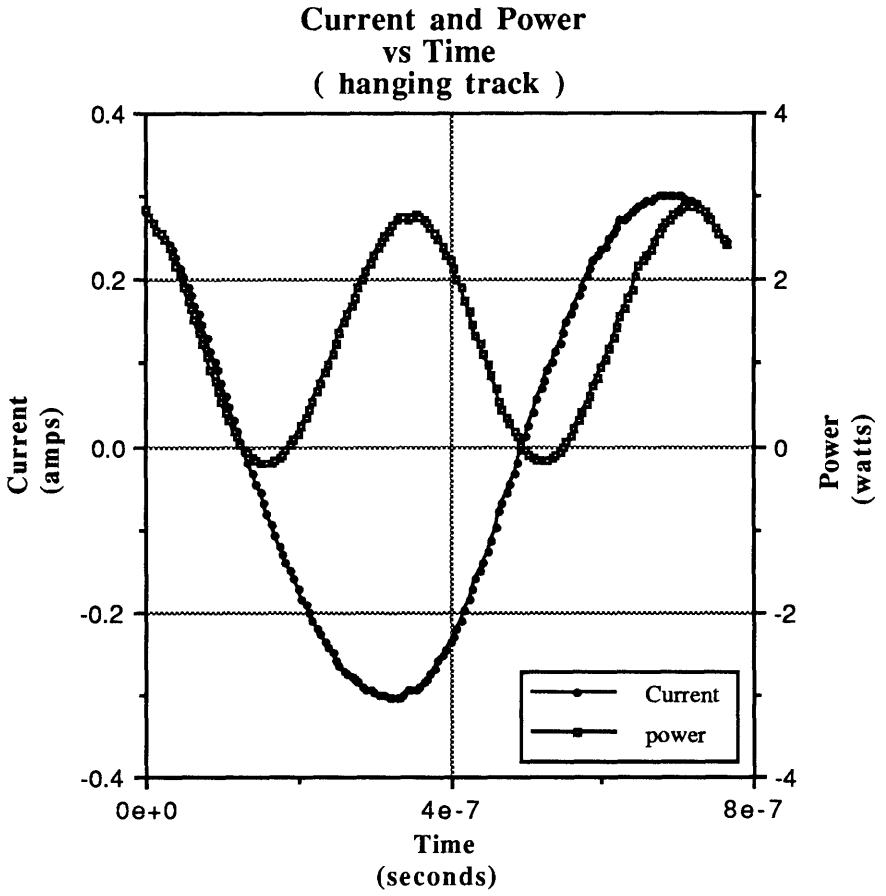

Figure 34- Current and Power versus Time. The Track is Suspended above the Base Plate

The electrical power delivered to the motor when the track is suspended in mid air is approximately 1.38 watts per signal. The total electrical power delivered to the motor is 5.536 watts. This figure is approximately 2.14 times smaller than the power delivered to the track when the motor is mounted onto is base plate for regular operation. This difference can be attributed theoretically to both mechanical and thermal energy dissipation into the rubber and aluminum base plates. In practice, however, no vibrations were detected on the surface of the aluminum base plate, which suggests that the dissipation of energy onto the base was mainly thermal in nature. (See Thermal Dissipation)

Mechanical Power : An estimate of the mechanical power output was obtained by allowing the sliders to travel along an incline of a specified angle at a constant velocity. The product of the measured velocity by the side force needed to maintain static equilibrium is equal to the mechanical power extracted by the slider from the motor.

Figure 35 shows the side force exerted by the motor as a function of the velocity of the sliders. The data points located along the y axis of the plot correspond to force measurements taken when the slider was at rest, such as the force measurements taken with the calibrated spring. The spread of these data points along the y axis corresponds to sliders of different weight. The data points located along the x-axis correspond to speed measurements taken while the sliders were moving at their top speed. The force exerted on the sliders is zero since the sliders are not doing work against anything. The data points in between the axis correspond to sliders which are extracting mechanical work from the track and therefore have non-zero velocity as well as non-zero force.

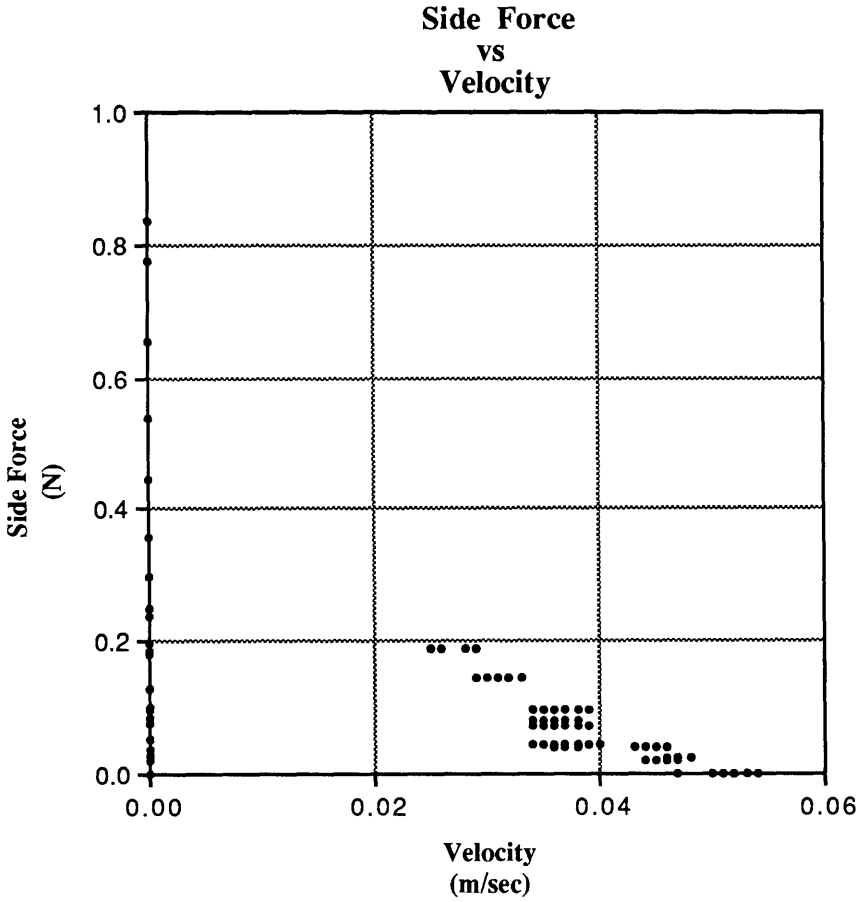

Figure 35- Side Force Exerted by Motor as a Function of Slider Velocity.

The data points shown in Figure 35 suggest a frictional model such as the one illustrated in Figure 36. Points along the horizontal axis correspond to sliders who have the greatest velocity relative to the inertial frame of the base of the motor, but which are at rest relative to the points of the surface of the track with which they are in contact. The slip velocity for these points is zero, hence, there is no force exerted on the sliders by the track. When the velocity of the slider stops matching that of the top surface of the track, a slip velocity between the sliders and the track appears and so does a frictional force. The greatest slip velocity is encountered when the velocity of the sliders is zero relative to the inertial frame of the base. As shown in Figure 35, the force on the slider is related to the speed of the slider, and hence to the slip speed between the slider and the track. The

frictional model in Figure 36 is one which allows for a dependency between slip velocity and coefficient of friction.

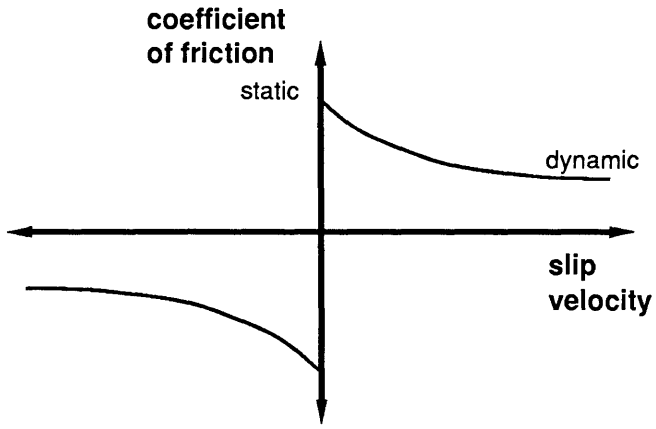

Figure 36- Suggested Frictional Model based on Results

Figure 37 shows both force data and power estimates as functions of velocity. The curves shown in the figure are both fourth order polynomial approximations to the data available. The largest amount of mechanical power extracted from the motor was measured at 6 milliwatts. This amount of power was extracted by placing one slider on the surface of the track an allowing it to go up the incline. More power could have been extracted from the motor if the mass of the slider had been increased. This was not done in order not to scratch the surface of the track.

The mechanical power extracted from the track could also be increased by placing more sliders on the track. This was not done in general however, since it was not possible to place enough sliders on the track and have them move freely without interfering with each other. This was done successfully, however, with two sliders of equal mass. The power extracted during this run was approximately 12 milliwatts.

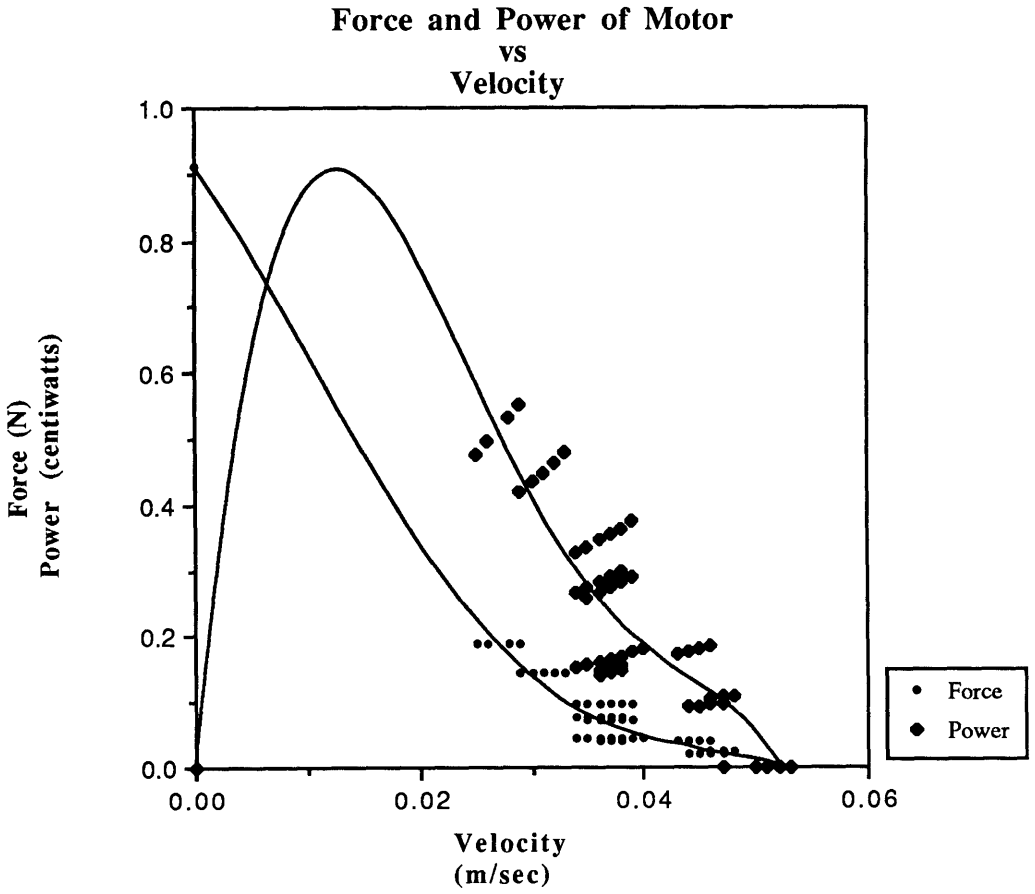

Figure 37- Side Force And Power Curves as Functions of Slider Velocity.

Thermal Dissipation : The rate at which the motor is converting electrical energy into heat was estimated by measuring the temperature increase of the track while attached to the hard rubber base via double sided sticky foam, and while the track was kept suspended in the air (with the foam tape attached to it). Figure 38 shows the measured surface temperature of the track as a function of time. The curve on the top, represents the temperature increase of the track fixed to the base. The lower curve shows the temperature rise of the track suspended in mid-air. During the first 400 seconds of operation the increase in temperature of the tracks is close to linear, and can be approximated by straight lines as the ones shown in Figure 38. After 400 seconds, the rate at which heat is dissipated by the surface of the tracks onto its surroundings approximates the rate at which

heat is being pumped into the track, and hence the temperature curves level off. The slope of the straight lines approximating the tracks' initial increase in temperature is a good indicator of the power used to raise the temperature of the track.

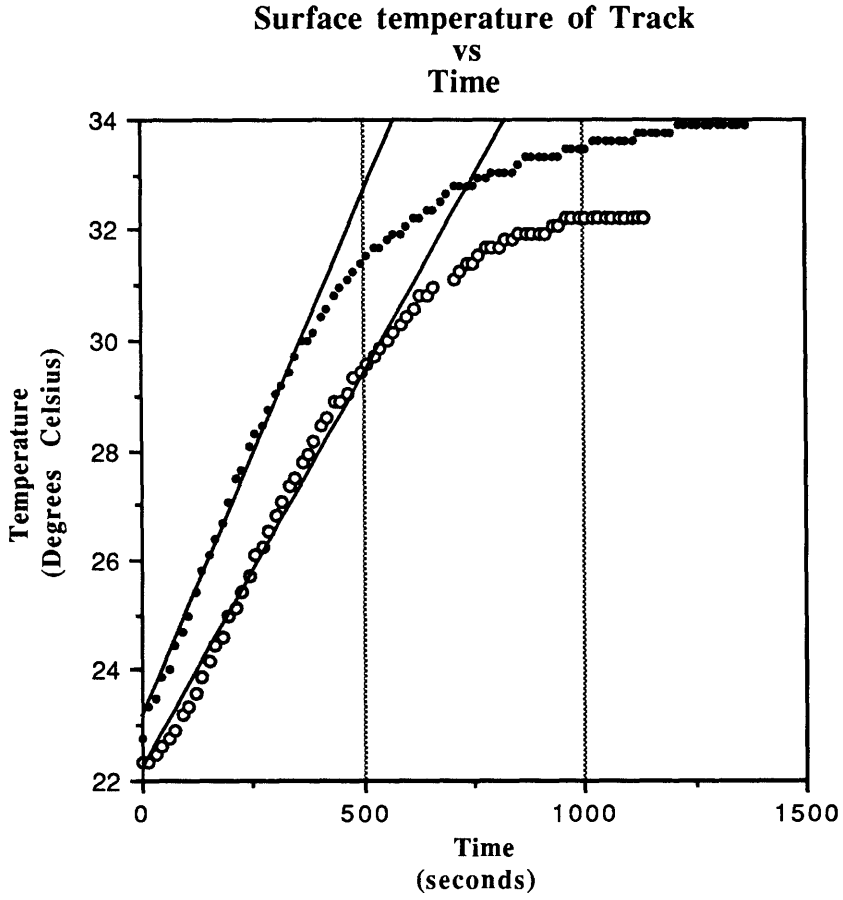

Figure 38- Measured Surface Temperature of the Track as a Function of Time

The power used to increase the temperature of the track was calculated using the following relationship :

$$P_{heat} = \frac{m\Delta TC_f}{t} \qquad (44)$$

where: m = mass of the composite track = 0.0673 Kg

C_f = Specific Heat of Aluminum = 895.37 J/Kg K

$\Delta T/t$ = Slope of the straight line in Figure 34

= 0.01896 K/sec (for the rubber-mounted track)

= 0.01423 K/sec (for the suspended track)

The track mounted on the rubber base absorbs 1.14 watts of heat, while the track suspended in mid air (with the foam tape attached to it), absorbs 0.86 watts of heat. These estimates equate the specific heat of the piezo ceramics to that of Aluminum and neglect to take into account the mass of the rubber or the foam in thermal contact with the track. These assumptions could be wrong by a factor of 3 or 4. When the track was suspended without the foam tape attached to it, the track still absorbed 1.14 watts of heat.

Figure 38 indicates that the when the aluminum track is suspended, its temperature does not increase as rapidly as when it is attached to its base plate. Furthermore, Figure 38 also indicates that the equilibrium temperature of the suspended track is lower than that of the mounted track.

When the track is mounted onto the base plate, the piezo ceramics cause both the aluminum track and the foam tape plus rubber substrate to strain. The heat produced by these materials is proportional to the amount of strain they undergo. The amount of strain that they undergo is inversely related to their modulus of elasticity. Rubber's modulus of elasticity is anywhere between 700 to 70000 times smaller than that of Aluminum while rubber's thermal conductivity is about 1000 times smaller than that of Aluminum*. Any heat produced by the piezos, aluminum and foam tape will probably manifest itself in the temperature increase of the track. Any heat produced by the rubber substrate will probably dissipate through the Aluminum base plate which can acts as a good heat reservoir.

---

* Rubber has a thermal Conductivity Value of 0.15 watts/m K, while Aluminum has a value of 164 watts/m K.

The difference between the amount of power used to heat up the track when it is suspended or mounted on the base is small compared to the difference between the electrical power required to drive the motor when it is suspended in mid air or mounted onto the base plate. This suggests that the amount of power dissipated as heat by the track, piezos, and foam tape is in the vicinity of 1 watt while the extra power delivered by the amplifier when the track is mounted onto the base plate is going into the base plate. This implies that when the track is in operation approximately 6.4 watts of power get dissipated into the base plate.

Acoustic Dissipation : While in operation, the travelling wave motor radiates energy in the form of sound. Most of the sound radiated, probably occurs in the ultrasonic range at the operating frequency of 27230 Hz. This hypothesis, however, was not verifiable experimentally, since equipment capable of measuring sound pressure disturbances at this frequency range was not available.

The traveling wave motor emitted sound waves at the audible frequencies of 3037 Hz and 13646.8 Hz. These signals were detectable by available sound level indicators, and they were also found present, using a spectrum analyzer, in the signal read from the strain gauge mounted on the track. These two frequencies correspond to the first and ninth subharmonic of the motor's operating frequency of 27230 Hz.

When disconnected from the track, the driving circuitry produced a relatively clean sinusoidal signal at 27230 Hz. The electrical signal contained strong higher harmonics at 54 kHz and 81 kHz, but these signals were attenuated relative to the main frequency signal of 27 kHz, by -45 dB and -30 dB respectively . The electrical signal also contained low frequency noise and subharmonics of the resonant frequency, but these were attenuated by more than -70 dB relative to the operating frequency.

As shown above, the electric signal driving the motor appears to be clean, yet the track radiates acoustic energy at subharmonics which are not being driven by the electric input signal. This suggests that the motor has a detectable non-linear behavior. On the other hand, if the audible acoustic energy is the result of an electric signal 70 dB lower than the main operating frequency, then the power dissipated as sound at the operating frequency should be approximately 70 dB greater than what was measured at the audible frequencies.

The sound pressure level emitted by the track in the frequency range between 20 Hz to 20 kHz was measured (using a flat weighting filter) to be 102 dB. This sound pressure level indicates that the motor is dissipating approximately 3.7×10^{-7} watts of audible sound. (See Appendix 6 for acoustic power estimation procedure). The amount of energy being dissipated at frequencies above 20 kHz is unknown. However, if we assume that it is about 70 dB greater than what is emitted in the audible range, we obtain an estimate of 1.17×10^{-3} watts.

Overall Efficiency : The overall efficiency of the motor was defined as the ratio between the electrical power supplied by the amplifiers and the mechanical power extracted from the motor. The best measured efficiency achieved by the motor was 0.1 %. based on previous discussion it can be said that this estimate is a conservative one. Higher efficiencies are attainable.

The energy balance for the motor is summarized in Table 1.

Table 1- Energy Balance Summary for Motor

		Mounted on Base Plate	Suspended in Air
Input Power	**Electric**	11.89 W	5.53 W
Output Power	**Mechanical**	12 mW	NA
	Thermal	1.14 W (into track) 6.4 W (into base)	0.86 W (w/ foam tape) 1.14 W (w/o foam tape)
	Acoustic < 20kHz	3.7×10^{-7} W	3.7×10^{-7} W
	Acoustic >20 kHz	1.17×10^{-3} W	(estimated value)
	Lost Power	3 W	NA
Overall Efficiency = 0.1 %			

The most accurate figures above, are those of the electric input power. The thermal power consumption figures provided above represent conservative values, since they are values which have been directly or indirectly measured. The amount of power unaccounted for, is therefore probably much less than 3 watts, which makes sense, since energy conservation demands that the lost power be equal to zero.

Torsional Coupling Present in Motor

While evaluating the performance of the motor, it became apparent that objects placed on top of the track were subjected to a force which made them slide back and forth across the width of the track. It was also observed that this motion was not arbitrary since the changes in direction of the objects placed on the surface occurred at approximately equal intervals, and always at the same location along the track.

The scratch patterns left by the various sliders on the surface of the track, revealed a sinusoidal motion with an average wavelength of 0.0835 m, with a standard deviation of

.0135 m. The whole wave pattern remain fixed relative to the track, suggesting that together with the travelling wave, the piezo ceramics were also driving a torsional standing wave.

Equation (9) represents the equation of motion describing the twisting behavior of a straight beam.

$$GJ\beta'' - \rho J\ddot{\beta} = 0 \tag{9}$$

By assuming a solution of the form :

$$\beta_{(x,t)} = \beta_o e^{i(kx+\omega t)}$$

we obtain the following dispersion relation:

$$GJk^2 = \rho J\omega^2$$

which can be rewritten as equation (45) in terms of the wavelength and of the operating frequency in Hz :

$$\lambda_t = \frac{1}{f}\sqrt{\frac{GJ}{\rho J}} \tag{45}$$

Given that the density for the composite beam has been estimated at 3562 Kg/m3 and that the shear modulus of the track is approximately that of aluminum, ie- G = 2.688 x 10^{10} Pa, equation (45) predicts that the wavelength of the torsional waves along the straight sections of the track, is approximately $\lambda_t = 0.1062$ m. This value is approximately 27 % larger than the average wavelength, yet within the range of measured values of λ_t.

Comparing the wavelength of the measured sinusoidal movements on the track, to the wavelength of the predicted torsional mode of vibration, suggests that these two

phenomena are the same. The discrepancy between theory and practice could be the result of a discrepancy concerning the value of the track's shear modulus.

It was further noticed that the separation between the nodes of the torsional standing wave varied greatly and that the node pattern became diffuse along the curved sections of the track. Furthermore, the node pattern was slightly shifted relative to the symmetry axis of the track. All this seems to indicate that the standing wave pattern was very sensitive to construction irregularities in the track.

During design, the dispersion curves for the racetrack predicted the presence of a torsional mode at the operating frequency. The magnitude of such a presence or how it would interact with the transverse mode of vibration was unknown and a detailed analysis was not attempted. The chosen value for the radius of the track was meant to minimize the effect of the torsional waves on the transverse waves. From an operational point of view, this was achieved since the effect of the torsional waves is minimal and the track is capable of performing satisfactorily.

One possible method of eliminating the undesired torsional waves is to increase the radius of the circular portions of the track. Another method, which was suggested in the theoretical section of this paper, is to change the cross section of the track in the circular portions of the motor such that the thickness increases towards the outer edges, or the section mass center is shifted slightly towards the inner edges. Neither of these options was tested since we did not want to physically damage the surface of the track, and since we were skeptical about the possible benefits of performing these alterations on a track whose torsional behavior was somewhat erratic.

Other Observed Phenomena

Dynamics of Short Sliders : As described in Section 2, objects that are longer than the operating wavelength of the motor will essentially only be in contact with the crests of the waves. The velocity of the surface, at the crest of the waves, is opposite in direction than that of the velocity of the travelling waves. The sliders resting on the surface of the track will try to match the speed of the crests, and therefore move in the direction of the crest velocity.

Surprisingly, while testing the travelling wave motor, sliders of different lengths were used. Their measured velocities at a given frequency were the same regardless of their length. Among the sliders tested, one of them was a half a wavelength in length and the other one was a quarter wavelength in length. Despite their size, these sliders moved in the same direction as the longer ones, with the same speed. In theory, however, it would seem possible for these smaller sliders to fall into the trough of a wave and gain contact with those surfaces of the track whose velocity is in the same direction as that of the travelling wave. Such an occurrence would cause the smaller sliders to move in the opposite direction than those sliders whose length is greater than a wavelength.

This possibility is unique to linear travelling wave motors since, a circular motor has a rotor which is resting at all times on the crests of all the waves of the stator. A linear travelling wave motor, however, has a slider which rests on only some of the crests of the track at any given time. In the case of a slider that is smaller than the wavelength of the travelling waves, it is possible for the slider not to be in contact with any crests at all.

The fact that the smaller sliders behaved identically to the larger ones is due to the particular operating conditions of the motor and can be explained as follows : Figure 39 shows the upper surface of a portion of the track and the velocity profile of the surface

through a whole cycle. At the motor's operating conditions, the travelling wave is moving at a velocity of 693.4 m/sec, while a point on the crest of a wave is moving in the opposite direction at approximately 5 cm/sec. For a point mass to move in the same direction as that of the travelling wave, it must make contact with the portions of the track's surface which are below the centerline. An object smaller than the wavelength of the travelling waves does not touch the surfaces below the centerline because it does not have time to reach them.

Figure 39 depicts a particle leaving the crest of a wave with zero vertical velocity and free falling until it collides with the next wave. Because of the velocity at which the waves are travelling, the particle has less than 36.7 μ seconds of free fall time. During this time, it can descend a distance **h** equal to 6.5 nanometers which is approximately 1/200th of the amplitude of the traveling waves. If the particle does not bounce upwards significantly after colliding with the incoming wave, it will simply be lifted up and pushed sideways at the crest. This particle will therefore always be in contact with points on the surface very close to the crest of the waves, and its velocity will always be in the direction opposite to that of the travelling waves.

Figure 39 also depicts a mass particle falling from a certain height **h2** and following a trajectory (in the wave frame of reference) which allows it to go fast enough to reach the bottom of the wave trough. This distance **h2** corresponds to a height of 1 mm, which is approximately half the thickness of the track.. Therefore, as long as the sliders on the track do not vibrate up and down in a visible manner, there is no chance of a particle reaching the trough of a travelling wave.

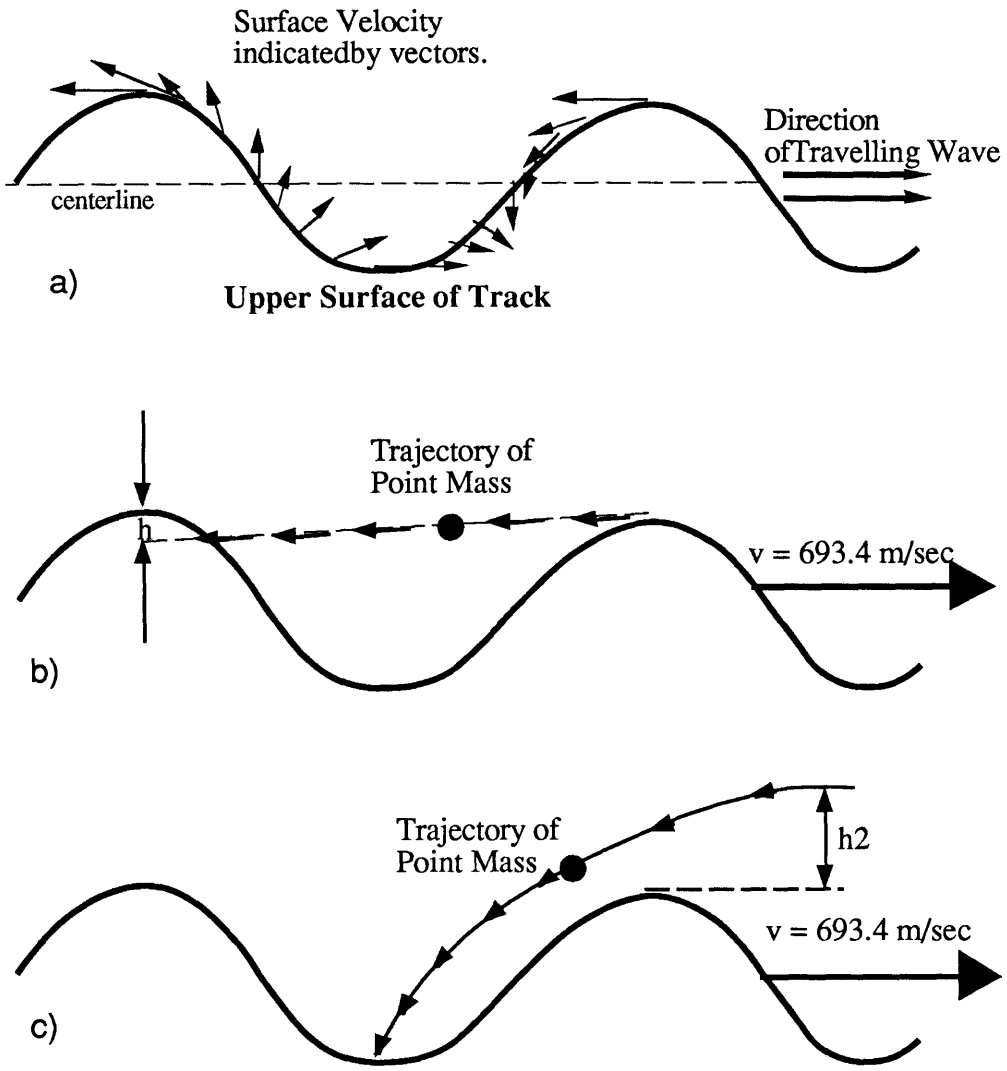

Figure 39- a.) Surface velocities of track over a wavelength. b.) Probable trajectory for mass particle resting on track. c.) Improbable trajectory for mass particle on track.

The previous explanation, suggests that if the operating frequency of the motor was smaller or if a particle was dropped onto the track from a height greater than one mm, such a particle would have a chance traveling along the same direction of the waves. This hypothesis was verified on a couple occasions when a small piece of plastic was dropped onto the track and started travelling backwards. This event, however, was not verifiable in a repeatable manner.

Aerodynamic Effects : While evaluating the performance of the motor, several observations could not be explained using the models developed to describe the functioning of a travelling wave motor: Flat surfaced sliders, with large surface areas had been noted to hover at a given position along the track while "slotted" sliders of equal weight and dimensions would move along a given direction as expected; furthermore, measured force data seemed to correlate better when normalized by pressure. This suggests that the side force supplied by the track is somehow related to surface area.

The observations suggested that a layer of air trapped between the sliders and the track was preventing these surfaces form establishing good contact. As mentioned before, the track's local vibrational motion could be forcing air to circulate about it as shown in Figure 40.

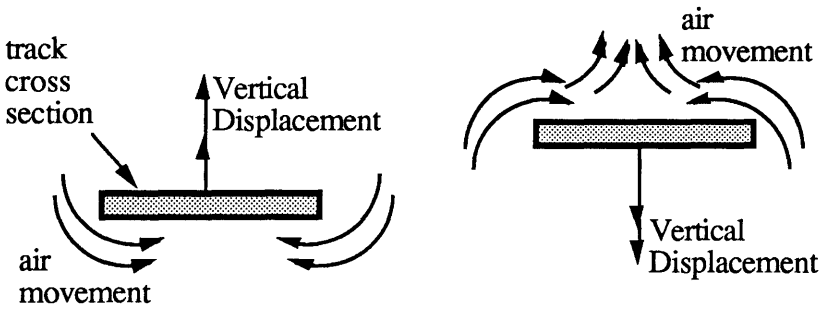

Figure 40- Air Circulation About Track Due to its Vibrational Motion

By placing a flat slider on the surface of the track, air is forced underneath it thereby creating a cushion which separates it from the track. Hence the flat sliders, hover at a given position and do not make good contact with the crest of the waves. This prevents them from feeling the side force exerted by the track. On the other hand, the slotted sliders allow air to flow underneath them without preventing the slider from remaining in contact with the track. Hence the slotted sliders feel the side force exerted by the track in a consistent manner.

The air circulation effect was crudely verified by placing the motor in a vacuum chamber and reducing the pressure within the chamber to 0.0045 torrs. A flat slider was placed on the track and the velocity of the slider was measured as a function of the operating frequency of the motor. Figure 41 compares the data obtained in the vacuum chamber to the data obtained under regular laboratory conditions. The slider used under regular laboratory conditions was a slotted slider.

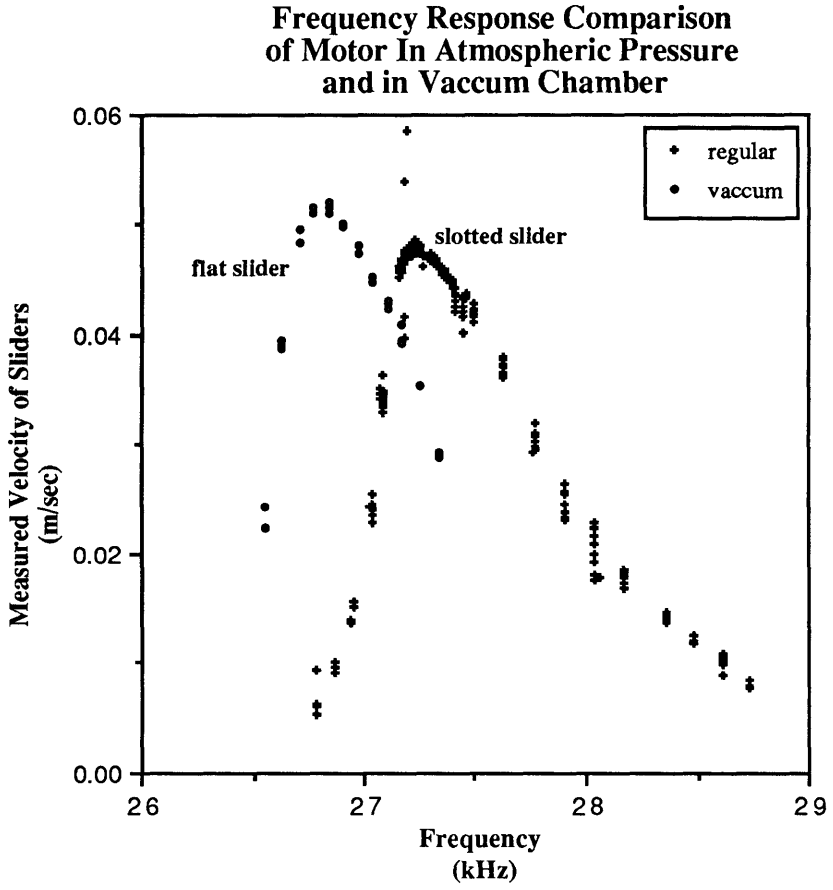

Figure 41 - Comparison of the Frequency Response Curves in Regular Laboratory Conditions and in Vacuum

As shown in Figure 41, the performance of the flat slider in vacuum increased to a level comparable to that of the slotted slider in air. No hovering behavior was displayed by

the flat slider. This evidence suggests that an air cushion between the slider and the track while operating the motor in air was affecting the performance of the motor.

Figure 41 also shows the resonant frequency of the motor shifting from 27230 Hz to to a lower value of approximately 26700 Hz. This decrease in the resonant frequency suggest that the effective stiffness of the track in the vacuum chamber is lower than that of the track at standard atmospheric pressure or that the track is experiencing air loading effects while operating in a vacuum. The air loading hypothesis would support an increase of the resonant frequency when operating the track in vacuum. The data, however displayed the opposite trend.

A decrease in the effective stiffness of the track can be attributed to a change in behavior of the foam layer supporting the track. If the structure of the underlying foam is porous, then the vacuum chamber would extract the air from the foam structure leaving behind a less rigid mesh of material. Thus, the overall stiffness of the track decreases causing the resonant frequency of the motor to shift as well.

V- Conclusions & Suggestions for Further Research

The primary and secondary goals of this project were accomplished. A working prototype of a linear travelling wave motor was successfully constructed and tested within the time span of 8 months. Careful analysis of the results obtained suggest the following:

• The models used in designing the track were able to accurately predict the resonant frequency of the travelling wave motor. These models however were not able to properly characterize the torsional behavior of the track.

• Torsional coupling in the track was detectable, yet insufficient to render the motor ineffective. The torsional behavior of the track was found to be very sensitive to variations in the construction of the track.

• The overall measured efficiency achieved by the motor was 0.1 %. Most of the energy used by the motor was dissipated as heat by the rubber base it was mounted on. A better track suspension design is required for future motors.

• At high operating frequencies objects will be displaced by travelling wave motors at essentially the same speed regardless of their length.

• The performance of the motor was hindered by the presence of air at the interface between the sliders and the track. In practice this meant that sliders operated better if the surface in contact with the track was small or if the motor was placed in a vacuum chamber.

In order to improve the performance of travelling wave motors, further research is needed in the following areas :

• The dynamic behavior of small objects placed on travelling wave motors requires better understanding. It would be interesting to verify whether the direction of travel of a particle can changed by varying the operating frequency of the motor and not the direction of the travelling waves.

• The aerodynamic effects encountered during the experiments need to be further understood. It is possible that for certain operating conditions, these effects may hinder less the performance of the motor. It is also evident that better sliders need to be designed.

• A feedback control system should be incorporated into the motor's configuration in order to evaluate its potential use as a positioning actuator. This requires a better understanding of the transient behavior of the motor.

• A motor with variable cross sectional properties should be constructed in order to verify the predicted decoupling of the torsion bending modes of vibration.

VI- Appendices

APPENDIX 1-A

Electric Circuit Design

The driving circuitry is composed of a *quadrature generator* which is responsible for generating four square waves shifted 90 degrees in phase relative to each other and a *filtering circuit* which filters out the higher frequency components of the square waves and leaves four, similarly phased, sine waves. These signals are then amplified and sent to their corresponding piezo ceramics.

Quadrature Generator and Filtering Circuit : These circuits were implemented digitally using TTL logic components and assembled on a protoboard. Appendices 1-B and 1-C contain the circuit diagrams for both of these circuits.

Circuit Description: The quadrature generator uses the TTL output of a signal generator as the main clock for the circuit. Two cascaded 4-bit counters (LS163's), divide the frequency of the clock pulse by 19 and this signal is then divided by 2 as it is converted into a square wave by a J-K flip-flop (LS76). This square wave is then split into two signals, one of which is inverted and the other which is buffered. These two signals are used to clock two more J-K flip-flops operating in toggle mode, thereby obtaining 4 square wave signals, 1/76th of the original clock frequency and shifted by 90 degrees.

The dc component of these four signals is eliminated by an analog high pass filter. The resulting ac signals are then fed to the digital filters which have a 75:1 clock to corner frequency ratio. These filters require a +/-8 V voltage supply which is provided by two regulators connected to the +15V power supply of the protoboard.

Amplification and Connections to Piezoceramics : The output signals of the digital filters are then buffered by "follower circuits" implemented using operational amplifiers (3140's). These signals are then used to drive two dual channel Crown Amplifiers (DC-150 and DC-300).

The signals from the amplifiers are finally used to drive the piezo ceramics on the bottom side of the racetrack. The aluminum track serves as common ground for all four signals. The track however, is electrically floating, since it is not connected directly to ground. This is possible due to the complementary nature of the driving signals.

Besides serving as common electrical ground, the aluminum track behaves as a heat sink for the piezo ceramics, to prevent them from overheating. Depolarization of the piezo ceramics is avoided by using high frequencies. The G1195 ceramic looses it polarization at about 30 Volts when driven at DC or at low frequencies. By operating in the 30 kHz range, the voltage levels can be doubled or tripled without causing depolarization.

The amplifiers are responsible for driving a capacitive load of approximately 200 pF at 30000 Hz. This implies that each signal will require current levels in the order of 0.7 amperes and that the amplifiers will have to dissipate at their output stage approximately 30 watts per signal (@ 20 volts p-p). Appendix 1-D elaborates on the power consumption estimates of the circuitry.

APPENDIX 1-B

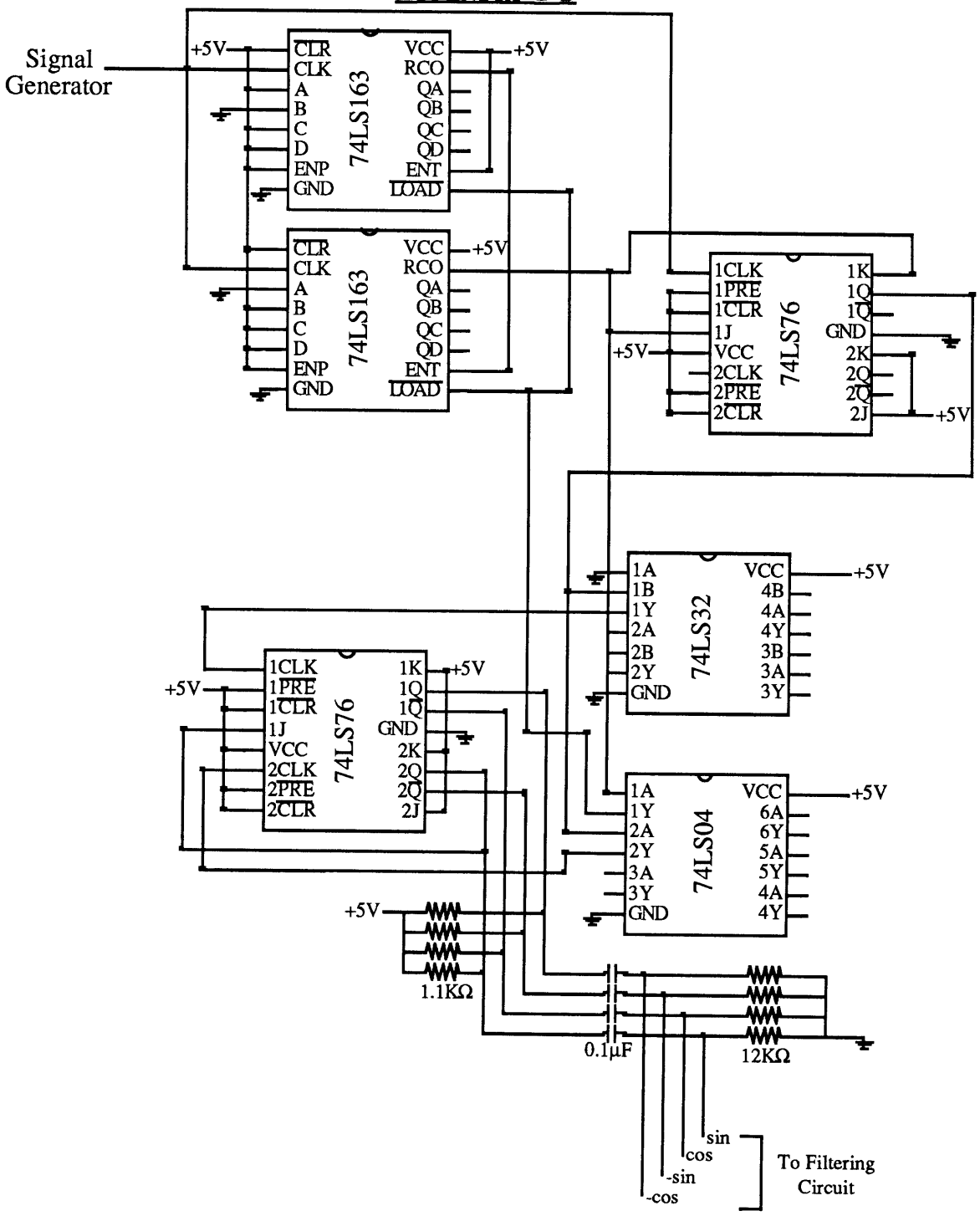

Square Wave Quadrature Generator

APPENDIX 1-C

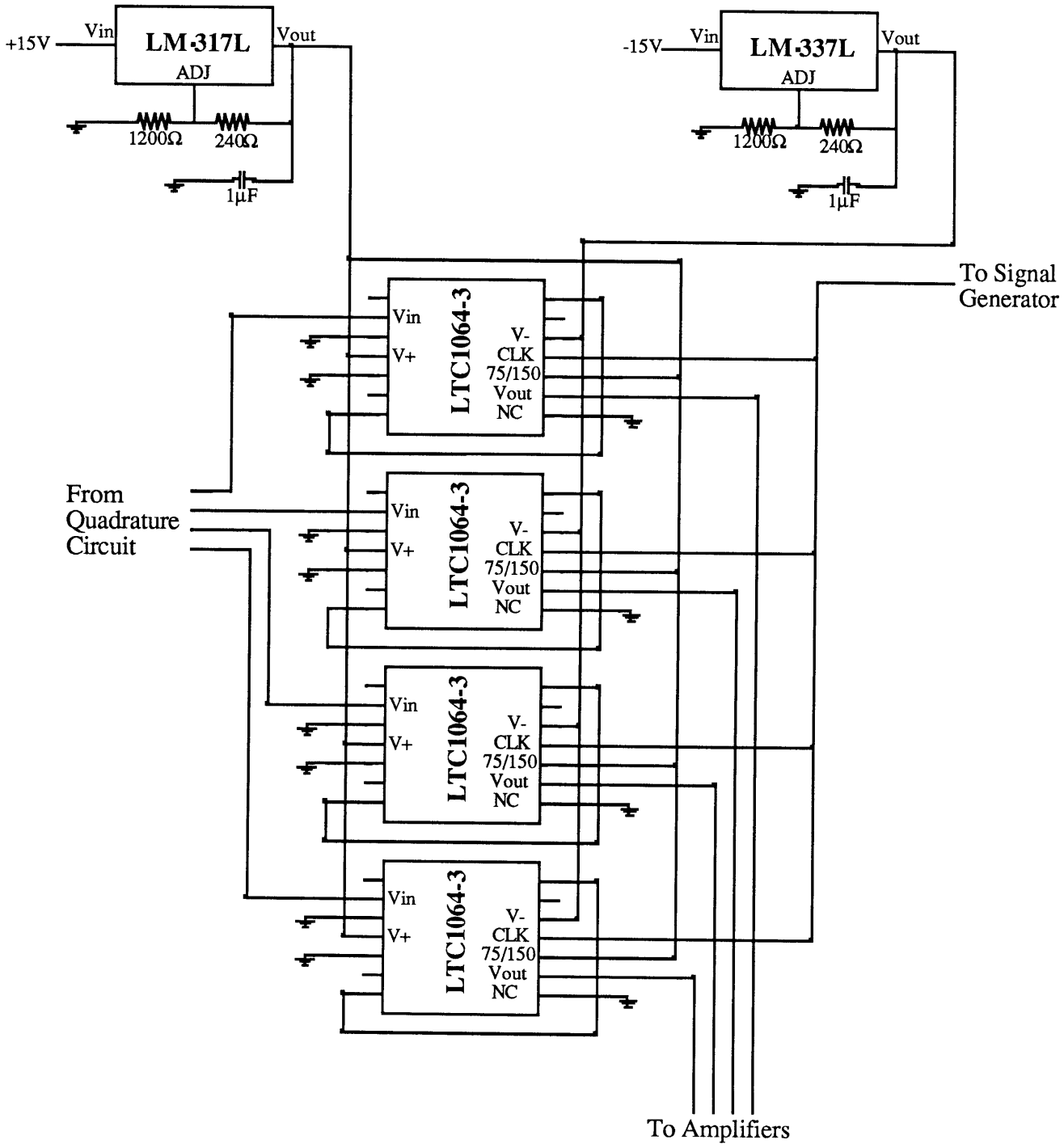

Digital Filter with 76:1 Clock to Corner Frequency Ratio

APPENDIX 1-D

Estimate of Total Capacitance and Power Consumption of Motor

Given the dimensions of the track, the total surface area of piezo electric ceramics covering it, can be approximated to 14.5 in^2. From Appendix 5, the value of K^t is known. The overall capacitance of the piezo layer can be estimated using :

$$C = \frac{\varepsilon_r A}{4.448T} = \frac{k^t A}{4.448T}$$

where the area A is given in units of inches squared, and C is given in Farads. There are 116 piezo ceramics which effectively behave as four piezos, each with an equivalent area of 3.678 in2. The equivalent capacitance of each of these four piezos, as given by the above formula is $C = 200.69 \times 10^{-9} F$.

Now in order to estimate the current requirements per signal, the motor was modelled as a simple capacitive circuit, where :

$$V_{(t)} = V_o \sin \omega t$$

$$i = C\frac{dV_{(t)}}{dt} = C\omega V_o \sin \omega t$$

This implies that the maximum current drawn by each signal is given by:

$$\max(i) = V_o \omega C$$

Using this relation and the following values :

$$V_o = 20V(p-p)$$

$$\omega = 2\pi(27434Hz)$$

the maximum current drawn by each signal is estimated at 0.6919 amps. This further implies that each amplifier must be capable of delivering approximately 28 watts of power

APPENDIX 2

DERIVATION OF PDE'S FOR CIRCULAR BEAM

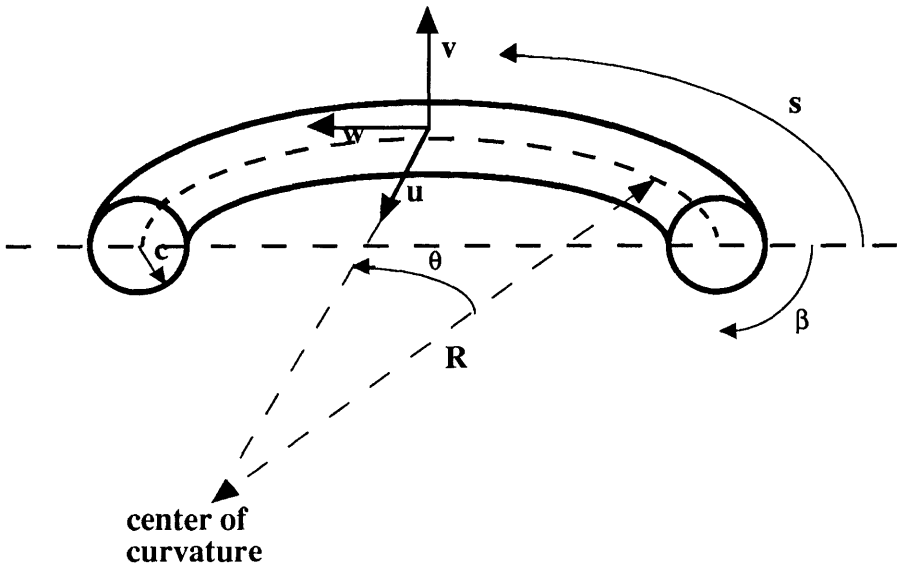

As copied from Love [1], force and moment equilibrium considerations, lead to the following six equations:

Force Balance Equations:

$$\frac{\delta N}{\delta \theta} + T = mR\frac{\delta^2 u}{\delta t^2} \tag{46}$$

$$\frac{\delta N'}{\delta \theta} = mR\frac{\delta^2 v}{\delta t^2} \tag{47}$$

$$\frac{\delta T}{\delta \theta} - N = mR\frac{\delta^2 w}{\delta t^2} \tag{48}$$

Moment Balance Equations:

$$\frac{\delta G}{\delta\theta} + H - N'R = -\frac{1}{4}c^2 m\frac{\delta^3 v}{\delta t^2 \delta\theta} \tag{49}$$

$$\frac{\delta G'}{\delta\theta} + NR = \frac{1}{4}c^2 m\frac{\delta^2}{\delta t^2}\left(\frac{\delta u}{\delta\theta} + w\right) \tag{50}$$

$$\frac{\delta H}{\delta\theta} - G = \frac{1}{2}c^2 mR\left(\frac{\delta^2\beta}{\delta t^2}\right) \tag{51}$$

where using Love's notation:

m = mass per unit length of beam
c = radius of the cross section of the beam
u = displacement in the radial direction
v = displacement in the transverse direction
w = axial compression or extension
β = twist about about the centerline
θ = angle distended by circular beam
N = shearing force on cross sectional face
T = tension
G = flexural couple defined in Love [1]

Now given the following constituent relations:

$$G = \frac{1}{4}E\pi\frac{c^4}{R^2}\left(R\beta - \frac{\delta^2 v}{\delta\theta^2}\right) \tag{52}$$

$$G' = \frac{1}{4}E\pi\frac{c^4}{R^2}\left(\frac{\delta^2 u}{\delta\theta^2} + \frac{\delta w}{\delta\theta}\right) \tag{53}$$

$$H = \frac{1}{2}\mu\pi\frac{c^4}{R^2}\left(\frac{\delta v}{\delta\theta} + R\frac{\delta\beta}{\delta\theta}\right) \tag{54}$$

as well as the expressions for the bending and polar moments of inertia as defined for a beam of circular cross section:

$$I = \frac{1}{4}\pi c^4$$

$$J = \frac{1}{2}\pi c^4$$

the derivation of the equations for out of plane motion, can be completed: we set the rotary inertia of (49) equal to zero, solve for N' and differentiate by θ. This result is then plugged into (47) and used together with equations (52), (53), (54) and the coordinate transformation :

$$\frac{\delta()}{\delta\theta} = R\frac{\delta()}{\delta s}$$

to obtain the coupled equations:

$$\frac{\delta^2}{\delta s^2}\left(EI\frac{\delta^2 v}{\delta t^2}\right) + \rho A\frac{\delta^2 v}{\delta t^2} = \frac{\delta^2}{\delta s^2}\left(\frac{EI\beta}{R}\right) + \frac{\delta}{\delta s}\left(\frac{GJ}{R^2}\frac{\delta v}{\delta s}\right) + \frac{\delta}{\delta s}\left(\frac{GJ}{R}\frac{\delta\beta}{\delta s}\right) \tag{55}$$

$$\frac{\delta}{\delta s}\left(GJ\frac{\delta\beta}{\delta s}\right) - \rho J\frac{\delta^2\beta}{\delta t^2} = -\frac{EI}{R}\frac{\delta^2 v}{\delta s^2} - \frac{\delta}{\delta s}\left(\frac{GJ}{R}\frac{\delta v}{\delta s}\right) + \frac{EI\beta}{R^2} \tag{56}$$

If we assume that the material properties of the beam remain constant throughout the length of the beam, then these equations become:

$$EIv'''' + \rho A\ddot{v} = \frac{1}{R}(EI + GJ)\beta'' + \frac{1}{R^2}GJv'' \tag{13}$$

$$GJ\beta'' - \rho J\ddot{\beta} = -\frac{1}{R}(EI + GJ)v'' + \frac{EI\beta}{R^2} \tag{14}$$

where: ' = shorthand notation for the spatial derivative d()/dx

$\dot{}$ = shorthand notation for the time derivative d()/dt

It should be noted that as the value for the radius of curvature of the beam approaches infinity, equations (13) and (14) decouple, and we obtain the equations of motion for a straight beam.

APPENDIX 3-A

Construction Diagram for Track

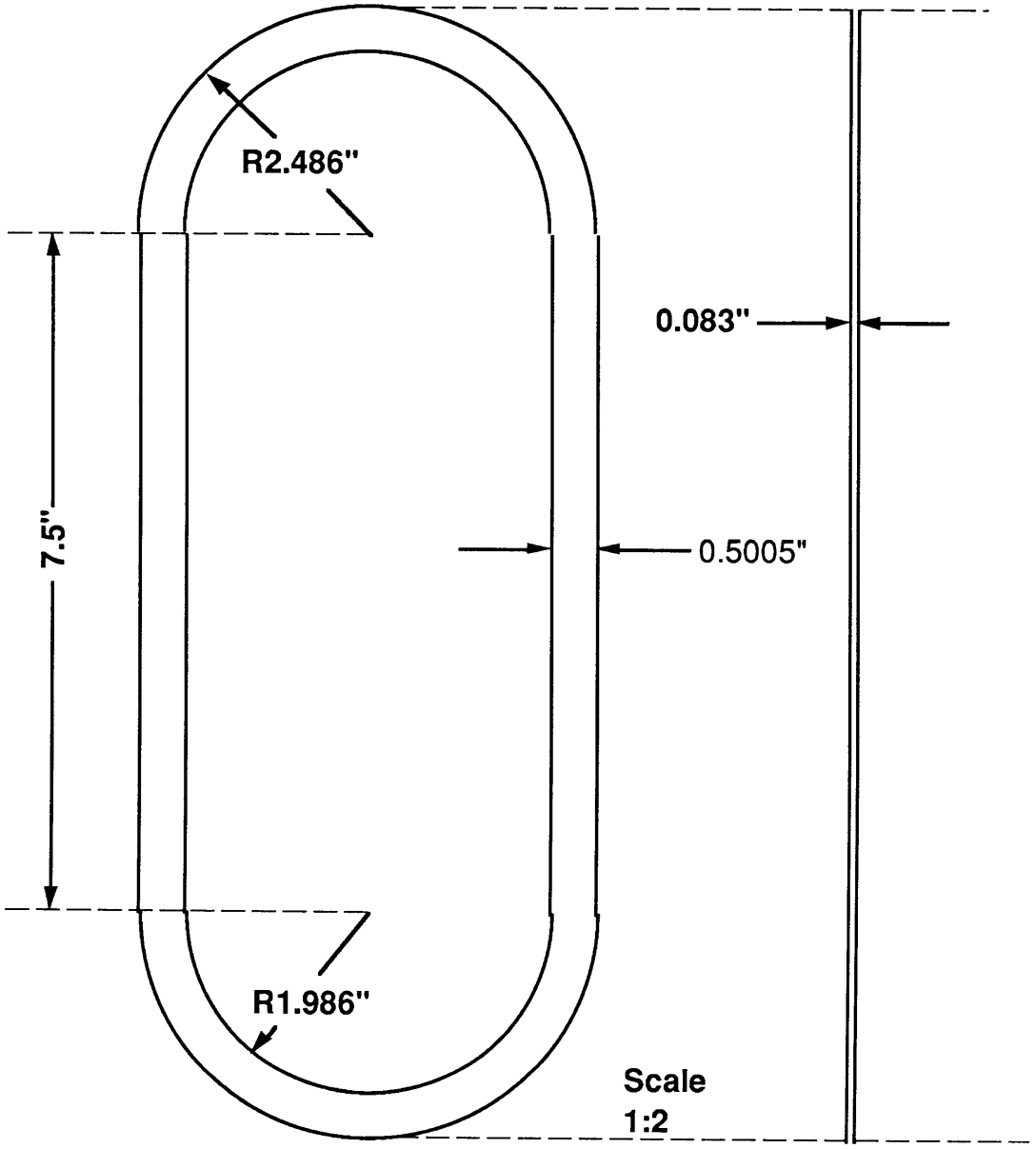

APPENDIX 3-B

Construction diagram for Flat Sliders

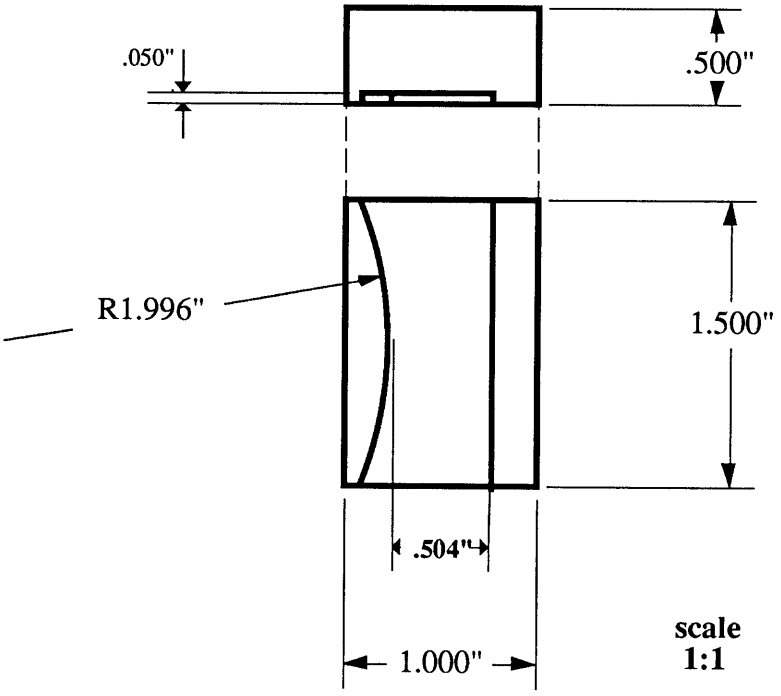

APPENDIX 3-C

Construction Diagram for slotted sliders

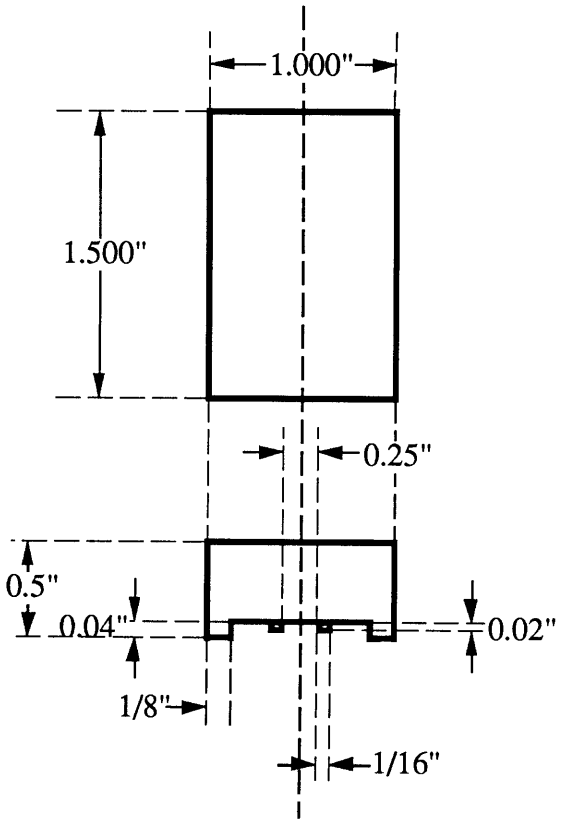

Scale 1:1

APPENDIX 4

Relevant Data of G1195 Piezo Electric Ceramics

Composition		Lead Zirconate Titanate
Material Designation		G1195
Thickness		$h_p = 0.0075$ in
Relative Dielectric Constant		$K_3 = 1700$
.....		$K_1 = 1700$
Piezo Electric Strain Coefficient		$d_{33} = 360 \times 10^{-12}$ m/V
.....		$d_{31} = -166 \times 10^{-12}$ m/V
Polarization Field		$E_p = 2 \times 10^6$ V/m
Coercive Field-	Static	$E_c = 5 \times 10^5$ V/m
	60 Hz	$E_c = 7.5 \times 10^5$ V/m
Density		$\rho = 7600$ Kg/m^3
Elastic Modulus		$YE_{33} = 4.9 \times 1010$ N/m^2
.....		$YE_{11} = 6.3 \times 1010$ N/m^2

APPENDIX 5

Static Analysis Of Beam with Piezo Actuators

The amplitude of the waves in a motor which operates at resonance is equal to the static deflection of the track times a dynamic amplification factor. This amplification factor is inversely related to the damping ratio of the resonant mode of the track and needs to be determined experimentally.

An estimate of the static amplitude of the travelling waves in the racetrack can be derived as follows: Let us isolate a portion of the track equal in length to half the wavelength of the travelling waves. Let the end points of this portion of the track correspond to points of zero deflection. Let a pinned-pinned Euler beam of equal length and cross sectional properties replace the selected portion of the track. Finally, lets define a coordinate frame in which the origin is located half way between the end points of the beam. Figure 42 illustrates the selected portion of the track in its undeflected state.

As shown by De Luis [14], piezo ceramic actuators attached to a structure can be modelled as point moments located at the edge of the ceramics. The selected portion of the track has two piezo ceramic segments attached to its lower side. Assuming that both piezos are being excited equally, they each can be modelled as two moments. The moments generated at x=0, being equal in magnitude and opposite in direction tend to cancel each other out. The moments that remain are the moments applied at each end of the pinned-pinned beam.

The problem of estimating the static amplitude of the track has been simplified to calculating the deflection of a pinned-pinned beam due to two applied moments at the tips of the beam.

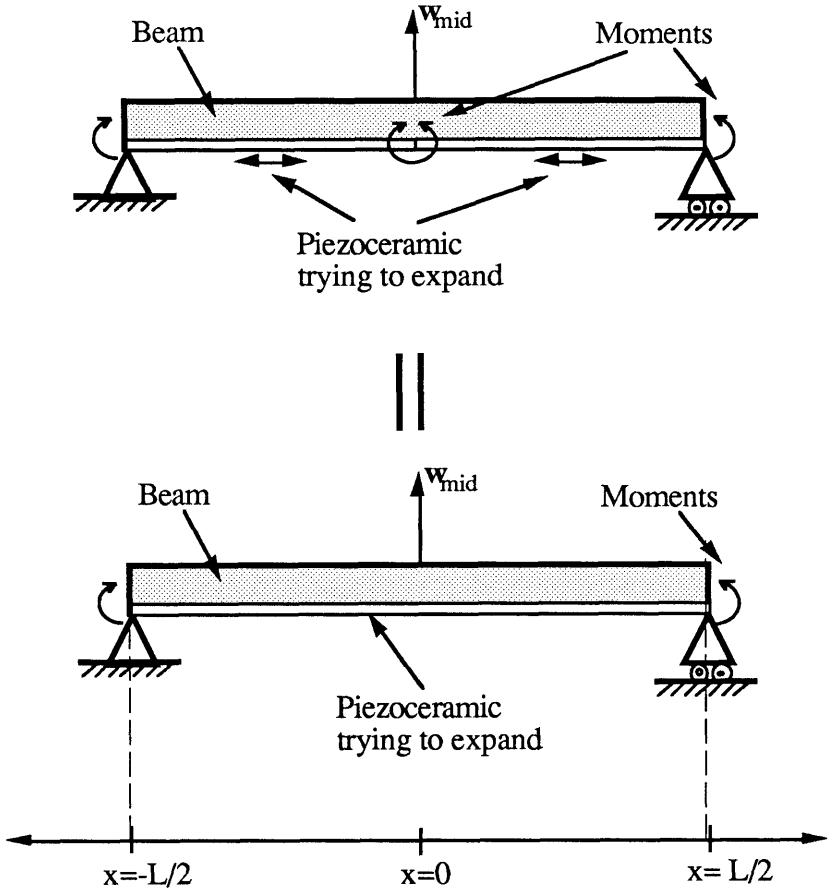

Figure 42- A Pinned-Pinned Beam with Two Piezo Ceramic Actuators can be Modelled as a Pinned-Pinned Beam and Two Moments Located at the End Points

From simple Beam-theory we can recall that :

$$EIw''_{(x)} = M_{(x)} \tag{57}$$

where w" is the second derivative with respect to x of the assumed deflection shape of the beam. If $w_{(x)}$ is given by:

$$w_{(x)} = w_{mid}\left(1 - \frac{4x^2}{L^2}\right) \tag{58}$$

where: w_{mid} = deflection at x=0 (see Figure 40)

By taking the second derivative with respect to x, solving for w_{mid} and substituting (57) and (58) into the resulting expression we obtain (59):

$$w''_{(x)} = -\frac{8}{L^2} w_{mid}$$

$$w_{mid} = -\frac{L^2 w''}{8}$$

$$w_{mid} = -\frac{L^2 M}{8EI} \tag{59}$$

From De Luis [14], we obtain an expression for **M**, the moment applied by the piezo actuators at the tips of the beam, as a function of the thickness of the beam, **h**, the thickness of the piezo ceramics, $\mathbf{h_p}$, the voltage applied to the piezo ceramics, $\mathbf{V_a}$, the piezo electric strain coefficient $\mathbf{d_{31}}$ and the modulus of elasticity of the of the track and of the piezo ceramics :

$$M = \frac{-Eh^2 b}{\Psi + \alpha} \frac{d_{31} V_a}{h_p} \tag{60}$$

where :

$$\alpha = 6$$

$$\Psi = \frac{Eh}{E_p h_p}$$

By substituting equation (60) into equation (59) we obtain an expression which provides an estimate for the static deflection of the track as a function of the applied voltage, the dimensions of the track and the operating conditions of the motor:

$$w_{mid} = \frac{L^2}{8} \frac{h^2 b}{(\Psi + \alpha)} \frac{d_{31} V_a}{h_p l} \tag{61}$$

APPENDIX 6

Acoustic Power Estimation Procedure.

A sound level meter measures the pressure variation due to a given a sound. The sound Pressure Level, L_p, is defined as :

$$L_p = 20 \log_{10} \frac{p}{p_{ref}} \tag{62}$$

where p_{ref} , for gases, is defined by convention to be 2 x 10^{-5} Pa and **p** corresponds to pressure level of the disturbance being measured.

As shown by Beranek [15], Sound Intensity Levels can be approximated by Sound Pressure Level measurements, if these are taken in a room at a temperature of approximately 20 degrees Celsius and 1 atmosphere of pressure. Sound Intensity Level, L_I, is defined as:

$$L_I = 10 \log_{10} \frac{I}{I_{ref}} \tag{63}$$

where I_{ref} is defined by convention as 10^{-12} watts/m^2.

In order to obtain an estimate of the amount of power needed to produce a sound at a given Sound Pressure Level, we must first define Sound Power Level and the relation between the two of them. Sound Power Level, L_w, is defined as :

$$L_W = 10 \log_{10} \frac{W}{W_{ref}} \tag{64}$$

where W_{ref} is defined by convention as 10^{-12} watts, and **W** is the power of the source producing the sound. If the intensity of the sound is constant over an area **S**, then sound Power Level can be written in terms of the Sound Intensity Level as follows:

$$L_W = L_i + 10\log S \tag{65}$$

where **S** corresponds to the surface area in meters over which the measurement is being taken.

In order to estimate the amount of power converted into audible sound by the motor, the value of $\mathbf{L_I}$ was assumed to be equal to the measured value of $\mathbf{L_p}$. The value of **S** was then calculated after measuring the diameter of the microphone used to measure the sound pressure level. Through equation (65) we obtain a value for $\mathbf{L_w}$, which can then be used in equation (64) to obtain the estimate for power, **W**, in watts.

APPENDIX 7

Force Balance on Slider Resting on Inclined Track

Given the following force balance diagram :

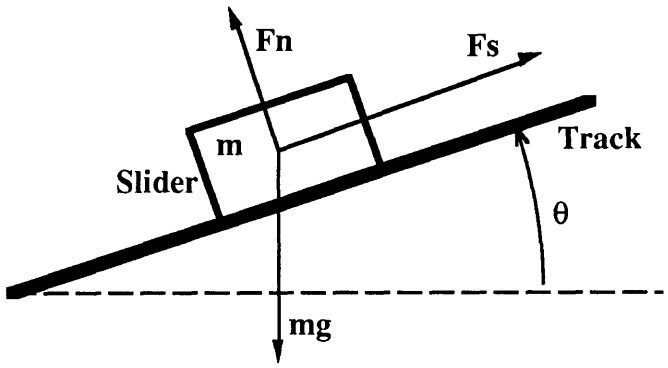

Static equilibrium (ie.- velocity of slider is constant) requires that :

$$F_s = mg\sin(\theta)$$

but since the Normal Force, $\mathbf{F_n}$, is also related to the angle θ by :

$$F_n = mg\cos(\theta)$$

then it can be concluded that static equilibrium always requires that :

$$\frac{F_s}{F_n} = \tan(\theta)$$

This implies that the force coefficient of the motor, which we have defined as the ratio of the side force exerted on the sliders to the normal force on the track, is equal to the tangent of the angle of the track at which a slider will reach static equilibrium.

$$\frac{F_s}{F_n} \equiv \text{Force Coefficient of Motor} = \tan(\theta)$$

VII-REFERENCES

1- Love, A.E.H., Treatise on the Mathematical Theory of Elasticity, University Press, Cambridge, 1927, p 444-454.

2- Graff, Karl F., Wave Motion in Elastic Solids, Clarendon Press. Oxford 1975 p.140-212.

3- Flynn, A.M.; Brooks, R.A.; Tavrow, L.S., Twilight Zones and Cornerstones - A Gnat Robot Double Feature, MIT Artificial Intelligence Laboratory, A.I Memo 1126, July 1989. -

4- Panasonic Ultrasonic Motor Technical Reference. EMDUSM-8703,, Electric Motor Division, Matsushita Electric Industrial Co., Ltd.

5- Scheibel Josef, *Piezo-Revolution in Fotogeråten* ?, Aus Fotomagazin, May, 1987.

6- Kuribayashi, M.; Sadayuki, U.; Mori, E., Excitation Conditions of Flexural Travelling Waves for a Reversible Ultrasonic Linear Motor, Journal of the Acoustical Society of America, #77(4), April 1985, pp 1431-1435.

7-.Cremer, L.; Heckl, M.; Ungar, E., Structure-Borne Sound- Structural Vibrations and Sound Radiation at Audio Frequencies , Springer-Verlag, Berlin, Second Edition 1988. p 109-115.

8- von Flotow, A.H., A Travelling Wave Approach to the Dynamic Analysis of Large Space Structures, presented at the 24th SDM Conference, May 1983. AIAA 83-0964. -

9- von Flotow, A.H., Disturbance Propagation in Structural Networks, Journal of Sound and Vibration (1986) 106(3), pp. 433-450. -

10- Bispinglinhoff, R.L., Ahley, H, and Halfman, R.L., Aeroelasticity, Reading, MA : Addison Wesley, 1955. pp 105-106

11- Inaba,R.; Tokushima, A.; Kawasaki, O.; Ise, Y.; Yoneno, H., Piezoelectric Ultrasonic Motor, Proceedings of 1987 Ultrasonic Symposium, p 744-756.

12- Kawasaki, O., Nishikura, T.; Imasaka Y.; Sumihara, M.; Takeda, K.; Yoneno, H., Ultrasonic Motors, IEEE Tokyo Section, Denshi Tokyo No. 26, (1987).

13- Rabinowicz,E., "The Nature of Static and Kinetic Coefficients of Friction", Journal of Applied Physics, Volume 22, Number 11, 1951

14- Crawley, E.F., and de Luis, J., "Use of Piezoelctric Actuators as elements of Intelligent Structures", AIAA Journal, Vol 25, No 10, 1987.

15- Beranek, Leo L., Noise and Vibration Control , Institute of Noise Control Engineering (publ.), Revised Edition, 1988, Cambridge, MA, p 25-36.

VIII- Annotated Bibliography

1- Bennighof, J.K.; Meirovitch, L., Active Suppression of Travelling Waves in Structures, Journal of Guidance and Control, No 4, July-August 1989, pp. 555-567. - This paper is concerned with the control of travelling waves in structures. Two approaches to the problem are presented, independent modal-space control and direct feed back control.

2- Gaberson, A. Howard, "Material Transport on Oscillating Conveyors", PhD Thesis in Mechanical Engineering at MIT, January 1967. - Detailed study of the dynamics of objects placed on oscillating conveyor belts. Useful reading when trying to characterize the motion of small objects which do not remain in contact with the supporting surface at all times.

3- IEEE Std 176-1978, "IEEE Standard on Piezoelectricity", 1978. - A summary of terms, definitions and models relevant to the use of piezoelectric materials.

4- von Flotow, A.H. and Schäfer, B.,Wave-Absorbing Controllers for a Flexible Beam, Journal of Guidance and Control, Volume 9, No 6, Nov-Dec 1986. - This paper describes theoretical and experimental work in the areas of wave absorption and control in flexible beams. The impedance matching problem between the termination of a beam and free air is addressed.